CONTENTS

CHAPTER THREE

CHAPTER FOUR

LIST OF ABBREVIATIONS, SYMBOLS AND CONSTANTS

CSP	Concentrating solar power
f	Selectivity
AM	Air mass
IR	Infrared
FTIR	Fourier Transform Infrared
UV-vis-NIR	Ultraviolet-Visible-Near infrared
NIR	Near infrared
UV	Ultra violet
T	Absolute temperature
λ	Wavelength
λ_c	Cut off wavelength
$\alpha(\lambda)$	Absorptance
$\varepsilon(\lambda)$	Emittance
$R(\lambda)$	Reflectance
$T(\lambda)$	Transmittance
EM	Electromagnetic field
N_0	Amplitude of EM field
$N=n+ik$	Complex optical constant
n	Refractive index
k	Extinction coefficient
ε	Complex dielectric constant
BR	Bruggeman
MG	Maxwell-Garnet
EMT	Effective Medium Theory
AFM	Atomic Force Microscopy
EDS	Energy Dispersive Spectroscopy
XRD	X-ray Diffraction
SEM	Scanning Electron Microscopy
RBS	Rutherfold Backscattering
TEM	Transition Electron Microscope
SSC	Solar selective coating

SS	Stainless Steel
SA	Super Alloy
CVD	Chemical Vapor Deposition
PVD	Physical Vapor Deposition
ALD	Atomic layer Deposition
c	Speed of light in vacuum, $2.9979*10^{8}$ m/s
e	Electronic charge
m	Mass of the electron
P	Power
δ	Change in phase
Γ	Dumping Force
ω	Angular frequency
ω_p	Plasma frequency of material
ω_0	Resonance frequency of Lorentz model
ε_0	Permittivity of free space
μ_0	Permeability of free space
h	Plank's constant, $6.626*10^{-34}$ *Js*
k_B	Boltzman's constant, $1.381*10^{-23}$ *J/K*
σ	Conductivity
Eqn.	Equation
Fig.	Figure
et al.	Et alia
etc.	et cetera
Al	Aluminium
D.I.	De-ionized water
AC	Alternating Current
NR	Nanorod
NC	Nanocylinder
NW	Nanowire
NT	Nanotube

CHAPTER ONE

INTRODUCTION

1.1 BACKGROUND TO THE RESEARCH STUDY

Solar Energy is an abundant renewable energy source, striking the earth at a rate of 90,000TW, which is 5000 times our current global power [1.1]. Most of this energy is received in Africa, also known as a continent of sunshine and heat, a place of the hottest nations in the world [1.1]. We receive on average a very high amount of days per year with bright sunlight especially the dry and desert areas; this creates massive solar energy potential. Most renewable energy comes either directly or indirectly from the sun, it is converted into useful forms through different ways [1.2-1.3].

The sun's non uniform heat on the earth's surface creates mass flow of moving air in the atmosphere whose energy is captured with wind turbines. Water circulation in the earth is driven by the sun; its energy can be captured using hydroelectric power. Bioenergy uses solar energy through the organic matter or biomass that makes up plants. These cases are regarded as indirect uses of solar energy. Direct use of solar radiation consists of photovoltaic (PV) and solar thermal energy conversion for heating and lighting homes and other buildings, generating electricity in solar power plant (CSP) , hot water heating, swimming pools, air conditioning, solar cooling, and a variety of commercial and industrial uses.

Energy is considered essential for sustainable development. As much as it is not a basic need, it is critical for the fulfilment of all needs. Insufficient energy supply means all human services like lighting, cooking, heating and cooling, water pumping, refrigeration, transport and communication are compromised, they will not be met [1.4-1.5]. Lack of access to diverse and affordable energy services will correlate closely with indicators of poverty like poor education, roads and, inadequate health care, hardships imposed on women and children. In developing countries that are the majority in Africa, people spend a lot of time and energy on basic activities like fetching water and collecting firewood rather than on earning money. Limited access to energy marginalizes poor communities and seriously limits their ability to improve their quality of life.

Currently the world relies on fossil fuels to produce 86% of its energy. The combustion of fossil fuels is the largest source of health-damaging air pollution as well as producing large amounts of carbondioxide, this makes the fuels a major source of the greenhouse gas emissions (GHG). Women and their children and most vulnerable to the effects of indoor

pollution from cooking fires. The most serious environment problem today is the steady increase in the atmospheric concentrations of GHGs that cause climate change also known as global warming. The drive to replace fossil fuels with renewable energy sources has accelerated because renewable energy sources are clean and environment friendly, they are a boundless yet barely tapped solution to the two great global challenges such as poverty and global warming [1.6-1.7]. By reducing environmental pollution such as air pollution caused by burning of fossil fuels, renewable energy resources and improve public health, reduce premature mortalities and lower the associated health and climate change mitigation costs.

According to the International Energy Agency, the development of affordable, inexhaustible clean solar energy technologies will have huge longer-term benefits; renewable energy has the ability to raise the world's developing countries to new levels of prosperity [1.6]. Renewable energy will increase a nation's energy security through reliance on an indigenous import-independent resource, enhance sustainability and this way promotes the economic growth.

This research work is based on highly oriented tubular Co nanocomposites embedded in Al_2O_3 host matrix deposited on flexible Aluminium substrates for the application of selective solar absorbers. Solar absorbers used in solar thermal conversion are the direct method of harnessing solar energy. Energy production systems like CSP and other solar collectors that use selective solar absorbers generate very low levels of green-house gas emissions and are therefore emerging as a key technology for extenuating climate change [1.8].

1.2 STATEMENT OF THE PROBLEM

The optical properties and thermal stability of the material used as a solar absorber coating will determine the level of efficiency in solar-thermal conversion systems [39], increasing the operating temperature improves performance. Current coating exhibit thermal stability and very good solar absorption characteristics at temperatures lower than 500 ºC , they lack the stability and performance necessary to move to higher operating temperature. It is important to develop high temperature selective stable solar absorber nanocoatings with both high solar absorptance ($a \geq 0.96$) and low thermal emittance ($\varepsilon < 0.07$ at 400 ºC) that are thermally stable above 500 ºC, ideally in air, with improved durability and manufacturability.

Current research has not considered the possibility of electrodeposited Co and Ni nanowires in porous alumina owith an additional femtosecond laser surface structuring as a selective

absorber coating material. It is fundamentally important to develop this novel ferromagnetic coating because the electrodeposition technique of the magnetic nanowires is a low cost, high yield, easy to use method that has speed and ability to achieve extremely small features. Laser surface structured Co and Ni nanocylinders in self-assembled arrays are a potential candidate in the development of high temperature selective stable solar nano-coatings.

1.3 SOLAR RADIATION

1.3.1 The Sun

The sun is the star closest to the earth and its radiant energy is the source of energy that influences atmospheric motions and climate. It is a spherical body of diameter $1.39x10^6$ km made of intensely hot gaseous matter consisting of mainly hydrogen and has an effective black body temperature of about 5762 K [1.9]. The energy radiated from the sun is due to reactions dominated by hydrogen nuclei combining to form helium nuclei and heat energy. The sun has seven layers in order from the interior: core, interior, convecting zone, photosphere, reversing layer, chromosphere and corona. The photosphere is considered to be the source of most of the solar radiation arriving at the Earth's surface.

1.3.2 The Electromagnetic Spectrum

Solar energy is an electromagnetic wave, this as first proposed by J.C.Maxwell is a combination of electric and magnetic properties of streams of massless particles called photons travelling in a wave-like pattern at the speed of light [1.10-1.11]. The different types of radiation are defined by the amount of energy found in the photons. The electromagnetic (EM) spectrum is the range of all types of EM radiation classified according to frequency from the high frequency and energy cosmic and gamma rays of short wavelength ~ 10^{-8}μm to low frequency and energy radio waves of long wavelength ~10^{10}μm. The wavelengths of interest for solar-thermal applications are found in the wavelength range of ultraviolet to infrared (0.3-50μm), thus include the solar spectrum range of 0.3-3μm and the spectral range of thermal radiation at about 2-50μm, which is emitted from a surface [1.12] . The solar spectrum which is the radiation incident at the surface of the Earth, after atmospheric absorption runs from ultraviolet-visible-near infrared (UV/Vis/NIR) wavelengths.

1.3.3 Solar radiation on the Earth's surface

The solar insulation, coming from the sun to the earth, perpendicularly to the atmosphere highest layers is about 1353W/m^2, which is called the solar constant. It consists of two main components; direct and diffuse solar radiation [1.12]. Direct solar radiation is radiation received directly from the Sun without multiple scattering while diffuse radiation is the radiation resulting from multiple scattering by the constituents of the Earth's atmosphere such as clouds, atmospheric gases, and water vapour molecules. The Earth revolves around the Sun in an elliptical orbit causing the distance between the Sun and Earth to vary periodically. This has an effect on the mount of solar radiation reaching the Earth [1.10-1.11]. The solar radiation reaching the Earth is inversely proportional to the square of its distance from the Sun. Literature has reported an average Sun- Earth distance of one astronomical unit equal to $1.496x10^8 \pm 500$km. The intensity of direct solar radiation on the earth surface can reach 1kW/m^2, but the amount of solar energy on the earth horizontal surface at our latitude can be up to 1000 kWh/m^2 .

1.3.4 The Sun as a Black Body

The blackbody is well known as a perfect absorber or emitter of radiation with additional property of zero surface reflection and complete internal absorption [1.13]. These properties qualify for it to serve as a standard comparison for bodies emitting radiation, however in nature only a few materials such as gold black, carbon black approach the blackbody's ability to accurately absorb radiant energy. The blackbody derives its name from the fact that to the human eye, good absorbers of incident visible light do indeed appear black. Outside the visible region into the spectral range of thermal radiation, our eyes are not good indicators of the absorbing ability of a material. Let us consider a material that has been coated with white based paint. At room temperature this material is a excellent absorber of infrared radiation but a poor absorber of light in the visible region of the solar spectrum.

1.3.5 Air Mass

The solar radiation is attenuated when it passes through the earth's atmosphere. Since the spectral distribution of the solar radiation also depends on the attenuation, various solar spectra can be measured at the earth's surface. The degree of attenuation is variable. The parameter that determines the intensity of solar irradiance is the distance that the sunlight has to travel through the atmosphere. This distance is the shortest when the sun is at the zenith

(directly overhead). The Optical air mass (AM) is defined as the ratio of the mass of the atmosphere through which the sunlight passes to the mass it would pass at the sun's minimal distance (zenith). When the sun is at its zenith the optical air mass is 1 and the radiation is expressed as air mass one (AM1) radiation [1.14-1.15]. When the sun is at an angle to the zenith, the air mass is given by: AM0 radiation is an extraterrestrial spectrum of solar radiation outside the earth's atmosphere at which power density is the solar constant.

The power density of the sun's radiation on the earth's surface is approximately1.4 kW/m^2. This value varies slightly throughout the year by no more than 0.001 due to the change in earth-sun distance. The solar constant is defined as the quantity of solar energy (W/m^2) at normal incidence outside the atmosphere at the mean sun-earth distance; i.e. 1367.7 W/m^2 [1.14-1.15]. However outside the earth's atmosphere, terrestrial solar radiation varies both in intensity and spectral distribution depending on the position on the earth and the position of the sun in the sky. AM 1.5 is used in the following sections to calculate solar absorptance corresponding to an angle of 48.2º between the sun's position and the zenith.

1.3.6 The Solar Spectrum

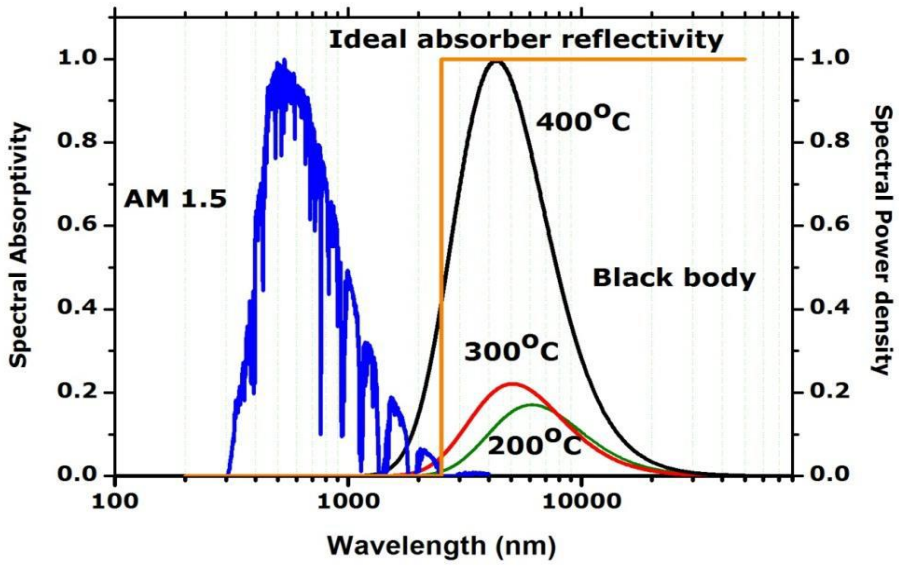

Figure 1.1: The normalized solar radiation spectrum (blue curve), black body radiation spectra at three different temperatures (black, red and green) and the ideal selective absorber reflectance spectrum (yellow) [1.16]

Fig. 1.1 shows the hemispherical solar irradiance that reaches the surface of the Earth after passing through the atmosphere under clear sky conditions. This is adapted from the International Organization for Standardization (ISO) for air mass (AM1.5) i.e when the sun is about 42 above the horizon [1.17]. The solar spectrum has several local minima, which are caused by (1) atmospheric absorption by water vapour, carbon dioxide and ozone and (2) atmospheric scattering by air molecules, water and dust. There is minimal overlap between the solar spectral range of AM1.5 and the thermal emittance spectra at three temperatures of a blackbody-like surface. The non-overlap between the solar radiation and emittance spectra provides an opportunity to tailor a material and to achieve spectral solar selectivity, which strongly determines the efficiency of the solar thermal collectors.

1.4 SOLAR-THERMAL COLLECTORS

Solar-thermal collector is a special kind of heat exchanger designed to collect and convert incoming solar energy into heat/thermal energy. Basically solar collectors are classified into two general categories based on their concentration ratio (*c*):

(i) concentrating and
(ii) non-concentrating

Non-concentrating collectors such as flat plate and evacuated tube collectors have a concentration ratio of one and are mainly designed for solar hot water and industrial process heat applications. The collector area (the area that intercepts the solar radiation) is the same as the absorber area (the area that absorbs the radiation) [1.8]. They are mechanically simpler than concentrating collectors and require less maintenance. Concentrating type collectors such as parabolic-trough, parabolic-dish, and central tower their concentration ratio is above one [1.18]. In these CSP systems, various types of mirrors, reflectors or concentrators are used to concentrate solar energy and they provide higher temperatures (i.e., 400-1000^{o}C) than non-concentrating type collectors.

1.4.1 Non-concentrating collectors

A flat-plate collector is the simplest of all devices used for solar energy utilization. It consists of an absorber panel, which maybe spectrally selective, or in the chipper manner, non-selective. In efficient collectors, the space between the absorber and the cover plates is

evacuated. Solar radiation passes through the cover plate (usually low-iron glass) and is converted by the absorber into thermal energy, which is then transferred to a heat transfer fluid.

Figure 1.2: Solar Thermal Collectors: Flat plate collector and Evacuated tube [1.18]

1.4.1 Concentrated Solar Power (CSP)

Many power plants today use fossil fuels as a heat source to boil water. The steam from the boiling water spins a large turbine, which drives a generator to produce electricity. However, a new generation of power plants with concentrating solar power systems uses the sun as a heat source. CSP technologies use mirrors to concentrate (focus) the sun's light energy and convert it into heat to create steam to drive a turbine that generates electrical power [1.19], see Fig. 1.2. The plants consist of two parts: one that collects solar energy and converts it to heat, and another that converts the heat energy to electricity.

The three main types of concentrating solar power systems are:

1. *Linear concentrator*,
2. *Dish/engine*, and
3. *Power tower systems*.

1. Linear Concentrator Systems collect the sun's energy using long rectangular, curved (U-shaped) mirrors. The mirrors are tilted toward the sun, focusing sunlight on tubes (or receivers) that run the length of the mirrors. The reflected sunlight heats a fluid flowing through the tubes. The hot fluid then is used to boil water in a conventional steam-turbine generator to produce electricity [1.19]. There are two major types of linear concentrator systems: parabolic trough systems, where receiver tubes are positioned along the focal line of

each parabolic mirror; and linear Fresnel reflector systems, where one receiver tube is positioned above several mirrors to allow the mirrors greater mobility in tracking the sun.

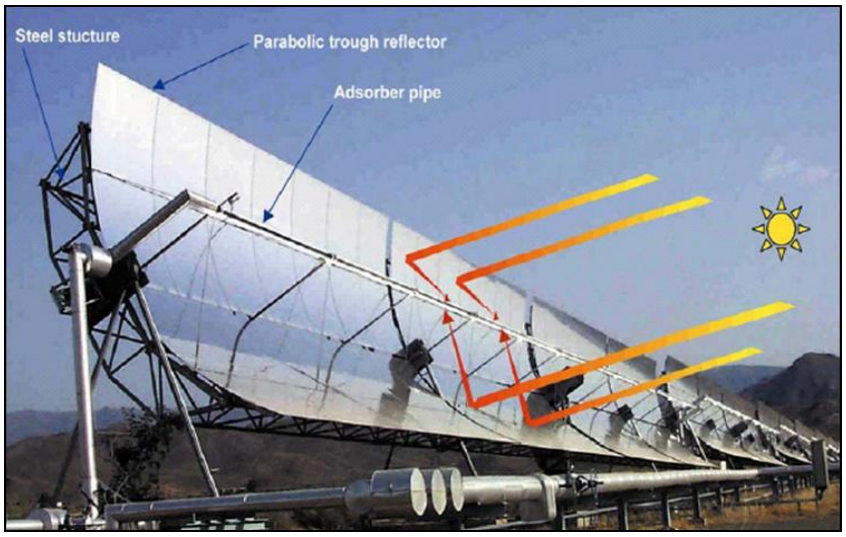

Figure 1.3: Photo of Parabolic trough system [1.19]

2. A Dish/Engine System is the combination of parabolic reflectors and a heat engine, its mirrored and circular dish is similar to a very large satellite dish, see Fig. 1.4. To minimize costs, the mirrored dish is usually composed of many smaller flat mirrors formed into a dish shape. It reflects and concentrates sunlight onto a thermal receiver, which absorbs and collects the heat and transfers it to the engine generator. The most common type of heat engine used today in dish/engine systems is the Stirling engine. This system uses the fluid heated by the receiver to move pistons and create mechanical power. The mechanical power is then used to run a generator or alternator to produce electricity.

Figure 1.4: Schematic of solar dish system [1.20]

3. A Power Tower System also called a Central Receiver uses a large field of flat, sun-tracking mirrors known as heliostats whose angles are computer controlled; to focus and

concentrate sunlight onto a receiver on the top of a tower [1.21]. A heat-transfer fluid heated in the receiver is used to generate steam, which, in turn, is used to drive a turbine generating electricity. Some power towers use water/steam as the heat-transfer fluid. Other advanced designs are experimenting with molten nitrate salt because of its superior heat-transfer and energy-storage capabilities. The energy-storage capability, or thermal storage, allows the system to continue to dispatch electricity during cloudy weather or at night [1.21].

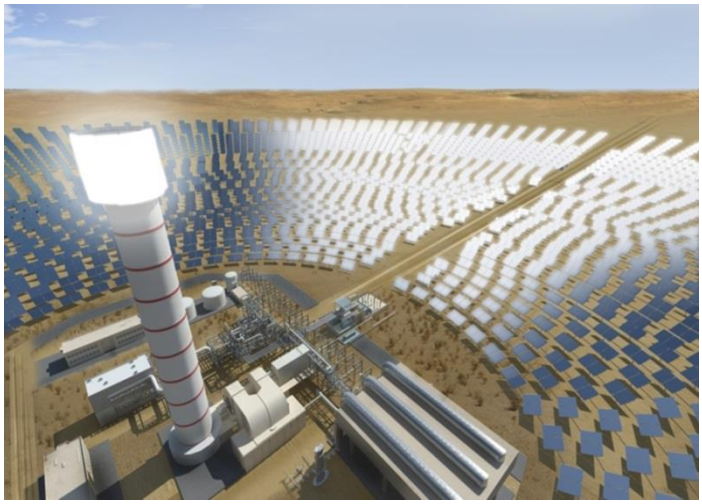

Figure1.5: Power Tower System [1.22]

1.5 SPECTRALLY SELECTIVE SOLAR ABSORBERS.

Spectral Selectivity is the ability of a solar absorber to operate only at a given frequency or within a given band of the solar spectrum. A solar absorber should absorb as much of the incident radiation as possible and should avoid losing the absorbed energy through thermal radiation to the surroundings. For efficient photothermal conversion solar absorber surfaces must capture maximum solar energy in the visible and near infrared spectral regions and should have a minimum thermal emittance in the thermal infrared region at the operational temperature [1.23]. Selective solar absorbers are now widely used in solar hot water systems and concentrated solar power plants, and are actively studied in solar thermoelectric generators as well as solar thermos-photovoltaics.

Efficient photo-thermal conversion is obtained at higher temperatures. Increasing the operating temperature above the current operating limits of 400ºC can improve power cycle efficiency and therefore reduce the cost of thermal energy storage resulting in reductions in the cost of solar generated electricity [1.24]. The solar-selective coating is desired to have

high solar absorptance, low emissivity and stability for temperatures beyond 400ºC. Current photo-thermal coatings are, generally, stable at temperatures lower than 400ºC, they do not have the stability and performance necessary to move to higher operating temperatures [1.24]. Based on the configuration of coatings and the absorption mechanism, these spectrally selective absorbers can be classified into six types as shown in Fig. 1.6.

- Intrinsically selective
- Semiconductor-on-metal coatings
- Multilayer stacks
- Textured surfaces
- Metal-dielectric (cermet) composites
- Selectively transmitting coatings on blackbody-like absorbers

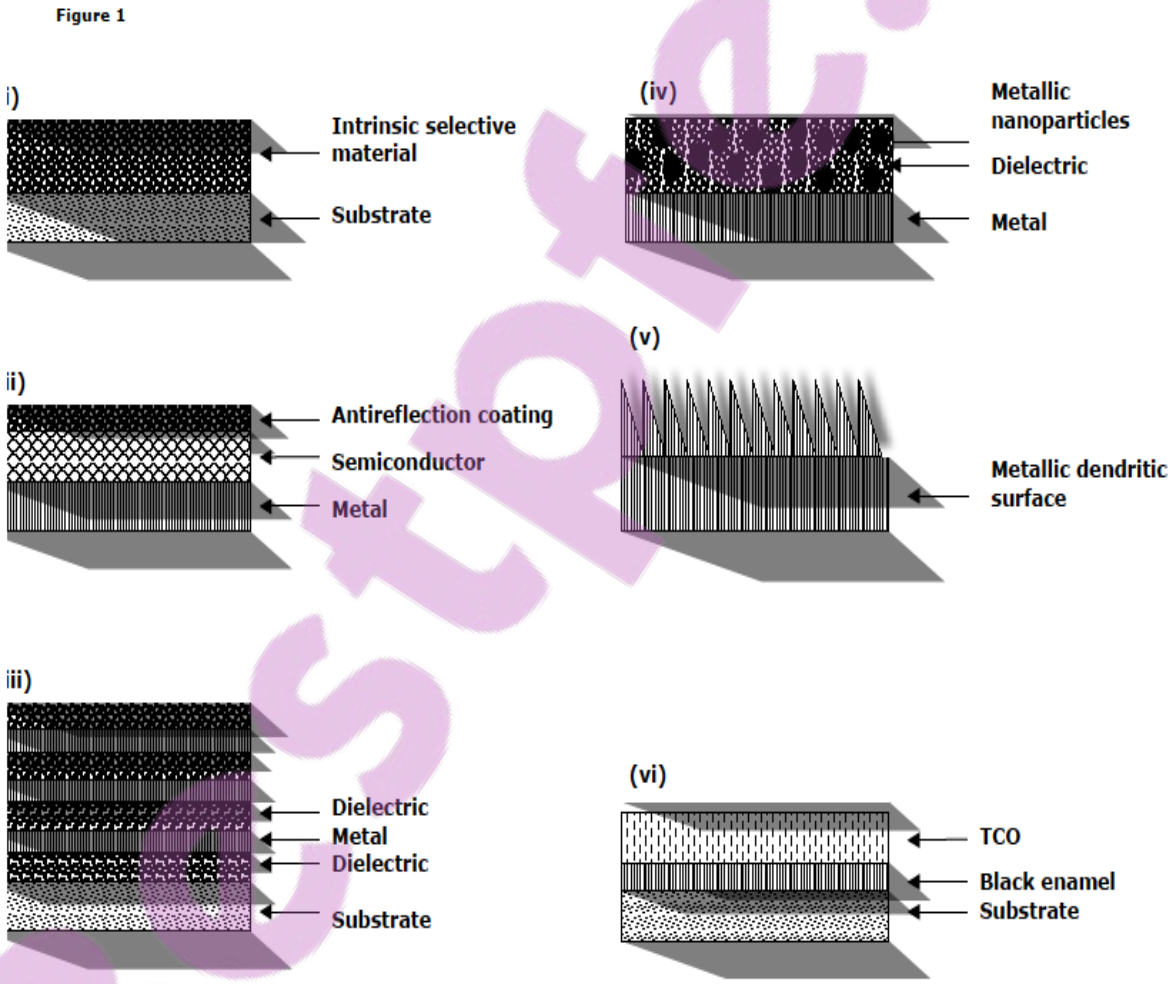

Figure1.6: Various used solar selective absorbers for photothermal conversion applications [1.25].

(i) Intrinsic or mass absorbers

Intrinsic absorbers in which optical selectivity is a natural property of the materials, are structurally more stable but optically less effective than multilayer stacks. Examples include metallic W, MoO_3-doped Mo, Si doped with B, CaF_2 , HfC , ZrB_2 , SnO_2 , In_2O_3 , Eu_2O_3 , ReO_3 , V_2O_5 , and LaB_6 [1.26-1.27]. Research in intrinsic absorbers has not been very productive because no naturally occurring material exhibits intrinsically ideal solar-selective properties. Some semiconductors, carbides and nitrides of transition metals possess semi-selectivity but they need to be greatly modified to serve as intrinsic absorber. Intrinsic materials however, are finding increasing use as a component in high-temperature absorber multilayers and composite coatings.

(ii) Semiconductor-metal tandems

Semiconductors with low bandgaps from about 2.5μm to 1.0μm absorb short wavelength, the metal beneath is highly IR reflecting and provides the low emittance to give the desired spectral selectivity. The semiconductor layer absorbs photons having energies greater than the band gap, while those of less energy are transmitted through the coating unchanged. Semi-conductor tandems of interest include Silicon (Si), Germanium (Ge) and Lead Sulphide (PbS) [1.28]. To obtain high solar absorptance antireflection coatings are needed because the semiconductor tandems have high refractive indices, which result in large detrimental reflectance losses on the air/semiconductor interface. Si-based designs produced by chemical-vapor deposition (CVD) are suitable for mid-to high-temperature applications [1.29].

(iii) Multilayer absorbers.

These are also referred to as multilayer stacks can be designed so that they become efficient selective absorbers. The selective effect is because the multiple reflectance passes through the bottom dielectric layer and is independent of the selectivity of the dielectric. This bottom dielectric layer is covered by a thin semi-transparent reflective metal layer that has high reflectance in the infrared (IR) region and is slightly less reflective in the visible region [1.30-1.31]. The top dielectric layer reduces the visible reflectance and increases the absorption in the visible region and broadens the region of high absorption. The thickness of this dielectric determines the shape and position of the reflectance curve. Below the top dielectric layer is an additional semi-transparent (i.e., thin) metal layer that further reduces the reflectance in

the visible region [1.30-1.32]. Multilayer interference stacks have high solar absorption, low thermal emittance, and are stable at elevated temperatures (≥ 400ºC) depending on the materials used. Several multilayer absorbers using different metals (e.g., Mo, Pt, Ag, Cu, z and Ni) and dielectric layers (e.g., Al_2O_3, SiO_2, CeO_2, ZnS) have been cited in the literature for high-temperature applications.

(iv) Metal-dielectric composite coating

Metal-dielectric composite coatings or absorber-reflector tandems consists of fine metal particles or metal oxide nanoparticles embedded in a dielectric or ceramic matrix deposited on a highly infrared reflecting metal substrate. These films are transparent in the thermal IR region, while they are strongly absorbing in the solar region because of interband transitions in the metal in combination with small particle resonance. The base metal dominates the infrared properties (the low thermal emission) of the absorber. Solar selectivity of this cermet can be tailored by varying the choice of particle, metal volume fraction in the matrix, particle size, shape and orientation, optical constants of the constituents, thickness of the composite coating [1.31]. This high degree of flexibility is the major advantage of metal tandems.

(v) Surface texturing

Surface texturing can be very efficient for optical trapping of solar energy through the surface features of a roughened surface by multiple reflections and partial absorptions. Properly textured surfaces appear rough (needle-like, dendrite, or porous microstructures) and absorb solar energy while appearing highly reflective and mirror-like to thermal energy because thermal infrared dimensions are greater than the surface features. The emittance can be adjusted (higher or lower) by modifying the microstructure (microcrystallites) of the coatings with ion-beam treatments, chemical or sputtering etching and sandblasting [1.33]. The selective properties depend on the ratios of mean height deviations and the autocorrelation distance to the wavelength [1.34-1.35], well known examples include dendritic tungsten, textured copper, nickel and stainless steel surfaces.

vi) Selectively solar-transmitting coating on a blackbody-like absorber

A selectively solar-transmitting coating on a blackbody-like absorber is the last concept. The selective solar-transmitting coating can be a highly doped semiconductor (e.g., SnO_2:F,

SnO_2:Sb, In_2SO_3:Sn, and ZnO:Al) over an absorber with a proven long-term durability. Some low-temperature flat-plate collectors have used black enamel as the absorber material [1.3]. Highly doped semiconductors may be useful with high-temperature black absorber materials.

1.6 AIMS AND OUTLINE

Nanotechnology is the manipulation of matter on an atomic, molecular and supramolecular scale it is one of the emerging technologies that have been widely used recently in various applications like memory devices, sensors, semiconductor devices magnetic recording, electronic and electro-optical devices and optoelectronic device. Synthesis and characterization of nanowires has been studied widely, because of their unique physical and structural properties. These nanostructures are not only interesting for research but also attract the various applications in the field of future technology because of their innovative properties. In this thesis ferromagnetic nanowires in nanoporous alumina will be used for solar thermal energy application. Nanocermets are potential candidates for solar energy conversion because they exhibit strong absorption in the visible region which occurs because of surface plasmon resonance phenomena, also known as quantum confinement effect.

The current global objective targeted by the international community working on photo-thermal solar energy conversion is to develop new, more-efficient selective coatings with both high solar absorptance ($\alpha \geq 0.96$) in the solar spectrum region and low thermal emittance ($\varepsilon < 0.07$ at 400 ºC) in the infrared region that are thermally stable above 500 ºC, ideally in air, with improved durability and manufacturability.

The main objective of this work is to provide a new family of femtosecond laser surface structured selective solar absorbers consisting of electrodeposited non-percolated and highly oriented Co nanocylinders embedded in nanoporous Al_2O_3 host matrix. Aluminium oxide (Al_2O_3) coatings have high hardness, excellent dielectric properties, refractoriness and good thermal properties making them good choice for developing a high-temperature solar absorber [1.36].

Chapter 2 provides a detailed survey of solar selective coatings used for mid-and high temperature solar thermal applications that have been developed using a variety of physical vapor deposited processes that include evaporation, sputtering, ion plating, pulsed laser

deposition). Other methods such as electroplating, anodization and solution-based method are also presented.

Chapter 3 of the thesis will focus on the theoretical background of selective solar absorbers. This will include basic electromagnetic wave theory, Effective Medium Theories Maxwell Garnett as well as the Bruggeman models for inhomogeneous materials and brief survey on laser surface structuring.

Chapter 4 deals with the experimental methods that were used to design the laser surface structured Co-Al_2O_3 selective solar absorber. We also discuss the operation of various techniques that were used to investigate the structural, chemical and optical properties of the coatings which include SEM, AFM, XRD, EDS, RBS, Raman spectroscopy and optical spectroscopy.

Chapter 5 will report results and their analysis. We discuss the structural and optical properties of laser surface structured laser surface structured Co-Al_2O_3 cermet solar absorber. This chapter will also include an investigation of a double ferromagnetic cermet, namely (Co-Ni) nanocylinders-Al_2O_3 cermet on flexible Aluminium substrate for enhanced solar selective absorbers applications and also a section on the effect of annealing on the structural and optical properties of the laser surface structured Co-Al_2O_3 cermet.

The final *chapter 6* will present the concluding remarks, future work/scope of the current thesis and summary of the research project.

1.7 REFERENCES

[1.1] P.M. Boffey, Science, 168 (1970) 1554-1559.

[1.2] Renewable energy. http://en.wikipedia.org/wiki/Renewable.energy. Wikipedia, the free encyclopedia.

[1.3] C.G. Granqvist, V. Wittwer, Materials for solar energy conversion. Solar Energy Materials & Solar cells 54 (1998) 39-48.

[1.4] K. Kaygusuz, Energy for sustainable development: Key Issues and Challenges. Energy Sources, Part B 2 (2007): 73-83.

[1.5] N.C. Leitao, Economic Growth, Carbon Dioxide Emissions, Renewable Energy and Globalization. International Journal of Energy Economics and Policy 4 (2014) 391-399.

[1.6] N. Apergis, D.C. Danuletiu, Renewable Energy and Economic Growth: Evidence from the Sign of Panel Long-Causality. International Journal of Energy Economics and Policy 4 (2014) 578-587.

[1.7] P. Sadorsky, Renewable energy consumption and income in emerging ecomomies. Energy policy 37 (2009) 4021-4028.

[1.8] N. Selvakumar, H.C. Barshilia, Review of physical vapor deposited (PVD) spectrally selective coatings for mid- and high-temperature solar thermal applications. Solar Energy Materials & Solar Cells 98 (2012) 1–23.

[1.9] J.A. Duffie, W.A. Beckmann, Solar Engineering of thermal processes. (1980), Wiley Interscience Publication. Chapters 1-3.

[1.10] J. Mubiru, Deveploment of an appropriate solar radiation model for Uganda. Ph.D. Dissertation, Uganda: Makerere University; (2006).

[1.11] M. Iqbal, Introduction to Solar Radiation. (1989), Pergamon Press.

[1.12] J.C. McVeigh, Solar Radiation in Sun Power. (1977), Oxford: Pergamon Press.

[1.13] T.B. Chibuye, A Comparative Study of Copper- and Nickel-Pigmented Anodised Aluminium Coatings for Solar Energy Absorption. Ph.D. Dissertation, Zambia: University of Zambia; (2002).

[1.14] P. Jayakumar, Solar energy - Resource assessment handbook. 1st ed. (2009), APCTT 1-117.

[1.15] W.L. Wolfe, G.J. Zissis, The infrared handbook, Environmental Research Institute of Michigan. (1989), Washington DC.28Deut8.

[1.16] Z.Y. Nuru, Spectrally selective $Al_XO_Y/Pt/Al_XO_Y$ solar absorber coatings for high temperature solar-thermal applications. Ph.D. Dissertation, South Africa: University of Western Cape; (2014).

[1.17] International Organization for Standardization. ISO 9845-1. Solar energy. Reference solar spectral irradiance at the ground at different receiving conditions. Part 1: Direct normal and hemispherical solar irradiance for air mass 1,5, International Organization for Standardization (1992), 1-14.

[1.18] Z. Sen, Solar Energy Fundamentals and Modeling Techniques: Atmosphere, Environment, Climate change and Renewable Energy. (2008), Springer.

[1.19] Concentrated Thermal Power Now. http://www.greenpeace.org/raw/content/international/press/reports/Concentrated-Solar-Thermal-Power.pdf.

[1.20] Dish/Engine systems. http://www.examiner.com/article/stirling-energy.

[1.21] Solar-Facts. Light concentration methods for Solar Power Installations. www.solar-facts.com/light-concentration/.

[1.22] Energy Power Solar Thermal. http://www.exergypower.com.au/solar-thermal.php.

[1.23] S. Khamlich, R. McCrindle, Z.Y. Nuru, N.Cingo, M.Maaza, Annealing effect on the structural and optical properties of Cr-Cr_2O_3 monodispersed particles based solar absorbers. Applied Surface Science 265 (2013) 745-749.

[1.24] C.E. Kennedy, Review of Mid- to High-Temperature Solar Selective Absorber Materials, NREL/TP-520-31267, National Renewable Energy Laboratory, Colorado, July 2002.

[1.25] M. Maaza, Z.Y. Nuru, S. Khamlich, B.D. Ngom, Surface-Interface investigation and stability of cermet based solar absorbers by grazing angle x-rays reflectometry: Pt-Al_2O_3 case. The Arabian Journal for Science and Engineering.

[1.26] G. Pellegrini, Experimental methods for the preparation of selectively absorbing textured surfaces for photothermal solar conversion. Solar Energy Materials 3 (1980) 391.

[1.27] W.F. Bogaerts, C. Lampert, Review Materials for photothermal solar energy conversion. Journal of Material Science 18 (1983) 2847-2875.

[1.28] D.M. Mattox, G.J. Kominiak, Deposition of semiconductor films with high solar absorptivity. Journal of Vacuum Science and Technology 12 (1975) 182–185.

[1.29] B.O. Seraphin, Chemical vapor deposition of thin semiconductor films for solar energy conversion.Thin Solid Films 57 293 (1979).

[1.30] Å. Andersson, O. Hunderi, C.G. Granqvist, Nickel pigmented anodic aluminium oxide for selective absorption of solar energy. J. Applied Physics 51 (1980) 754-764.

[1.31] M. Nejati, Cermet based solar selective absorbers; further selectivity improvement and developing new fabrication technique, Ph.D. Dissertation. University of Saarlandes; (2008).

[1.32] M. Born, E. Wolf. Principles of Optics, 6th Ed. (1980), Oxford: Pergamon.

[1.33] O.P Agnihotri, B.K. Gupta, Solar Selective Surfaces. (1981), New York: John Wiley & Sons.

[1.34] B.O. Seraphin, A.B. Meinel, Optical Properties of Solids: New Developments. ed. B.O. Seraphin. (1976), Amsterdam: North Holland Publishing Co.

[1.35] J.J. Cuomo, J.F. Ziegler, J.M. Woodall, A new concept for solar energy thermal conversion. Applied Physics Letters 26 10 (1975) 557.

[1.36] Z.Y. Nuru, C.J. Arendse, S. Khamlich, M. Maaza, Vacuum 86 (2012) 2129-2135.

CHAPTER TWO

LITERATURE SURVEY OF SELECTIVE SOLAR ABSORBERS

This chapter presents a detailed overview of previous work that has been reported by several authors using different fabrication techniques namely: Physical and chemical vapor deposition (Evaporation, Sputtering), Electroplating, Anodization, Painting and Solution-based fabrication to prepare cermet- based spectrally selective solar absorbers. We discuss one by one the solar thermal performance of different dielectric materials such as Cr_2O_3, Al_2O_3, AlN, Si_2O_2 and other materials.

Cermet coatings have been extensively investigated and are still widely researched due to their high solar absorptance, low IR emittance, and good thermal stability for mid-and high-temperature applications such as concentrated solar power (CSP) systems for solar thermal power generation and solar thermoelectric generators (STEGS). The mid-temperature solar selective solar selective coatings are used for industrial process heat desalination and solar hot water applications. Coatings that are thermally stable in the range of 100-400°C are called mid-temperature solar selective coatings and coatings stable above 400°C (in air and vacuum) are called high –temperature solar selective coatings.

2.1. EVAPORATION

Sputtering and evaporation are two basic methods of thin film deposition. They are widely deployed and require high vacuum systems. The principle of evaporation is to heat the source material up to a sufficiently high temperature to vaporise it, and let it condense on the substrate to form a layer of thin film. This method (both thermal and electron beam evaporation) is widely used in thin film deposition and has advantages that include high deposition rate, production of fine particles of many materials and it is a simple low cost process [2.1-2.5]. The main drawback of the evaporation method is that it is not suitable for large area deposition of solar selective coatings due to poor growth rate control, presence of large number of pin holes and the thin films do not bond well with the substrate. It is also hard to evaporate the materials with high melting points such as platinum (Pt) and molybdenum (Mo). Table 2.1 shows the absorptance, emittance and thermal stability of various solar selective coatings deposited by evaporation.

Material	Subst.	α	ε(100°C)	Stability (°C)	**Refs.**
Ge	Glass	>0.95	0.48 (240°C)	-	Mattox & Kominiak [2.8]
PbS	,,	>0.95	0.14 (240°C)	-	,,
Si	,,	0.70	-	-	,,
PbS	Al	0.95	-	-	McMohan& Jasperson [2.9]
PbS	Al	-	-	-	Marchini & Gandy [2.10]
(Ge or PbS)-SiO	Al, Ni, Cr	0.79-0.94	0. 01-0.11(127°C)	-	Flordal & Kivaisi [2.11]
PbS & ZrO_2 ARC	-	-	-	-	Martin [2.12]
Au-SiO_2	Glass	0.88 ± 0.01	0.014 ± 0.005	-	Brunger [2.13]
Cu-SiO_2 & SiO_2 ARC	Cu or glass	0.92	0.02 (50°C)	-	Zhang
Co-Al_2O_3 & Al_2O_3 ARC	Mo	0.90	0.02 (50°C)		Zhang & Mills [2.24]
Ni-Ni-SiO_2-SiO_2	Quartz, SS	0.90	0.07 (300°C)	420°C (40 h) in vacuum 515°C (12 h) in vacuum	Okuyama [2.26] ,,
Ni-Ni-MgO- SiO_2	Quartz, SS	0.88	0.05 (300°C)	420°C (40 h) in vacuum 515°C (12 h) in vacuum	Okuyama [2.26] ,,
Cr-Al_2O_3	Cu coated glass	0.92	0.03 at R.T.	500°C (100 h) invacuum	McKenzi [2.27]
Ni-Al_2O_3 & SiO_2 ARC	Mo-Ni-SS	0.94	0.07 (100°C)	500°C (100 h) in air	Sathiaraj
Co-Al_2O_3 Al_2O_3 ARC	Ni	0.94	0.04 (100°C)	-	Niklasson& Granqvist [2.7]
Al_2O_3-Mo-Al_2O_3	Molybdenum	0.85	0.11 (500°C)	- 400 in air 920°C (500 h) invacuum	,, Schmidt & Park [2.28] ,,
Al_xO_y/Pt /Al_xO_y	Glass, Si & Cu	0.94±0.01	0.06 ±0.01(82°C)	-	Nuru [2.31]
Ni/Ni-Al_2O_3	Cu	0.94	0.22 (150°C)	300 in air	Craighead [2.32]
Ni/Ni-Al_2O_3	Quartz	0.96	0.22 (150°C)	500 (100 h) in air	,,
Pt/Pt- Al_2O_3	Cu	0.94	0.19 (150°C)	400 in air	Craighead [2.33]
Pt/Pt- Al_2O_3	Quartz	0.94	0.19 (150°C)	600 (300 h) in air	,,
Graphite	Cu, Ni, Ti, &	0.71-0.80	0.01 - 0.02	300 in vacuum 277 in vacuum	McKenzie [2.23]
Al-AlN& AlN ARC	Si	0.90	0.06	-	Yin [2.18]
Ag/TiO_2	-	-	-	-	Jahan Smith [2.20]
CuO	SS	0.93	0.16	200 in vacuum	Marquez [2.21]
Cu-SiO_2/Cu	Ag	0.93	0.05	-	Garnich & Sailer [2.22]
Black Chrome	Glass	0.80	0.05		Harding [2.14]
Te & Se	Cu Au, Cr, Mo & Cu	0.90-0.92	0.02-0.05		Peterson & Cocks [2.17]

Table 2.1 Solar selective coatings prepared by evaporation

Evaporation approach was first studied by Hass et al. [2.6] to design a mid-temperature PVD solar selective coating. They have deposited germanium on top of Aluminium substrate and reduced the reflectance of opaque Al from 90% to 40% at 430 nm. Further addition on SiO on top of the Ge coating resulted in zero reflectance at 600 nm.

Niklasson and Granqvist developed a single layer Co–Al_2O_3 cermet with Al_2O_3 antireflection coating by vacuum co-evaporation of Co and Al_2O_3 for mid-temperature selective solar absorber application [2.7]. Absorptance of 0.94 and emittance of 0.04 at 100°C have been obtained for an optimized coating having 70nm of Co–Al_2O_3 (58 vol% Co) on a Ni or Al reflector with a 70nm Al_2O_3 antireflection coating. The high absorptance was achieved without composition grading and surface roughening.

Mattox and Kominiak used various narrow band gap semiconductors (i.e., Si, Ge and PbS) as mid-temperature solar selective absorbers because they absorb in the solar spectrum and are transparent in the infrared region [2.8]. They investigated the effect of surface morphology on

the absorptance of Si, Ge and PbS coatings. It was observed that coatings with high absorptance have a very rough surface morphology when compared to the reflecting coatings. Absorptance greater than 0.95 was obtained for Ge and PbS coatings, whereas, Si coatings exhibited very low absorptance (0.70). The emittance values at 240°C of the Ge (ε =0.48) and PbS (ε =0.14) coatings were also very high resulting in very low solar selectivity.

McMohan and Jasperson also developed mid-temperature PbS solar selective absorbers without any antireflection coating (ARC) on Al substrates, which exhibited high solar selectivity [2.9]. High solar absorptance (0.95) was achieved for 100 nm thick PbS coating as compared to Si and Ge, where the optimum thickness was in the range of 1-10μm. The reduction in film thickness for PbS is due to its large absorption coefficient when compared to Ge and Si. In addition, PbS is a direct bandgap semiconductor, whereas Ge and Si are indirect band gap semiconductors. The high solar selectivity of the PbS coatings has been attributed to a unique surface morphology, which reduces the front surface reflection [2.68].

The effect of PbS film thickness on the absorptance and emittance of mid-temperature PbS-Al coatings was investigated by Marchini and Gandy [2.10] [2.69]. They have demonstrated both theoretically and experimentally that the optimum coating thickness to achieve high solar selectivity is in the range of 300–800 A. Unfortunately, all semiconductor materials have high refractive index, which resulted in high front surface reflection [2.8]. In order to reduce the front surface reflection, an antireflection coating must be deposited on top of the semi-conductor layer.

Flordal and Kivaisi developed Ge and PbS semiconductor selective solar absorbers with silicon monoxide antireflection coating on different metal substrates (i.e., Al, Ni and Cr) [2.11] for mid-temperature application. Ge–SiO and PbS–SiO coatings deposited on various metal substrates (Al, Ni and Cr) exhibited absorptance in the range of 0.79–0.94 and emittance in the range of 0.01–0.11 at 127 °C.

Martin et al. prepared PbS thin films with ZrO_2 antireflection coating by different routes such as ion beam sputtering, electron beam evaporation and thermal evaporation and compared the optical properties of these coatings [2.12]. Thermally evaporated PbS coatings exhibited very high absorption when compared to the sputtered and electron beam evaporated coatings. This is due to the porous surface texture of the mid-temperature thermally evaporated solar selective coatings [2.72].

Brunger embedded gold in SiO_2 matrix via co-evaporation of Au and SiO_2 by electron beam Evaporation [2.13]. A very low thermal emittance of 0.014 ± 0.005 at 100°C was obtained from a thermal radiation experiment compared with the radiation of a blackbody.

G.L. Harding developed evaporated black chrome as an alternative for electroplated black chrome coatings for mid-temperature solar selective coating [2.14]. He reported that the evaporated black chrome exhibited an absorptance of 0.80 and an emittance of 0.05 at 100°C with thermal stability of 200°C in vacuum [2.14].

Even though black chrome coatings have been in use for several years, their properties were poorly understood until they were studied by Granqvist and Niklasson [2.15]. They were the first to report the optical properties of ultrafine chromium particles prepared by evaporation method. The spectral selectivity of these coatings is comparable to that of the best electroplated black chrome coatings [2.15]. The ultrafine chromium particles exhibited high absorptance in the solar spectrum and low emittance in the infrared region.

Kivaisi studied the optical properties of selectively absorbing chromium films deposited at an oblique angle of incidence for mid-temperature applications [2.16]. The coating consists of a high concentration of metallic chromium surrounded by a very thin film of chromium oxide. Unlike gas evaporation (i.e., evaporation of chromium in the presence of oxygen) or co-evaporation (evaporation of chromium and its oxide), the chromium oxide formation in this coating is due to residual oxygen gas present in the vacuum chamber. This coating exhibited high absorptance in the solar spectrum and was transparent in the infrared region.

Peterson and Cocks developed semiconductor solar absorbers with high solar selectivity for mid-temperature applications. Tellurium and Selenium on various metal substrates were prepared by angular vapor deposition [2.17]. Tellurium coatings deposited on Au, Al and Cu substrates exhibited absorptance in the range of 0.90-0.92 and emittance in the range of 0.03-0.06 at 100°C.

Yin et al. used cathodic arc evaporation method to prepare mid-temperature Al–AlN and a-C:H-SS cermet coatings on silicon and glass substrates respectively [2.18] . The homogeneous Al–AlN cermet with AlN antireflection coating exhibited an absorptance of 0.90 and emittance of 0.06 at room temperature. Whereas, a-C:H-SS cermet with a-C:H antireflection coating deposited at macroparticle filtered condition exhibited very low reflectance in the visible region . However the cathodic arc method has one major

disadvantage: i.e., the emission of macroparticles of cathodic metal, which influences the optical properties of the coatings [2.19].

Jahan and Smith investigated the angular selective optical properties of mid-temperature Ag/TiO_2 cermets [2.20]. TiO_2 coatings were deposited by oblique angle deposition using a filtered cathodic arc and in a magnetron sputtering system. The metallic Ag was co-deposited by thermal evaporation. They have reported that the cathodic arc evaporated coatings showed better solar selective results than the sputtered coatings. This is due to the different microstructure of the oblique oxide obtained from cathodic arc evaporation.

Marquez et al. prepared mid-temperature CuO coatings by cathodic arc depositions with absorptance of 0.93 and emittance of 0.16 at 300°C on steel substrates [2.21]. The cathodic arc evaporated CuO coating exhibited solar selectivity of 5.8, which is in good agreement with the sputter deposited CuO coatings ($\alpha/\varepsilon = 7.5$).

Cu-SiO_2/Cu-cermet selective absorbers for mid-temperature solar photothermal conversion were developed by Garnich and Sailer [2.22]. The cermet coating was prepared by vacuum co-evaporation on glass substrates gave solar absorptance higher than 0.93 and emittance less than 0.05. Tandem films consisting of this cermet and a copper reflector exhibit thermal stability up to at least 550 K and calculated Carnot photothermal conversion efficiency up to 0.3.

D.R. McKenzie [2.23] conducted a study on the effect of substrate on graphite and other solar selective surfaces consisting of a substrate of copper, titanium, silver, or nickel underlying a single layer of material of refractive index $N = n + ik$. Copper is shown to be slightly superior to silver, and both are shown to be superior to nickel for operating temperatures of 200°C. The absorptance and emittance properties of graphite films on copper, silver, nickel, and titanium are found to be $\alpha \approx 0.7$ and $\varepsilon \approx 0.06$. Graphite films on copper and silver are candidates for mid-temperature evacuated solar selective coatings.

Q.C. Zhang and D.R. Mills [2.24] designed high temperature solar selective absorbers with cermet film structures composed of two cermet sublayers, each having a different metal volume fraction, located between a conventional metal reflector and a dielectric anti-reflection layer. The Cu-SiO_2 double layer cermet with SiO_2 antireflection coating designed by co-evaporation of Cu and SiO_2 had the best predicted ratio of absorptance to normal emittance α/ε of 46 at room temperature.

From computer modelling calculations using published experimental dielectric functions of Co-Al_2O_3 cermets, the authors clearly showed that the double layer cermet rather than one enhance the performance of the selective absorber. The Co-Al_2O_3 cermets exhibit high photothermal conversion efficiency with concentration factors of 8-10. An absorptance of 0.90 and normal emittance of 0.024 at 50°C (α/ε = 37) was obtained for a film composed of two cermet sublayers on a Mo reflector with an Al_2O_3 antireflection layer [2.25].

By selecting Ni as the inclusion, the thermal stability of SiO_2-based cermet coatings was improved by Okuyama et al. for high-temperature applications [2.26]. Ni-MgO and Ni–SiO_2 cermets were prepared by evaporation of pressed mixtures of Ni and SiO_2 /MgO, both with SiO_2 anti-reflection coating on quartz plates and stainless steel substrates. The complex refractive index was calculated by fitting a model to the transmittance and reflectance data. Absorptance values of 0.88 and 0.90 were achieved for Ni-MgO and Ni–SiO_2 cermets respectively. Both coatings were thermally stable in vacuum at 420 °C for 40 hours and at 515°C for 12 hours, they showed little spectral or mechanical degradation after annealing at these conditions.

D.R. McKenzie developed several cermet coatings that include Au–Al_2O_3, Ag–Al_2O_3, Cr–Al_2O_3, Cr–Spinel and Cu–Spinel for evacuated tube collectors applications [2.27]. A high absorptance greater than 0.90 was achieved by grading the composition of the cermet coatings and the emittance was less than 0.05 at 100°C. From the various cermet coatings, the Cr– Al_2O_3 cermet emerged as the best candidate for CSP applications because of its good thermal stability (500°C for100h) in vacuum [2.27].

Multilayer coating systems consisting nominally of one quarter-wave thick Mo and MgF_2 (MgF_2/Mo/CeO_2 on Mo, MgF_2/Mo/MgF_2/Mo/MgF_2 on Mo, MgF_2/CeO_2/Mo/MgF2/CeO_2 on Mo, and Al_2O_3/Mo/Al_2O_3/Mo/Al_2O_3/Mo/Al_2O_3 on Mo) deposited by electron-beam evaporation are stable to 540°C in vacuum with α = 0.85-0.91 and ε (260°C and 538°C) = 0.06-0.16 . Au/MgF_2 or CeO_2 cermet or multilayer films may also be of interest because of the performance and stability of the Mo/MgF_2 films.

A well-known example of a multilayer absorber is Al_2O_3–Mo–Al_2O_3, also known as AMA coating, which was developed for high-temperature applications by Schmidt and Park [2.28]. The AMA multilayer absorber coating has been developed for high-temperature space borne applications [28-29]. A semi-transparent Mo layer (20nm thick) was sandwiched between

two Al_2O_3 dielectric layers. The AMA coating exhibited an absorptance of 0.85 and emittance of 0.22 at 1000°C and 0.11 at 500 °C. The coatings deposited on Mo substrate were thermally stable in vacuum at 920 °C for 500h. In order to avoid the usage of costly Mo substrate, the coatings were deposited on Mo coated stainless steel substrates.

At temperatures of 900 °C, the AMA coating on Mo-coated SS substrate degraded, whereas the coating on Mo substrates started degrading at 1050°C. Auger electron spectroscopy analysis indicated that the stainless steel samples failed because of the diffusion of Fe and Cr from the stainless steel substrate [2.29]. The AMA coating had good thermal stability in vacuum, but exhibited limited durability when exposed to air (thermally stable in air at 400 °C for 24h). Based on the AMA design, various other multilayer absorbers using different metals (e.g.,Mo, W, Al, Hf, Ni) and dielectric layers (e.g., Al_2O_3, HfO_2, SiO_2, AlN) have been developed for high-temperature applications [2.30] .

Nuru et al. employed ellipsometric measurements and optical simulation to optimize and deposit $Al_xO_y/Pt/Al_xO_y$ multilayer spectrally selective coatings for solar thermal applications [2.31]. Spectrally selective $Al_xO_y/Pt/Al_xO_y$ multilayer absorber coatings were deposited onto corning 1737 glass, Si (111) and copper substrates using electron beam (e-beam) vacuum evaporator at room temperature. The optimized multilayer coatings exhibited high solar absorptance $\alpha \sim 0.94 \pm 0.01$ and low thermal emittance $\varepsilon \sim 0.06 \pm 0.01$ at 82 °C [2.31].

Craighead et al. developed high-temperature solar selective coatings of spherical Ni particles (diameter 5-10nm) embedded in an Al_2O_3 matrix and Pt–Al_2O_3 cermets on fused quartz substrates by controlled co-evaporation method. The optical properties of the Ni/Al_2O_3 composites measured over the range of the solar spectrum are in good accord with the predictions of Maxwell-Garnett theory provided the Ni volume fraction is < 0.2. The electron diffraction studies indicated that the Ni particles were crystalline and aluminium oxide was amorphous in nature; whereas, the pattern for Pt–Al_2O_3 showed only diffused rings, which is typical of an amorphous solid [2.32].

The cermet coatings deposited with a graded composition exhibited an absorptance of 0.94 and emittance of 0.10 at 150 °C. Ni–Al_2O_3 coatings deposited on Cu substrate were thermally stable in air up to 400°C and the coatings deposited on Ni coated fused quartz substrates were stable at 500 °C for 100h [2.32]. Pt–Al_2O_3 coatings deposited on Pt coated fused quartz substrates exhibited better stability than the Ni–Al_2O_3 coating on Ni coated fused quartz

substrates. The Pt–Al_2O_3 coatings showed no degradation in the optical properties even after heating the coatings in air at 600°C for 300h [2.32].

Craighead et al. [2.33] produced high temperature graded index films of coevaporated Pt–Al_2O_3 overcoated with a microscopically textured layer of SiO_x. The Pt and Al_2O_3 were deposited from independently controlled electron beam sources. A thin Pt layer (100nm thick) was deposited on top of a heated quartz substrate. By continuously varying the deposition rates of Pt and Al_2O_3, a graded Pt–Al_2O_3 cermet coating was deposited on top of the Pt layer [2.33]. The solar absorptivity of this graded refractive index surface is shown to be as high as 0.98 and the addition of the textured SiO_x antireflection coating increased the absorptance from 0.94 to 0.98.

2.2 SPUTTERING

Sputtering is a process that the atoms are ejected due to the bombardment of energetic particles on the source material and then deposited on the substrate to form a thin film. Compared with the evaporation, sputtering is easier to control the accuracy. In addition, the thin film by sputtering is more uniform and has better bonding with the substrate than the films deposited by evaporation. Magnetron sputtering has been applied on the solar selective coating due to its better control of the composition and thickness of the thin film, regardless of higher cost. The solar selective coatings prepared by sputtering include Al_2O_3/M-Al_2O_3 (M, metals include Ni, Co, Mo, Pt), and M-AlN, etc. Table 2.2 shows the absorptance, emittance and thermal stability of various solar selective coatings deposited by sputtering.

L. Rebouta et al. [2.34] conducted a study on solar selective coatings based on double Al_2O_3:W cermet layers and AlSiN/ AlSiON bilayer structures prepared by magnetron sputtering. Both were deposited on stainless steel substrates using metallic tungsten (W) layer as back reflector, followed by two absorption layers for the absorption of the solar energy, and by an antireflection (AR) layer. The structures were simulated by the SCOUT software using suitable dielectric function models. The layers showed good solar selective properties (solar absorptance of 94-95% and emissivity of 8-9% at 400 °C) as well as, good thermal stability.

Material	Subst.	α	Emittance ε(100°C)	Stability (°C) Air	**Refs.**
AlSiN/AlSiON	SS	0.94-0.95	0.8- 0.9(400°C)	-	Rebouta [2.34]
AgAl- Al_2O_3	Si, C or Quartz	-	-	500 (260h) in nitrogen	Tua [2.35]
W-Al_2O_3	-	-	-	580 in vacuum	Antonaia [2.36]
Pt-Al_2O_3 with Al_2O_3 ARC	Pt Cr, Mo coated glass	>0.90	<0.10	600 (100h) in air	Thornton[2.38-2.40]
Al_2O_3/ Pt-Al_2O_3 /Al_2O_3	Pt Cr, Mo coated glass	>0.90	<0.10	600 (100h) in air	Thornton[2.38-2.40]
Al_2O_3/M/Al_2O_3/R	-	>0.90	<0.10	500-600 in air	Thornton [2.41]
M is Cr, Ni, Pt-Al_2O_3	-	-	-	650-700 in vacuum	Thornton [2.41]
Au-MgO	Mo coated SS	0.90-0.93	0. 04-0.10 at100°C	400 in air	Fan,Zavaracky[2.45]
Ni-MgF_2	Ni	0.96	0.13 at 100°C	450 (446h) in air	Mast [2.42]
Pt-Al_2O_3 with Al_2O_3 ARC	Mo or W coated SS	0.92	0.14 at 300°C	400 (50-60h) in air	Vien [2.43]
	Mo or W coated **SA**	0.92	0.14 at 300°C	600(36-50h) in air	”
Cr-Cr_2O_3 with Cr_2O_3 ARC	Ni coated SS	0.92	0. 08	300 (64h) in air	Fan & Spura [2.46]
Cr_xO_y-Cr-Cr_2O_3	Cu	0.89-0.91	0.05-0.06	275 (50h)	Barshilia [2.47]
				500 (2h) in vacuum	”
Cu-Al_2O_3	Cu	0.86-0.90	0.03 at R.T.	<300 in vacuum	Mckenzie [2.51]
Ni- Al_2O_3 with SiO_2 ARC	Mo-Ni-SS	0.94	0.07 at 100°C	500 (1000h) in air	Sathiaraj [2.44]
Cr-Cr_2O_3	Cu	0.92-0.96	0.05-0.08	300-400(1h) vacuum	Yin [2.48]
Ag- Al_2O_3	Cu	0.94	0.04	<250 vacuum	Barshilia [2.52]
Metal carbide	Bulk Cu	0.76-0.80	0.02-0.03	400 (120h) in vacuum	Harding [2.53-2.54]
Metal silicide	Bulk Cu	0.75-0.81	0.02-0.03	400(100-400)vacuum	”
Al_xO_y-Al-Al_xO_y	Cu	0.95-0.97	0.05-0.08 (82°C)	400 (2h) in air	Barshilia [2.64]
Al_xO_y -Al-Al_xO_y	Mo	0.93-0.95	0.05-0.09 (82°C)	400 (2h) in air	Barshilia [2.64]
				800 (2h) in vacuum	”
Cu- SS-a-C	Glass	>0.90	<0.05(300°C)	400 (4h) in vacuum	Wyon [2.56]
TiN_x	Ag coated glass & SS	0.86-0.88	0.024-0.033 (127°C)	600 (500h) in vacuum	Blickensderfer[2.57]
ZrN_x	Ag coated glass & SS	0.86-0.88	0.024-0.033 (127°C)	600 (500h) in vacuum	”
ZrC_xN_y	Ag coated glass & SS	0.86-0.88	0.024-0.033 (127°C)	600 (500h) in vacuum	”
ZrO_xN_y	Ag coated glass & SS	0.88-0.93	0.08-0.93 (327°C)	600 (500h) in vacuum	”
TiAlN/TiAlON/Si_3N_4	Cu	0.93-0.94	0.05-0.08 (82°C)	550 in air 600-vacuum	Barshilia [2.58-2.59]
TiAlN/TiAlON/Si_3N_4	SS	0.93-0.95	0.15-0.17 (82°C)	550 in air	Barshilia [2.60]
TiAlN/AlON	Cu	0.93-0.94	0.05-0.06 (82°C)	550 (2h) in air	Barshilia [2.62]
				800 (2h) in vacuum	”
NbAlN/NbAlON/Si_3N_4	Cu	0.93-0.95	0.07 (82°C)	500 (2h) in air	Barshilia [2.63]
				600 (2h) in vacuum	”
Al_2O_3/Cu/Al_2O_3/AlCuFe homogeneous/Al_2O_3	Cu coated Si wafer	0.89-0.90	0.04-0.06 (400°C)	400 (450h) in air	Eisenhammer [2.67]
					”
Al_xO_y-AlN_x-Al	Quartz glass	0.94-0.97	0.07 (82°C)	400-600(30 min) in vacuum	Yue [2.69]
					”
Mo/HfO_x/Mo/HfO_2	Cu	0.90-0.92	0.07-0.09 (82°C)	400 (2h) in air	Selvakumar [2.68]
				600 (2h) in vacuum	”
$MoSi_2$/Al_2O_3		0.92	0.15(1100K)	-	Schon[2.70]
Pt-Al_2O_3		0.95	0.10	600 (400h)	Schon[2.70]
Ge or Si-CaF_2	Quartz	0.70	0.07 (500°C)	<500 in vacuum	Gittleman [2.71]
Fe-Al_2O_3 with Al_2O_3 ARC	SS	0.95	0.14 (427°C)	400-500 (36h) Ar+H_2	Sella [2.72]
Fe-Al_2O_3 with Al_2O_3 ARC	Superalloy (SA)	0.95		600 (Ar+H_2)	Sella [2.72]
W/WAlN/WAlON/Al_2O_3	SS	0.958	0.08	500 (150h) in air	Atasi Dan [2.73]
Al_2O_3-WC	SS	0.94	0.08	600 in air	X-H Gao [2.74]
SS/TiC-WC/Al_2O_3	SS	0.92	0.11	500 (100h) in vacuum	X-H Gao [2.75]
AlSiN/AlSiON/$AlSiO_y$	SS	0.93-0.94	0.07-0.1 (400°C)	-	Rebouta [2.76]
SiO_2- Si_3N_4-W-SiO_2-W	-	>0.95	<0.1	600 in air	Wang [2.78]
ZrC/ZrO_x/Al_2O_3	SS	0.92	0.12	-	Gao [2.80]

Table 2.2: Solar selective coatings prepared by sputtering

Thermal stability of Ag or AgAl nanoparticle embedded alumina matrix was comprehensively investigated by Tua et al. [2.35]. Ag- or AgAl-Al_2O_3thin films were deposited onto (100) silicon, porous carbon grids or quartz by a magnetron sputtering system at room temperature. The optical analysis demonstrated the AgAl-Al_2O_3 cermet films possess excellent thermal tolerance even after annealing at 500°C for 260 h under nitrogen ambient. It was proposed that the enhanced thermal stability was ascribed to the metallic Al that diffused out of AgAl alloy nanoparticles after the low-temperature pretreatment in air, and got

oxidized on the interfacial sites between the particles and the alumina matrix. The freshly generated alumina as acting as covering layer was pinned against the matrix could prevent silver element from migrating so as to maintain the expected optical properties.

Zhang Qi-Chu and Mills D. R studied the M-AlN solar selective coating created by d.c. sputtering, and showed that the absorptance is 0.92~0.94, the emittance is 0.08~0.10 (350°C).

Antonaia et al. investigated stability of multilayer graded W-Al_2O_3 cermet based solar coating fabricated by magnetron sputtering technique for receiver tube operating at high temperature [2.36]. The significant characteristics that emerged in the study were the partial oxidation of the tungsten nano-particles inside the cermet forming shells of WOx, the nucleation of a nano-crystalline porous alumina g phase in the matrix of the prevailing amorphous on eand the phase transition from b to a of the tungsten back-reflector. All these phenomena were responsible for the coating reflectance modification promoted by the increased temperature [2.36].

The temperature-induced ageing mechanisms and long-term stability of solar thermal absorbers having aluminium substrate with and without anodized aluminium oxide layer were investigated Kotilainen et al. [2.37]. A thin Al layer was used to act as an IR reflector on anodized aluminium oxide layer. The absorbers studied were industrial, sputtered chromium-based absorber coatings.The absorbers were aged by means of prolonged and extended thermal accelerated ageing studies at 248–308 C. The relation between optical degradation and ageing mechanism was studied using optical modelling and simulation with CODE Coating Designer. The results clearly demonstrated the effect of substrate material on the long-term stability of the absorber at intermediate temperatures.

Thornton and Lamb investigated three coating configurations of high temperature Pt–Al_2O_3 solar selective coatings: (1) Pt–Al_2O_3 cermet with a linearly graded platinum content and an Al_2O_3 antireflection coating, deposited on platinum coated glass, (2) Pt–Al_2O_3 coating with a uniform platinum content and an Al_2O_3 antireflection coating, prepared on Pt, Cr and Mo coated glass and (3) Al_2O_3/Pt-Al_2O_3/Al_2O_3 coating deposited on Pt, Cr and Mo coated glass [2.38-2.40].

The authors deposited the Pt–Al_2O_3 coatings using two cylindrical-post magnetron sputtering guns, one of which contains an alumina target and other contains an electro- plated platinum

target. All the three configurations exhibited absorptance greater than 0.90. Emittance less than 0.10 was obtained for the graded and AMA configurations, while, for the uniform cermet the emittance was 0.13 at room temperature. Graded, uniform and AMA coatings deposited on platinum coated glass substrates were stable in air at 600°C for 100h. Thornton and Lamb report that though the coatings deposited on Cr or Mo coated glass substrates were less stable; they showed promise for many applications in the temperature range of 300-500°C [2.39].

Thornton and Lamb also investigated the thermal stability of $Al_2O_3/M/Al_2O_3/R$ coatings with M layers of Mo, Cr, Ni, Ta and Pt–Al_2O_3 cermet and R layers of the same metal as the M layers, except for Pt–Al_2O_3 where they were Cr or Mo [2.41]. The coatings were deposited on glass plate substrates using planar magnetron sputtering sources. The Al_2O_3 layers were deposited by both direct RF sputtering of alumina and also by the reactive sputtering of aluminium targets. The thermal stability of this multilayer absorber coating mainly depends on the method of preparation of the Al_2O_3 layer. The multilayer absorber coatings were heat-treated in air and vacuum over the temperature range of 300–700°C for periods from 8 to about 1000h.

The authors [2.41] report that the high temperature solar selective $Al_2O_3/M/Al_2O_3/R$ coatings with reactively sputtered Al_2O_3 layers and M layers of Cr and Ta were stable up to 300°C and those with Ni, Mo or Pt–Al_2O_3 layers were stable in air/vacuum at 400–450°C. However, Al_2O_3 layers deposited by RF sputtering of alumina with M layers of Cr, Ni, or Pt–Al_2O_3 layers were stable up to 500–600°C in air and 650–700°C in vacuum. Correspondingly, detailed studies on graded Pt–Al_2O_3 cermet coatings on glass substrates with Pt interlayer have been reported by Thornton and Lamb [2.41]. The heating of this coating in air up to 600°C indicated an increase in emittance to approximately 0.25 from approximately 0.05 for reactively sputtered Al_2O_3 based coatings. The RF sputtered based cermet coating showed less emittance when compared to reactively sputtered Al_2O_3 based coating

Ni–MgF_2 single layer cermet deposited by sputtering on Ni substrates exhibited an absorptance of 0.96 and emittance of 0.13 at 100°C as reported by M. Mast et al. [2.42]. There was no significant degradation in the optical properties even after the coatings were heated in air at 450 °C for 446h; the Ni–MgF_2 cermet is consequently a high-temperature solar selective coating.

Vien et al. prepared single layer Pt–Al_2O_3 cermet coatings on SS and superalloy substrates by RF co-sputtering [2.43]. The coatings exhibited an absorptance of 0.92 and an emittance of 0.14 at 300°C. The coatings deposited on SS and superalloy substrates were thermally stable at 400 and 600°C in hydrogen atmosphere for 50-60h and 36-50h respectively. They are therefore considered high temperature solar selecting coatings.

Ni–Al_2O_3 selective cermet coatings were prepared by RF sputtering for photothermal conversion up to 500°C in studies conducted by T.S. Sathiaraj et al [2.44]. The single layer coatings were prepared on different substrates such as Ni plated SS, Mo coated SS, Cu coated SS and Mo coated nickel plated SS. The 65nm thick graded Ni–Al_2O_3 cermet coatings that have 78 nm thick SiO_2 antireflection coating deposited on molybdenum or nickel plated stainless steel substrates resulted in an absorptance of 0.94 and an emittance of 0.07 at 100°C. The Ni–Al_2O_3 cermet coatings without SiO_2 antireflection coating were stable in air only up to 400°C where as those with SiO_2 antireflection coating deposited on Mo coated or Ni plated SS substrates were thermally stable in air at 500°C for 1000h.

Fan and Zavaracky used MgO as a dielectric medium and developed black high temperature Au–MgO selective solar absorber coatings by RF sputtering method. The Au–MgO coatings were deposited on aluminum, copper, SS and SS substrate coated with molybdenum using a hot-pressed target with ¾ vol MgO and ¼ vol Au [2.45]. The absorptance attained for the different coatings was in the range of 0.90–0.93 while the emittance was 0.04 and 0.10 at 100 °C for coatings deposited on Cu and SS substrates, respectively. The coatings on Cu substrate were thermally stable in air at 200 °C, 300 °C for SS and Al substrates and 400 °C for Mo coated stainless steel substrate [2.45].

Fan and Spura developed mid-temperature sputter deposited chromium oxide cermet coating and compared with electro- deposited black chrome coating [2.46]. They found that the electro- deposited coatings are actually Cr/Cr_2O_3 cermets comparable in composition and microstructure to the sputtered films. The sputter deposited Cr/Cr_2O_3 with Cr_2O_3 antireflection coating deposited on nickel coated stainless steel (SS) substrates exhibited α/ε of 0.92/0.08. The coatings were thermally stable in air at 300°C for 64h.

Barshilia et al. developed Cr_xO_y/Cr/Cr_2O_3 multi- layer absorber coating for mid-temperature solar thermal applications [2.47] . To deposit the multilayer absorber coating on Cu substrates the Cr targets were sputtered using asymmetric bipolar pulsed direct current (DC) generators

in Ar + O_2 and Ar plasmas. The optimized multilayer absorber coating exhibited high absorptance (0.89–0.91) and low thermal emittance at 82 °C (0.05–0.06). The coatings were thermally stable in air at 300 °C and in vacuum 500°C for 2h [2.47]. Accelerated aging tests indicated that the coatings deposited on Cu substrates were stable in air up to 250h at 250 °C. At higher temperatures, the absorptance decreased and the emittance increased considerably which was attributed to the formation of CuO, the oxidation of Cr crystallites and increased surface roughness.

Yin et al. have developed Cr–Cr_2O_3 cermet solar selective surface by direct current reactive sputtering. The multilayer cermet was a low–high–low metal volume fraction profile and in the optimization the target current was used as a control parameter [2.48]. The solar absorptance of the sputtered black chrome selective surface is in the range of 0.92–0.96 and the thermal emittance is 0.05–0.08 at 100°C. The coatings were thermally stable at 300–400°C for 1h in vacuum. Long time aging at 170°C suggested that the coatings are suitable for solar hot water applications [2.48]. The sputter deposited Cr–Cr_2O_3 coatings and electrodeposited black chrome have been found useful for solar water heating applications. In evacuated tubes at an application temperature of around 300°C, black chrome has been used for steam generation at low pressures [2.49-2.50]. However, for high-temperature applications black chrome coatings are not recommended since they undergo compositional changes [2.5].

In research work by McKenzie, graded Cu–Al_2O_3 cermets were developed by dual cathode DC magnetron sputtering for evacuated tube collector applications [2.51]. The solar selective Cu–Al_2O_3 cermet coatings exhibited absorptance in the range of 0.86–0.90 and emittance of 0.03 at room temperature. When the coatings were annealed in vacuum at 300°C, the solar absorptance decreased from 0.86 to 0.83. From this performance result of the thermal stability test, it is clear that the Cu–Al_2O_3 cermet coating can be used only for low-and mid-temperature solar applications.

Barshilia et al. prepared Ag–Al_2O_3 nanocermets solar selective coating for mid-temperature solar thermal applications using unbalanced magnetron sputtering [2.52]. The optical properties of the nanocermets are due to surface plasmon resonance, which is attributed to collective oscillations of conduction electrons of noble metal nanoparticles embedded in a dielectric matrix. In the optimization of the nanocermets, the authors found that by controlling the particle size, shape, concentration of particle in matrix, particle distribution

and local dielectric environment of the host matrix, the optical properties can be controlled. These Ag–Al_2O_3 coatings on Cu substrate exhibited a solar selectivity of 0.94/0.04, but low thermal stability (up to 250 in vacuum).

Harding developed various transition metal carbide and silicide coatings for solar thermal applications [2.53]. The metal silicides and carbides of chromium, iron, molybdenum, nickel, stainless steel, tantalum, titanium and tungsten were deposited by reactive sputtering on bulk and sputtered copper substrates [2.53]. The metal silicide coatings were also deposited on evaporated Ni and bulk stainless steel substrates. A solar absorptance of 0.76–0.80 and a thermal emittance of 0.02–0.03 were observed at room temperature for the homogeneous metal carbides prepared on bulk copper.

Similarly, the homogeneous metal silicides on bulk copper have α = 0.75-0.81 and ε = 0.02-0.03 at room temperature Harding [2.54]. These coatings were thermally stable at 400°C in vacuum. The absorptance values of the metal silicides deposited on sputtered copper, evaporated nickel and bulk stainless steel substrates are enhanced due to the low visible reflectance of these substrates. the stainless silicide deposited on bulk copper substrate exhibited absorptance of 0.81 and emittance of 0.02 at room temperature.

The coatings deposited on bulk and sputtered copper substrates exhibited different aging effects. No detoriation was observed after 250h at 250°C and 120h at 400°C in air for the films on bulk copper, where as the coatings deposited on sputtered copper began to detoriate slightly at 250°C The absorptance of the homogeneous metal carbide and silicide coatings was increased by grading the coating composition, i.e., the coating was highly metallic near the substrate and dielectric at the air–film interface. These graded metal carbide and silicide coatings exhibited absorptance in the range of 0.90–0.95 without affecting the emittance [3.55].

Wyon and Valignat developed a mid-temperature solar selective Cu/SS/a-C coating for use in evacuated collectors [2.56]. Non-reactive magnetron sputtering was used to successively deposit an opaque Cu layer, a thin film of stainless steel and an amorphous carbon layer on glass substrate. This coating exhibited absorptance higher than 0.90 and emittance less than 0.05 at 300°C. The coatings were thermally stable in vacuum at 400 °C for 4h [2.56]. At higher operating temperatures, interdiffusion between the layers and the outward diffusion of Cu and its subsequent oxidation resulted in degradation of the coatings.

Blickensderfer et al. developed high temperature solar selective tandem absorbers. The single layer coating comprised of a stainless substrate with a faintly oxidized surface, a thin sputtered coating of reflective silver and a selective absorber coating of sub stoichiometric zirconium or titanium nitrides, carbonitrides, oxynitride and oxycarbonitrides[2.57]. TiN_x, ZrN_x and ZrC_xN_y coatings have the best combination of good absorptance in the range of 0.86-0.88 and low emittance (0.024-0.033) at 127°C. ZrO_xN_y coatings exhibited high solar absorptance of 0.93 and high emittance of 0.19 at 127°C [2.57]. Heat-treatment of these coatings in air at 127°C for 300h resulted in a decrease in the solar absorptance, but they exhibited excellent thermal stability in vacuum at 700 °C for 500h [2.57].

Barshilia and Selvakumar developed a new generation TiAlN/TiAlON/Si_3N_4 high-temperature tandem absorber of using reactive DC magnetron sputtering [2.58-2.59]. this tandem absorber is designed in such a way that the TiAlN which is metallic in nature acts as the main absorber layer and TiAlON which has low metallic content acts as the second absorber layer. The TiAlN/TiAlON tandem absorber deposited on Cu substrate is nanocrystalline in nature and exhibited absorptance of 0.90 and emittance of 0.05 at 82°C. After depositing an armorphous antireflection coating of Si_3N_4 the solar selectivity of the tandem absorber was increased by 0.95/0.06.

Studies by the same authors on the thermal stability of the TiAlN/TiAlON/Si_3N_4 tandem absorber on Cu substrate report that this tandem selective coating is thermally stable in air up to 550 °C (2h) and up to 800 °C (2h) [2.60]. The higher thermal stability of the tandem absorber has been attributed to the fact that TiAlN acts as a diffusion barrier layer on Cu substrate and also the constituent layers are thermally stable at higher temperatures [2.60]. This coating concept has been granted a US patent (Patent no: 07585568) [2.61]. Based upon the successful demonstration of this coating concept, other tandem absorbers such as TiAlN/AlON, NbAlN/NbAlON/Si_3N_4 and TiAlN/CrAlON/Si_3N_4 for high-temperature solar selective applications have been developed by Barshilia and Selvakumar et al.

Spectrally selective TiAlN/AlON tandem absorbers were deposited on copper and stainless steel substrates by Barshilia and Selvakumar using a reactive DC/RF magnetron sputtering system[2.62] . The compositions and thicknesses of the individual component layers on copper substrate were optimized to achieve high absorptance (α = 0.931–0.942) and low emittance (ε = 0.05–0.06). The experimental spectroscopic ellipsometric data have been fitted with the theoretical models to derive the dispersion of the optical constants (n and k). The

tandem absorber deposited on Cu substrates exhibited high solar selectivity (α /e) of 0.946/0.07 even after heat treatment in air up to 600°C for 2 h. At 625°C, the solar selectivity decreased significantly on Cu substrates (e.g., α/ε 0.924/0.30). The tandem absorber on Cu substrates was also stable in air up to 100 h at 400 °C with a solar selectivity of 0.919/0.06.

Barshilia and Selvakumar [2.63] A new spectrally selective NbAlN/NbAlON/Si_3N_4 tandem absorber was deposited on copper substrates using a reactive direct current magnetron sputtering system. A high solar absorptance (0.956) and a low emittance (0.07) were achieved by gradually decreasing the refractive index from the substrate to the surface. The tandem absorber deposited on copper substrate exhibited high solar selectivity in the order of 13–15 even after heat treatment in air up to 500°C for 2 h. These tandem absorbers also exhibited high thermal stability (450°C) in air for longer durations (116 h). The onset of oxidation for the tandem absorber deposited on silicon substrates was 650°C, indicating a high oxidation resistance. The results of the present study indicate the importance of NbAlN/NbAlON/Si_3N_4 tandem absorber for high-temperature solar selective applications.

Barshilia and Selvakumar developed high temperature solar selective Al_xO_y/Al/Al_xO_y multilayer absorber coatings on copper and molybdenum substrates using a pulsed sputtering system [2.64]. A symmetric bipolar-pulsed DC generators were used to deposit the Al_xO_y/Al/Al_xO_y multilayer absorber coating. The compositions and thicknesses of the individual component layers were optimized to achieve high solar absorptance (α = 0.95–0.97) and low thermal emittance (ε = 0.05–0.08) at 82°C. The multilayer absorber deposited on Cu substrates exhibited high solar selectivity of 0.90/0.06 even after heat-treatment in air up to 400 °C for 2h. At 450 °C , the solar selectivity decreased significantly on Cu substrates (e.g., α/ε = 0.79/0.07).The coatings deposited on Mo substrates were thermally stable up to 800 °C in vacuum for 2h with a solar selectivity of 0.93/0.05.

Thermodynamically stable quasicrystal-forming alloys (i.e., AlCuFe, AlCuRu, and AlMnPd films) can be used as selective absorbers. Materials with an icosahedral point group or other crystals of forbidden rotational symmetries are referred to as ‘quasicrystals’ [2.65]. Quasicrystals exhibit high thermal and chemical stability and show no selective properties at all, but thin (10-12-nm) film stacks on a highly reflective substrate or in a cermet show the desired properties [2.66].

Sputtering thin films of AlCuFe and AlCuFeCr on very rough copper films and silicon has produced such absorbers. Dielectric AR coatings of alumina and float glass were necessary to give the required optical properties. Thin (10-nm) quasicrystal films sandwiched between dielectric layers on a copper substrate were predicted to have α=0.91 and ε= 0.05 at 100°C. Theoretically, quasicrystals can achieve high solar absorptance (>0.9) and low thermal emittance (<0.05 at 400°C) with high-temperature stability (500°C), they generally exhibit good oxidation and diffusion stability [2.66].

Eisenhammer et al. developed Al_2O_3 based quasicrystalline cermets for high-temperature solar applications [2.67]. Solar selective absorbers based on AlCuFe thin films (i.e., Al_2O_3/Cu/Al_2O_3/AlCuFe homogeneous/Al_2O_3) and a cermet of AlCuFe particles embedded in an Al_2O_3 matrix (Al_2O_3/Cu/Al_2O_3/ AlCuFe cermet/ Al_2O_3) were deposited on Cu coated Si wafers by sputtering method. The absorptance of the homogeneous films was found to be 0.89–0.90 and the emittance was 0.04–0.06 at 400 °C. Whereas, for the cermet layer, the α & ε values were 0.79 and 0.03, respectively, at 400 °C. The coatings were thermally stable in air at 400 °C for 100h.

Selvakumar and Bashilia investigated the possibility of designing a dielectric/metal/dielectric multilayer absorber coating of HfO_2 and molybdenum [2.68]. Solar selective coatings of HfO_x/Mo/HfO_2 deposited using a pulsed sputtering system on Cu substrate exhibited high solar absorptance (α = 0.90–0.92)and low thermal emittance (ε = 0.07–0.09) at 82°C, they were thermally stable up to 400°C for 2h in air. Above 400°C, α decreased drastically due to diffusion of Cu from the substrate and its subsequent oxide formation [2.68]. The Mo/HfOx/Mo/HfO_2 on SS substrates designed by addition of a thin Mo interlayer (40nm) in the HfOx/Mo/HfO_2 coating showed no significant changes in α & ε values after annealing at 500°C in air and at 800°C in vacuum for 2h.

Yue et al. [2.69] used both aluminum oxide and aluminum nitride dielectric materials to develop a solar selective AlxOy–AlNx–Al tandem absorber using DC reactive magnetron scattering for high-temperature applications. The coating deposited on quartz substrates exhibited absorptance (α) of 0.88–0.97 and emittance (ε) of 0.07–0.10 at 82°C. The coatings were thermally stable at 400–600°C in vacuum. Even after heating the coating at 550°C for 40h, the α & ε values were 0.98 and 0.12 respectively [2.69].

In a study based on metal/dielectric multilayers by Schon et al. Pt–Al_2O_3 and Al_2O_3/$MoSi_2$ multilayer cermet coatings were prepared by RF magnetron sputtering for high-temperature solar applications [2.70]. These coatings were optimized by computer simulations and the selectivity results evidently showed that the Pt–Al_2O_3 coatings are promising candidates for high-temperature solar thermal applications. The tetragonal-$MoSi_2$/Al_2O_3 multi-layers have solar absorptance up to 0.92 and emittance of 0.15 (1100 K). A high solar absorptance of 0.95 and emittance of 0.10 have been achieved for Pt–Al_2O_3 multilayers [2.70]. These coatings were thermally stable in air at 600°C for 400h, though this clearly indicates that Pt–Al_2O_3 cermets are promising candidates for high temperature solar thermal applications, they are not commercialized due to the high cost of platinum. Ni–Al_2O_3 cermet coating is an alternative for Pt–Al_2O_3 cermets in terms of cost and high-temperature optical performance [2.5].

Gittleman et al. produced composite semiconductors for mid-temperature solar selective coating by cosputtering CaF_2 with either Ge or Si on quartz substrate and measured their optical constants [2.71]. Their optical behaviour was described as being similar to that of the parent semiconductor, with the same energy gap but with a reduced, concentration dependent index of refraction. From the computed data, the solar absorptance and thermal emittance were found to be $\alpha \approx 0.7$ and $\varepsilon \approx 0.06$ with a weak dependence on composition, thickness and operating temperatures.

Sella et al. developed a low cost Fe–Al_2O_3 cermet with an Al_2O_3 antireflection coating for high-temperature solar thermal applications [2.72]. The coatings were deposited on SS substrates covered with or without tungsten or molybdenum. This three layer stack (Mo/Fe–Al_2O_3/Al_2O_3) exhibited high absorptance of 0.95 and low emittance of 0.06 at room temperature. The coating deposited on stainless steel substrate without Mo interlayer was stable up to 400–500°C, while the coating deposited on superalloy substrates (Nicral, IN 100) was stable up to 600°C in Ar + H_2 atmosphere [2.72] . Even though the cost of Fe–Al_2O_3 coating is very low, the thermal stability of the coating is poor when compared to the Pt–Al_2O_3 coatings.

Atasi Dan reports excellent durability of a colored W/WAlN/WAlON/Al_2O_3 tandem selective absorber achieved by increasing the number of layers [2.73]. The colored solar-thermal collectors can provide advantages of architectural integration over energy performance. The tandem absorber, fabricated by DC and RF magnetron sputtering on stainless steel substrates

showed a high solar absorptance of 0.948 and the low thermal emittance of 0.08 with a sky blue color appearance and exhibited excellent long-term thermal stability at 500 °C in air for 150 h. The selective performance of the coating can be stable more than 25 years. The humidity test confirms the significant moisture resistant of the coating.

Xiang-Hu Gao et al. conducted a study on the structure, optical properties and thermal stability of Al_2O_3-WC nanocomposite ceramic spectrally selective solar absorbers [2.74]. Traditional metal-dielectric composite coating deposited on SS substrate using magnetron sputtering was composed of low Al_2O_3 ceramic volume fraction (Al_2O_3(L)-WC) layer, high Al_2O_3 ceramic volume fraction (Al_2O_3(H)-WC layer) and Al_2O_3 antireflection layer. The Al_2O_3-WC nanocomposite ceramic successfully achieves the all-ceramic concept, which exhibits a high solar absorptance of 0.94, a low thermal emittance of 0.08 and good thermal stability at 600°C. In addition, the solar absorber coating is successfully modelled by a commercial optical simulation programme, the result of which agrees with the experimental results.

Xiang-Hu Gao et al. investigated the microstructure, chromaticity and thermal stability of SS/TiC-WC/Al_2O_3 spectrally selective solar absorbers prepared on stainless steel (SS) substrate by magnetron sputtering [2.75]. The coating consists of an absorptance layer (TiC-WC) and an Al_2O_3 antireflectance layer from substrate to top. The SS/TiC-WC/Al_2O_3 tandem coating exhibits excellent selective absorbing properties with a high solar absorptance of 0.92, low thermal emittance of 0.11 and a purple colour. Experimental results indicate that the coating is highly stable in vacuum at 500°C for 100 h with a good solar selectivity of 0.92/0.11.

Rebouta et al. report on solar selective absorbing coatings based on AlSiN/AlSiON/$AlSiO_y$ layers [2.76]. Coatings with a double absorbing layer based on AlSiN/AlSiON were deposited on stainless steel substrates by magnetron sputtering technique, with different Al:Si ratios. A tungsten layer was used as a back reflector and $AlSiO_y$ or SiO_x thin films were used as antireflection top layers. The samples were annealed in air at 400°C and vacuum at 580°C with the purpose to evaluate their oxidation resistance and thermal stability, which was subsequently correlated with the Al:Si ratio. Optimum results were achieved for an Al:Si ratio of 2.3:1,whereas for significantly higher Si content resulted in detrimental performance. The solar absorbance and thermal emittance for the optimized multilayer selective coatings is 93–94% and 7–10% (at 400°C), respectively.

Atasi Dan et al. report on enhancing spectrally selective response of W/WAlN/WAlON/Al_2O_3-based nanostructured multilayer absorber coating through graded optical constants [2.77]. The spectral properties of selective coatings can be tailored by carefully adjusting the composition and thickness of each layer. Based on the extensive analysis with TEM and phase modulated ellipsometry data using Cauchy absorbent dispersion model, Tauc-Lorentz and Bruggeman effective medium approximation model, the gradation in optical constants (refractive index-n and extinction coefficient-k) across the tandem architecture was established. The engineering of the optical properties of the multi-layer W/WAlN/WAlON/Al_2O_3 coating enables it to be an exceptional selective absorber coating, it exhibits a high absorptance of 0.958 and a low emittance of 0.08.

Wang et al. report on the design, fabrication and optical characterizations of high temperature free ultrathin multilayer selective solar coatings made of SiO_2-Si_3N_4-W-SiO_2-W stacks deposited by sputtering and chemical vapor deposition techniques [2.78]. The optical performance was optimized by the particle swarm optimization algorithm for this multilayer absorber, whose spectral selectivity is associated with the Fabry-Perot resonance and anti-reflection effects. FTIR measurements indicate excellent spectral selectivity with solar absorptance larger than 0.95 in the visible and near IR, as well as emittance less than 0.1 in the IR spectral regime with excellent thermal stability up to 600 °C in air.

Heras et al. studied Aluminium titanium oxynitrides as candidate materials for high temperature absorbers in solar selective coatings [2.79]. A set of individual $Al_yTi_{1-y}(O_xN_{1-x})$ layers with different oxygen content was prepared by cathodic vacuum arc (CVA) deposition. Sample microstructure and morphology undergo systematic changes from a columnar growth to spherical nanoparticle inclusions when the oxygen concentration is increased. The authors demonstrate that the optical properties of these films can be controlled in a wide range by transition from metallic to dielectric behaviour with increasing oxygen content. Complete (SSC), including a TiN layer as IR reflector, were designed by applying optical simulations, obtaining excellent optical selective properties of $\alpha = 0.94$ and $\varepsilon = 0.048$.

Gao et al. A tandem layer structured ZrC-ZrOx/Al2O3 coatings are deposited onto stainless steel (SS) substrates by the sputtering method for solar selective absorbing [2.80]. The ZrC-ZrOx and Al2O3 layers work as an absorptance layer and an antireflectance layer, respectively. The substrate temperature has an important effect on the optical properties of

the coating. With a high substrate temperature (300 °C), the SS/ZrC-ZrOx/Al2O3 coatings exhibit a relatively high absorptance of 0.92 and a relatively low emittance of 0.12.

2.3 ELECTROCHEMICAL METHODS

Electrochemical methods, including Electroplating and the Anodization, can be used to prepare various kinds of solar selective coatings .Electroplating refers to the process of moving metal irons in the solution by electric field to coat an electrode. The part to be plated is the cathode of the circuit. The solar selective coatings prepared by electroplating have good optical properties, such as black chrome, a complex graded $Cr–Cr_2O_3$ composite on an Al or Ni substrate. However, due to its high cost, risk of pollution and bad thermal stability in high temperatures, electroplating is only suitable for low temperature solar energy applications.

Similar to electroplating, anodization also employs an electrochemical reaction in a special electrolyte to produce a coating. When the metal substrate like aluminium is immersed in the phosphoric acid (H_2PO_4) solution and connected with the cathode of the circuit; the surface forms a porous oxide layer (Al_2O_3–based cermet) from an electrolytic reaction of the aluminium and oxygen generated from the electrolyte [2.81-2.82]. The oxide coating has two parts consisting of a compact barrier layer and a porous alumina layer whose pores are perpendicular to the aluminium. The anodized sample is then placed in metal salt solution for coloration, which amounts to electrochemical deposition of metallic rod-like particles like Ni, V, Cr, Co, Cu, Mo, Ag, and W; 30-50 nm in diameter and 300 nm long, inside the pores of the oxide layer. Table 2.3 shows the absorptance, emittance and thermal stability of various solar selective coatings deposited by electrochemical methods.

The solar selective coatings made by anodic oxidation are thermally stable so that they can work at high temperature, such as anodizing aluminium and steel coating [2.81-2.82]. Usually, their absorptance is above 0.9 and the emissivity is around 0.1. In a graded cermet, the reflectance from the cermet is reduced by gradually increasing the metal volume fraction; hence the refractive index, as a function of depth from the surface to the base of the film.

McDonald [2.83] prepared electroplated black chrome on a 2 ft x 4 ft collector tube sheet. The absorptance based on the air mass 2 spectrum (AM 2) and emittance based on the 121 °C blackbody spectrum are 0.868 and 0.088, respectively.

Material	Subst.	α	ε(100°C)	Stability (°C)	**Refs.**
Ni	Al alloy	0.995	-	-	Saxena [2.87]
Ni-Co	Al alloy	0.98	-	-	Shashikala [2.88]
Cr-Cr_2O_3	Al	0.8686	0.088 (121°C)	-	McDonald [2.83]
Cr-Cr_2O_3	Cu	0.93	0.12 (27°C)	300 in air	Lampert[2.84]
Cr- Cr_2O_3	Al	0.98	0.2 (27°C)	350 (134°C)	Ritchie [2.85]
Cr-Cr_2O_3	Ni	0.96	0.25-0.35	300 in air	Pettit [2.86]
Ni-Al_2O_3	Al	0.90	0.06	-	Kumar [2.91]
CoO	Ni plated SS	0.95	0.11	<300 in air & vacuum	Kruidhof [2.89]
$NiFeCrO_x$		0.9	~ 0.1	300 in air	Ding [2.90]
Ni- Al_2O_3	Al sheet	-	-	-	Tesfamichael [2.93]
Ni- Al_2O_3	Al	0.91	0.17	-	Kadirgan [2.94]
Co- Al_2O_3	Al sheet	0.92	0.16	515°C (12h) in vacuum	Cuevas[2.95]
Ni- Al_2O_3	Al	0.92-0.97	0.11-0.225	-	Wazwaz [2.96]
Ni-Al_2O_3	Al sheets	-	-	-	Zemanova[2.97]
Cu-$CuAl_2O_4$	Al	0.923	0.06	300°C (48h) in air	Ding [2.98]
Co-Al_2O_3	Al	0.92	0.28	-	Nahar [2.92]
Ni-Fe-Al_2O	Al	0.91	0.12	-	Santibanez [2.99]
MWCNT	-	-	-	-	Chen [2.100]
Ni	Cu	0.92	0.28	-	E-Gutierrez [2.101]
Black Ni	-	0.96	0.11	-	S. John [2.102]
Ni black	-	0.87-0.90	0. 09-0.12	<380 in air	Srinivasan [2.103]
Black Ni	-	-	-	-	Voinea & Duta [2.104]
CdS	ITO coated glass	0.95-0.97	0. 06-0. 08	-	Kadirgan [2.105]
Cu/CuO_x	Cu	0.9	<0.1	-	Bogatu [2.106]
Black Ni	Cu	-	-	-	Teixeira [2.107]
Cr- Cr_2O_3	Ni	~0.9	-	-	Jafari & Rozati [2.108]

Table 2.3: Solar selective coatings prepared by electrochemical methods

Lampert and Washburn investigated the chemical and microstructural stability of black chrome on copper substrate at different temperatures and atmospheres [2.84]. A microcrystalline Cr_2O_3 phase was found after annealing at over 400°C, and when the temperature increased to 500°C, a new phase Cr_3O_4 appeared. An appreciable degradation of the microstructure and optical performance was not observed when annealed up to 300°C; a mild degradation was found near 400°C. Major degradation appeared between 500°C and 600°C.

Thermal stability of black chrome coatings on aluminium substrates was further tested by by Ritchie et al. [2.85]. After long-term annealing (134 hours) at 350°C in air the absorptance and emittance values obtained were 0.98 and 0.2, respectively.

Pettit et al. carried out a series of experiments to further optimize the thermal stability of electrodeposited black chrome on Nickel substrates [2.86]. This was done by changing the bath composition (chromic acid, acetic acid, trivalent chromium and iron), substrate, plating current density, time, and temperature. The most stable coatings were achieved with lower concentrations of trivalent chromium and additional agents. The solar absorptance was found stable at 0.96 in air at 350°C.

V. Saxena conducted studies on ultra high solar absorber blackening of electroless nickel coatings on aluminum alloys for space application [2.87]. Process optimization was carried out by investigating the influence of various operating conditions, like pH of electroless nickel solution, thickness of electroless nickel deposit, concentration, temperature on the physico-optical properties of the black coating. The surface morphology of the coatings revealed a dense array of microscopic, conical pores perpendicular to the surface. This structure acts as light traps, was capable of absorbing over 99.5% light in solar region. The ultra high absorptance of the coatings was associated with unique surface morphology and formation of nickel oxides (NiO, Ni_2O_3).

Solar selective black nickel–cobalt were obtained on nickel plated aluminum alloys in an electrolyte system containing $CoSO_4.6H_2O$, $NiSO_4$ $7H_2O$, CH3COONH4, and NaSCN, 10 g/L were investigated by Shashikala et al. [2.88]. Process optimization was carried out by the hull cell experiments investigating the influence of operating variables on the optical selectivity of the coating. SEM studies showed that the particles in the coatings are of dentritic structure. The high degree of solar absorptance (0.98) is related to the irregular dentritic structure and surface roughness of the coatings. Polarization studies showed that the nickel cobalt coatings exhibit good corrosion resistance and their excellent environmental stability make them extremely suitable for ground as well as space applications.

Kruidhof researched on the use of cobalt oxide on bright nickel-electroplated steel as a spectrally selective material for use in solar collectors [2.89]. Cobalt was formed electrochemically in a high efficiency cobalt sulphate bath and oxidation was done in air for two hours at 400°C. Of all bath parameters the pH-value had the greatest influence on the optical properties of the oxide, the best results obtained at a pH of 2.3. At a temperature of 55°C and a current density of 400-800A/m^2 the ratio of the normal solar absorptance to the normal total emittance at 100°C , was found to be α/ε = 0.76/0.05 (pH = 4) and 0.95/0.11 (pH = 2.3). The high absorptance found at pH=2.3 is mainly due to the structure of the upper part of the surface which is needle-like without and rod-like with an iron(III) sulphate addition, the later coatings were stable in air and vacuum up to 300°C.

Ding et al. synthesized textured air stable $NiFeCrO_x$ selective absorber for mid-to-high temperature photothermal application by electrochemically treating a Fe–Cr–Ni alloy surface [2.90]. Optical performance achieved gave an absorptance exceeding 0.9 and emittance near 0.1, the special surface configuration was favorable for light selective absorption. It was

found that the effective absorbing materials were mainly oxidation-resistant Cr_2O_3 and $NiFe_2O_4$ spinel. The thermal stability of this film was tested by heat treatment at 300°C for 300 h in air Both the chemical composition and urchin-like surface structure showed excellent thermal stability at 300°C in air.

The effect of various anodization parameters on the structural features and optical properties of solar absorbing nickel pigmented anodic alumina coatings was studied by S. N. Kumar et al. [2.91] . After thoroughly washing with water, they were pigmented with nickel by carrying out ac electrolysis in a Watt's type of nickel electroplating bath using a thick sheet of nickel as counter electrode. Stable coatings with low thermal emittance, ε ~0.06 (at 100°C), and solar absorptance α >0.90 were obtained; these values could be varied over a wide range by controlling the anodizing parameters. Addition of H_2SO_4 in the anodizing bath lead to an increase in the α and ε values of the film due to the formation of a thicker and alumina rich anodic film.

Nahar et al. are one of the earliest authors to report on the development of Co-Al_2O_3 selective absorber for solar collectors [2.92]. Optical and microstructural properties of the $A1_2O_3$-Co spectrally selective surface were investigated. The anodic oxidation was carried out in a phosphoric acid bath followed by electrolytic coloration in a cobalt salt bath. The anodic $A1_2O_3$ coating obtained was porous, with wall thickness and void diameter of 51 nm and 30 nm respectively. The electrodeposited cobalt occupied the pores of the oxide and X-ray photoelectron spectroscopy studies show that cobalt was partially in metallic form. The maximal optical properties of the coating were $\alpha = 0.92$ and $\varepsilon = 0.28$, it was stable in air up to 400 °C both under IR heating as well as under high solar flux irradiation.

A Ni-Al_2O_3 absorber designed by anodizing was pyrolytically coated with SnO_2 to improve its coating quality, the overall goal was to obtain efficient absorbers by optimizing the optical properties as reported by Tesfamichael [2.93]. A better solar-absorptance of the Ni-Al_2O_3 at higher angles of incidence was found. This was due to enhanced optical interference in the double-layer structure of Ni-Al_2O_3, which could not be achieved in the graded index film of Ni-NiO_x.

The optical properties of Si-Al_2O_3 films of different thicknesses were investigated by preparing the films using an integral coloration method [2.93]. The solar-absorptance and thermal-emittance were found to increase with increasing film thickness. Due to high

thermal-emittance, the Si-Al_2O_3 coating showed non-selective absorbing properties, the results indicated that the Si-Al_2O_3 coating is not a suitable candidate for selective solar absorbers.

Kadirgan et al. [2.94] made an electrochemical characterisation of Al_2O_3 –Ni thin film selective surface on aluminium. The properties of the oxidised aluminium surfaces were investigated by cyclic voltammetry. Nickel pigmentation of porous aluminium surfaces was also performed as a function of electrochemical pigmentation conditions by ac electrodeposition. The data showed that increasing pH and temperature values result in decreasing oxide thickness. The emittance is increased with film thickness. An improvement in emittance was obtained for shorter nickel deposition times. The optical properties of the prepared surfaces were optimised, and a solar absorptance of 0.91 and a thermal emittance of 0.17 obtained.

Cobalt-alumina composite layer for solar thermal selective absorbers was electrochemically grown by Cuevas et al. [2.95]. Due to its potential use as selective surface in solar thermal absorbers, cobalt was electrodeposited into porous alumina obtained by anodization of aluminum sheet. A 3^2 factorial design was applied to find out the effects of the electrochemical variables, electrodeposition time and applied cell potential, on optical properties in specific the values that lead to high solar absorptance $\alpha = 0.92$ and low thermal emittance $\varepsilon = 0.16$ and to optimize the solar energy selectivity of the obtained surfaces.

Solar thermal performance of a nickel pigmented aluminium oxide selective absorber was done was determined by A. Wazwaz et. al using an experimental model (prototype model) [2.96] . The constructed models were tested outdoors during daylight under a clear sky and the flat-plate collector used was of the glazed type. The maximum calculated collective flux of the selective absorbers was in the range 590–699 W/m^2. The maximum conversion efficiency for the systems was in the range 0.73–0.78. The selective absorbers used have absorptivity in the range 92.0–97.0% while they have emissivity in the range 11.0–22.5%.

Nickel electrolytic colouring of anodic alumina for selective solar absorbing films was done by Zemanova et al. with the purpose of obtaining profound knowledge of the nickel precipitation mechanism [2.97] .The influence of the current waveform on nickel deposition and of the type of electrolyte on the quality of nickel-pigmented aluminium coatings was investigated. It was confirmed that the negative half wave of the time-dependent AC is

responsible for nickel deposition. Morphology study revealed that the positive half wave causes softening/dissolution of the structure deposit. The content of nickel in the anodic alumina layer was found to changes in dependence of applied current waveform and it reflects also the colour brightness and colour shade of the pigmented finishes [2.97].

A new selective solar absorber coating of Cu–$CuAl_2O_4$ hybrids deposited in anodic aluminium oxide (AAO) on aluminium substrate was prepared through an electrochemical process by Ding et al [2.98]. While optical performance mainly depended on the intrinsic absorption of Cu nanoparticles, $CuAl_2O_4$ played a role of protecting Cu from oxidation at high temperature. The as-synthesized sample showed an excellent selectivity (α/ε) of 0.923/0.06, which was consistent with the computer simulation [2.98]. While α decreased after annealing at 200°C in air for 24h, ε was slightly influenced; the absorber showed high selectivity (α/ε) of 0.87/0.04 and did not change even after exposure to 300°C for 48h. XRD analysis showed that crystalline structure of the hybrids did not change after annealing treatment; condensation caused a decrease of absorptance by cracking the surface, this was prevented by applying a protective layer on the surface.

Santibanez et al. reports on the electrochemical deposition of Ni-Fe alloys into porous alumina for solar selective absorbers [2.99]. Formation of Ni-Fe amorphous phases was detected for compositions as high as 73% of Fe. XPS measurements revealed the presence of superficial binary and ternary oxides such as NiO, Fe_2O_3, and $NiFe_2O_4$. It was demonstrated that the introduction of Fe into the Al/Al_2O_3/Ni cermets decreased the solar absorptance up to 5% while the emittance decreased up to 10% when the content of Fe is increased from 0% to 55%. The sample without Fe and 100% Ni had the highest solar absorptance (0.91) and sample 45 Ni% and 55% Fe had the lowest emittance (0.12). Ni-Fe nanorod sizes of ~270-275 nm significantly heighten the light trapping effects into the pores of alumina and presented the highest values of solar absorptance.

Chen et al. [2.100] reports accelerated ageing of a novel tandem carbon nanotube spectrally selective solar absorbers fabricated by facile and efficient electrophoretic deposition using a homogeneous multi-walled carbon nanotube (MWCNT) coating as absorbing layer. The primary results revealed that the MWCNT absorber had a great thermal stability but was not resistant to condensation since the porous MWCNT coating permits water migration through

the pores down to the Al substrate which as a result oxidizes and absorbs in the infrared. Therefore, different type soft thin films such as dense silica, silica-titania were deposited on top of MWCNT absorbers as protective layer to prevent the penetration of condensed water.

Estrella-Gutiérrez et al. investigated the influence of metallic nickel interlayer on the performance solar absorber coatings based on bright and black nickel electrodeposited onto copper from nickel sulfate and nickel chloride baths, respectively [2.101]. The black nickel selective coatings on copper were found to be unstable under the thermal treatment, resulting in partial peeling off of the black nickel film and overall deterioration of the optical properties. In the presence of the bright, metallic nickel interlayer, the selective coatings are stable upon heat treatment though solar-to- thermal conversion efficiency for these multilayer coatings is slightly lower than for coatings of black nickel directly electrodeposited onto copper; hence, the bright/black nickel selective coating with high solar absorptance $\alpha = 0.92$ and low thermal emittance $\varepsilon = 0.28$ is the preferred option for solar collector applications.

S. John reports on an electrodeposited black nickel solar absorber coating produced cathodically from a low concentration bath [2.102]. The variation in pH, concentration of the nickel and ammonium salts, electroplating time, and temperature gave rise to black or light and dark grayish coatings. Optical properties of the coating produced under the optimum conditions are found to be $\alpha = 0.96$ and $\varepsilon = 0.11$. Thermal cycling and corrosion tests indicate the durability and stability of the coating suitable for solar thermal energy conversion systems.

Nickel black selective solar absorber coatings were investigated by Srinivasan et al. for use in flat-plate solar collectors [2.103]. The coating was electroplated for 10s from an electrolyte containing nickel and ammonium chloride using a nickel anode and pH of 6.0. This coating was found to exhibit better corrosion resistance than the well-known black-nickel coatings (which contains nickel, zinc and sulphur) and had a thermal stability up to 380°C which is sufficient for application in flat-plate collectors. The optical values obtained were solar absorptance $\alpha = 0.87$-0.9 and low thermal emittance $\varepsilon = 0.09$-0.12.

Research on electrochemical deposition of black nickel solar absorber coatings on copper substrate for solar thermal applications was done by Voinea and Duta [2.104]. The process optimization based on the growth rate estimated on the potentiodynamic cathodic polarization curves and the effect of neutral electrolytes was discussed. From the cathodic curves it was

clearly observed that increasing the ionic strength at high NaCl concentrations, leads to one single deposition process which is bright nickel formation. Sodium chloride has the role of decreasing the electrolyte internal resistance and consequently increasing the growth rate.

Kadirgan conducted a study on the electrochemical nano-coating processes in solar energy systems [2.105]. The efficiencies of electrochemically prepared nano-thick CdS and black nickel coatings were investigated as a function of their preparation conditions. Electrodeposited CdS films were prepared in a classical double wall, three-electrode cell under nitrogen using a 0.2M $CdCl_2$ solution on indium tin oxide (ITO) coated glasses as the substrates. The optimized coatings were found to have a large absorptivity in the visible and near infrared range and have little emissivity in the infrared range with values $\alpha = 0.95\text{-}0.97$ and $\varepsilon = 0.06\text{-}0.08$.

Bogatu et al. report the electrodeposition of Cu/CuO_X solar selective coatings with controlled morphology [2.106]. The thin films are electrodeposited on copper substrate using precursor's solution based on copper and sodium acetate. Additive based on maleic anhydride copolymers with controlled water solubility were tested as tailoring morphology agents. Different morphologies were obtained depending on the polymer type and concentration. The stability of the polymer–copper ion structures and the electrical-induced conformational transitions of the polymers in the precursors' solution are studied by cyclic voltammetry and correlated with the nucleation and growth mechanisms of the thin films. The polymer addition in the precursor solution was found to significantly improve the optical properties of the Cu/CuO_x layers with overall values $\alpha > 0.9$ and $\varepsilon < 0.1$.

Teixeira et al. made an MFM and XPS analysis of black nickel solar absorber electrocoating on nanostructured copper, this coating is used in thermal solar collectors [2.107]. XPS (X-ray photoelectron spectroscopy) results identified black nickel as a Cermet mainly composed of two metallic nickel atoms for each nickel and zinc sulfide, i.e. 2 Ni: NiS: ZnS and traces of thiocyanate. MFM (magnetic force microscopy) validate that black nickel solar absorber coating is a nanometric graded cermet of NiS-ZnS with 13% of metallic nickel nanoparticles by chemical composition of XPS results and MFM.

Characterization of surface and optical properties black chrome films prepared by electroplating technique and deposited on bright nickel substrates are reported by Jafari and

Rozati [2.108]. SEM analysis shows that films were denser with nano size grains while others become porous, with micro sized grains. The XRD and EDS results show shows that structure of black chrome films from both baths mainly consist of metallic chrome with (110) orientation. The spectral reflectance in the UV-Vis-NIR and IR regions shows that black chrome films have good optical properties for solar energy absorption with solar absorptance $\alpha \sim 0.9$ and can therefore be used in solar collectors.

2.4 PAINTING AND OTHER METHODS

The painted coating consists of small particles (pigments) mixed with binders, which have good selective optical properties due to the high absorption of the pigment, well disseminated in the coating, and high reflection of the substrate in the infrared region. The painted coatings are usually painted, or sprayed, or dip-coated on the substrate to form solar selective absorbers. FeMnCuO4/silicon binder, PbS/polyacrylic resin are typical painted coatings. Even though the painting method is a simple, low cost process and suitable large-scale application, the painted coating usually has a high emittance and terrible bonding with the substrate.

Abendroth et al. conducted a study on the selective absorption of carbon nanotube(CNTs) thin films for solar thermal applications [2.109]. The CNT areal load can be used to achieve increased absorption and tune the absorption edge towards higher wavelength. For optimized coatings solar absorptance coefficients $\alpha>0.92$ and thermal emittance coefficients $\varepsilon<0.1$ (400 °C) were achieved. This high performance, high thermal stability of CNTs under atmospheric(up to 590 °C) and oxygen free conditions(up to 4000K), low cost process technologies and low material consumption cost savings could propel the integration of CNT coatings into absorber systems as an alternative to commercially available vacuum deposited cermet coatings for high temperature concentrated solar power (CSP) application.

B. Cheng et al. prepared and characterized porous carbon–titania nanocomposite films with a well-defined interconnected macropores structure via a polymer-assisted photopolymerization-induced phase-separation method with results that indicates an excellent solar selective absorber [2.110]. The non-ionic water-soluble polymer polyvinylpyrrolidone works as a sol modifier advantaging the mean size of the interconnected macropores, residual carbon content, and films thickness. The single layer of as-prepared porous C/TiO_2

nanocomposite films exhibits high solar absorptance (α = 0.928–0.959) with low thermal emittance (ε = 0.074–0.105) and photothermal conversion efficiency η = α-ε of 0.864 corresponding to a film thickness of around 338 nm.

Elisa Sani et al. reports on the production and optical characterization of highly dense, pure zirconium and tantalum diborides, for solar thermal absorbers [2.111]. Monolithic bulk samples are produced by Spark Plasma Sintering starting from elemental reactants or using metal diboride powders previously synthesized by Self-propagating High-temperature Synthesis (SHS). Microstructural and optical properties of products obtained by the two processing methods have been comparatively evaluated. We found that pure diborides show a good spectral selectivity, which is an appealing characteristic for solar absorber applications.

Zhang et al. designed a symmetric nanovoid resonator for silicon-based single-nanowire solar absorbers using extensive finite simulations [2.112]. Single semiconductor nanowires offer an attractive option for low-cost and high-efficiency with diverse applications in sensing, photo-detecting, and light-harvesting. The authors demonstrate that integrating a nanovoid resonator into the single nanowire dramatically enhances the absorption in a broad spectral band by exciting highly strengthened optical resonances in the nanovoid-deformed nanowire cavity. This consequently lead to a remarkable photocurrent density with an enhancement ratio of 37.5% compared to conventional solid NW design. The high absorption can be well preserved by either filling the nanovoid with low-index di-electric or introducing the dielectric substrate.

Avila et al. developed cobalt oxide films deposited on stainless steel substrates for solar selective surfaces by spray pyrolysis technique [2.113]. The predominant cobalt phase is Co_3O_4, CoO & Co_2O_3 phases were also detected. Films deposited upon nickeled steel substrates at 400°C exhibit high absorptance (0.86) and high emittance (0.43), yielding a selectivity of 2.0. A similar film on steel substrate reaches a figure of α = 0.77 and ε = 0.20, giving a selectivity of 3.85. In the case of SS substrates, appearance of an iron austenite phase points to an interaction between the SS substrate and the cobalt oxide film. It was found that the higher the annealing temperature the higher the roughness of the film, which is correlated to a noticeable decrease of carbon content.

Kotilainen et al. developed Hafnium oxide thin films as a barrier against copper diffusion in solar absorbers [2.114]. The ALD HfO_2 thin films were deposited in a thermal process at

200°C using Tetrakis(Dimethylamido)Hafnium (Hf(NMe2)4) and H_2O precursors, with 200, 400, and 600 cycles. The copper surface without a HfO_2 barrier thin film oxidized significantly, which increased thermal emittance and surface roughness. The thickest HfO_2 thin film studied, which was deposited from 600 ALD cycles and had a thickness ~50 nm, prevented Cu oxidation and diffusion processes after 2h heat treatment in air at 300°C, and retained low thermal emissivity. At 400°C, diffusion and formation of copper oxide hillocks were observed but the HfO_2 thin film significantly retarded the degradation when compared to a Cu substrate without and with thinner barrier layers.

Ollier et al. solar technologies require improved material performances or new materials functions, either to improve energy capture or to develop new conversion principles [2.115]. This work presents a low cost pathway to realize 2D nanophotonic molybdenum crystals having a transition in their optical properties with a tunable cut-off wavelength. These nanostructured materials have a dual function. They can be used as selective solar absorbers and/or selective infrared emitters. This novel pathway for producing low cost nanostructured materials creates new opportunities for solar capture in Concentrated Solar Power, Solar Thermophotovoltaics, Solar Thermo-Electrical Generators and for infrared emission control in thermophotovoltaic technologies

Ziabari et al. Cobalt alumina cermet thin films were deposited on stainless steel substrates and the re- lated solar selective absorption was studied [2.116]. The measured reflectance spectra of the cermet thin films were used to calculate the pertinent normal solar absorptance and normal thermal emittance. The sample with a Co/Al = 40/60 ratio showed the lowest thermal emittance. A multilayer structure (high and low Co/Al ratio layers and an antireflection coating of Al_2O_3 was prepared to inhibit optical degradation. The thermal stability of the solar selective absorbing coating was tested by annealing at high temperature in air.

2.5 SOLUTION-BASED METHOD

The solution-based method is a chemical method widely used in the solar selective coating preparation of nanomaterials and ceramics. Compared with other techniques, such as evaporation, CVD, and sputtering the simplicity and low cost of solution-based processing allow it to be a possible candidate for large-scale deposition of spectrally selective coatings. In the process of sol-gel, the colloidal solution is obtained from some metal alkoxides and metal salts by various forms of hydrolysis and polycondensation reactions. This is then deposited to form a coating. The coatings fabricated by sol-gel process are uniform but easily damaged. Table 2.4 shows the absorptance, emittance and thermal stability of various solar selective coatings deposited by solution-based methods.

Material	Subst.	α	ε(100°C)	Stability (°C)	**Refs.**
$CuFeMnO_4$	Al plate	0.85	0.07	-	Kaluza[2.117-2.118]
Au-SiO_2	Metal or glass	0.80	0.01 (400°C)	>500	Lincoln
Ni-Al_2O_3	Al	0.83	0.03	-	Bostrom[2.119]
Ni- Al_2O_3 with Al_2O_3 ARC	Al	0.93	0.03	-	Bostrom[2.119]
Ni-Al_2O_3	Al	0.93	0.05	300 in air	Z. Li [2.120]
Ni-Al_2O_3	-	>0.90	<0.1 (100°C)	-	Wang [2.121]
Cr/α-Cr_2O_3	Cu	>0.95	-	<600 (2h) in air	Khamlich [2.123]
Porphyrin nanorods	-	>0.98	-	-	Mongwaketsi [2.125]
nc-C/TiO_2	-	0.939	0.195	-	Wang [2.126]
Cu-Co-Mn-Si-O	-	0.95	0.12(100°C)	360 in air	Joly [2.127]
ZnO	Al	0.71	0. 06	-	Katumba [2.128]
NiO	Al	0.84	0. 04	- -	,,

Table 2.4: Solar selective coatings prepared by solution based method.

Kaluza and Orel et al. conducted a study on the structural and optical properties of Sol-gel processed $CuFeMnO_4$/Spinel and $CuFeMnO_4$/silica Films and $CuCoMnO_x$/Spinel Coatings for Solar Absorbers [2.117-2.118]. Their study showed that the $CuFeMnO_4$ coated on the Al plate by sol-gel process has the absorption of 0.85 and emissivity of 0.07.

Cermets made with TiO_2 and ZrO_2 plus additives of noble metals such as Au and Pd have been found to be solar selective because of their high index of refraction and significant chemical and mechanical stability. According to Blickensderfer et al. selective absorber cermets (33%Au/67%TiO_2) made by inexpensive sol-gel techniques have good optical selectivity α/ε (400°C) = 0.80/0.01 and thermal durability (>500°C in air) [2.57]. An AR layer increases absorptance up to 0.85. Thermal durability has been tested in an oven at temperatures above 500°C at ambient conditions with no degradation in performance.

Titanium, zirconium, or hafnium metal carbides, oxides, and nitrides have a high degree of spectral selectivity. In these group IV tandem absorber-reflector films, of the compositions studied, substoichiometric compounds of TiN_x, ZrN_x, and ZrC_xN_y (on silver) had the best combination of high solar absorptance and low thermal emittance [2.57]. TiN_x and ZrN_x had nearly identical optical properties, but for HfN_x the absorptance was lower and the emittance higher. ZrC was the best pure carbide film. Adding carbon to form zirconium carbonitride (ZrC_xN_y) increased the solar absorptance by 6%.

Tobias Bostrom developed and optimized highly selective and durable Ni–Al_2O_3 cermet-based coatings on aluminum substrates using the solution-based method [2.119]. The optimal coating, with a nickel content of 65%, a thickness of 0.1 μm, and a particle size of ~ 10 nm, has a normal solar absorptance of 0.83 and a normal thermal emittance of 0.03 at 100°C.

To further optimize the spectral selectivity, Bostrom et al. [2.119] applied an anti-reflection layer silica, hybrid silica, silica-titania' or alumina to the Ni–Al_2O_3 using a sol–gel process. The optimized sample was achieved when alumina was used as an AR coating; the absorber had a solar absorptance of 0.93 and a thermal emittance of 0.03 at 100°C. The structure and morphology investigation revealed the size of the Ni nanoparticles dispersed in Al_2O_3 was in the range of 3–10 nm.

Ni–Al_2O_3 coatings prepared via an aqueous solution-chemical method was suggested by Li et al. [2.120], the aqueous solution had many advantages, such as its abundance, lower cost, and low toxicity. They found that a single Ni–Al_2O_3 coating on an aluminium substrate demonstrated a high normal solar absorptance of 0.85 and a low thermal emittance of 0.03 at 100°C. A three-layer coating consisting of a double absorption layer and one antireflection layer indicated a better selectivity with a solar absorptance of 0.93 and a thermal emittance of 0.05 at 100°C and thermal stability in air up to 300 °C.

Wang et al. observed that surface plasmon polaritons enhanced solar absorption in a Ni nanochain-Al_2O_3 cermet structure, which demonstrated a high solar absorptance exceeding 0.90 and a low thermal emittance of less than 0.1 [2.121]. The authors also discovered that the spectral selectivity can be tailored by changing the length of Ni nanochains.

Ni–Al_2O_3 solar selective absorbing coatings were prepared by Zhenxiang Li et al. using the simple and easy to perform aqueous solution-chemical method (sol gel) [2.122]. At high temperature and in N_2 atmosphere, aluminium ions from an Aluminium and nickel nitrate solution were converted into an Al_2O_3 matrix and nickel ions were in situ reduced into nano-size nickel particles embedded in the Al_2O_3 matrix. The three-layer coating exhibited better optical properties of selectivity (α/ε) = 0.93/0.05 respectively, and is stable in air up to 300°C. Due to excellent properties and low cost, the Ni–Al_2O_3 coatings fabricated by aqueous solution-chemical method were strongly competitive with those prepared by sputtering method.

S. Khamlich [2.123] developed black Cr/α-Cr_2O_3 nanoparticles based solar absorbers. Monodisperse spherical core–shell particles of with high adhesion were successfully coated on rough copper substrates by a simple self-assembly-like method with high adhesion to the substrate: the Aqueous Chemical Growth (ACG). The samples aged for more than 40h at 75°C show high chromium percentage on the surface of the particles, low infrared reflectance exhibit the targeted high absorbing optical characteristic -Black chrome while those aged for show a significant high UV–vis diffuse reflectance -green color''.

S. Khamlich et al. investigated the effect of 2h annealing on the structural and optical properties of cCr/α-Cr_2O_3 monodispersed particles based solar absorbers [2.124]. Designed using green chemical method, the so-called aqueous chemical growth (ACG).The XRD and ATR analysis indicated that by increasing annealing temperature, the particles crystallinity was improved and Ta_2O_5 was formed around 600°C, due to the fast oxygen diffusion from the deposited _-Cr_2O_3 toward the tantalum substrate. The optical measurements show that samples annealed at 400 and 500°C exhibit the targeted high absorbing optical characteristics of "Black chrome", while those annealed below 400°C and above 500°C show a significant low absorptivity and high emissivity.

Mongwaketsi et al. synthesized and characterized porphyrin nanorods for solar radiation harvesting and solar cells [2.125]. Spectroscopic and microscopic studies were carried out to investigate the effect that time, concentration and solvents have on the fabrication of porphyrin nanorods by ionic self-assembly by aggregation of two oppositely charged porphyrins $[H_4TPPS_4]^{2-}$ and $[SnTPyP]^{2+}$. The porphyrin nanostructures reflectance for all samples was found to be below 0.2%. The study demonstrates the potential for using different

concentrations and solvents to influence the physical and optical properties of porphyrin based nanorods.

Wang et al. fabricated a composite selective solar absorber containing uniform nano-crystallized carbon (nc-C) embedded in titanium oxide (TiO_2) matrix by a facile sol–gel technique [2.126]. The high-resolution TEM demonstrated that the nc-C grains, whose size ranges from 2 nm to 10 nm, make up a crosslinked network. The structural template (polyethylene glycol) used could tune the carbon contents of the composite films and the optimized α and ε optical values of the single layer film on copper substrate were about 0.939 and 0.195, respectively. The little deterioration after aging test (at 500 °C for 30h in vacuum) demonstrated an outstanding durability of nc-C/TiO_2 nano-composite films.

Joly et al. conducted a study on high temperature multi-layered chrome-free novel black selective coating for tubular solar absorbers based on a low-cost sol gel method [2.127]. The multi-layered Cu–Co–Mn–Si–O based nanocrystalline thin films thin films were designed with the aid of computer simulations based on the method of characteristic matrices and deposited using a sol–gel dip-coating. After optimization of the multilayer design, optical values $\alpha = 0.95$ and $\varepsilon = 0.12$ at 100°C have been achieved. The stability of the coatings at 360°C in air surpassed the one of the conventional robust black chrome coatings existing on the market and found to be candidate for applications working with CSP.

Katumba et al. report selective solar absorber coatings of carbon embedded in ZnO and NiO matrices on aluminium substrates have been fabricated by a sol–gel technique [2.128]. The SEM and other techniques revealed a smooth featureless surface for both C–ZnO and C–NiO ,dentritic features for some C–NiO samples and a nanometric grain size for both types of samples. The C–ZnO and C–NiO coatings contained amorphous carbon embedded in nanocrystalline ZnO and NiO matrices, respectively. Based on the results, C–NiO samples proved to have better solar selectivity behaviour than the C–ZnO counterparts. The optical values obtained were $\varepsilon = 0.06$ for the ZnO and $\varepsilon = 0.04$ for the NiO matrix materials; $\alpha = 0.71$ and $\alpha = 0.84$ for ZnO and NiO samples, respectively.

Boström et al. investigated Nickel-alumina/silica thin film materials for the use in solar thermal absorbers [2.129]. The TEM images revealed that all layers have a very small thickness variation and that the layers are completely homogenous. High resolution images

showed 5–10 nm (poly) crystalline nickel nanoparticles. ERDA showed that both the silica and alumina compositions contain more oxygen than 2:1 and 3:2 respectively. SEM showed the surface morphology and characteristics of the top silica anti-reflection layer. Hybrid-silica has showed to generate a smoother surface with less cracking compared to pure silica. The final curing temperature revealed to be of importance for the formation of cracks and the surface morphology.

2.6 COMMERCIALLY AVAILABLE SOLAR SELECTIVE COATINGS

A large number of mid-temperature physical vapor deposited solar selective coatings have been developed, but only few of them have been successfully commercialized. SS–C, SS–AlN, CrN–Cr_2O_3, etaplus, TiNOX, a-C:H/Cr, TiC/TiOxNy/AlN and Ni–NiO coatings are commercially marketed by NittoKohki,Turbosun, Alanod Solar, BlueTec, Almeco-TiNOX, Ikarus Coatings, Plasma and S-Solar, respectively.

Solar selective coatings such as Pt–Al_2O_3, Ni–Al_2O_3, Ni–SiO_2, Fe–Al_2O_3, Cr–SiO, Mo–Al_2O_3, Mo–SiO_2, W–Al_2O_3, etc. have been developed for high-temperature solar thermal applications, as extensively discussed in section 2.5. However only a few of them such as, Mo–SiO_2, W–Al_2O_3, Mo–Al_2O_3 and M–AlN (M:SS,W and Mo) cermets have been successfully commercialized and are being used in evacuated receiver tubes for solar thermal power generation. Table 2.5 also shows the list of commercially available sputter deposited solar selective coatings, for mid and high temperature applications all of these have a graded composite absorber.

TurboSun, China in conjunction with Peking University, China and the University of Sydney, Australia have commercially developed evacuated solar collector tubes incorporating sputtered SS–AlN cermet solar selective coatings [2.130]. Currently, TurboSun manufactures three different series of solar collector tubes with superior solar performance also designs, manufactures and installs utility-scale solar hot water systems. TurboSun also produces commercial U-shaped all-glass evacuated solar collector tubes that are widely used for low temperature solar hot water collectors. According to the IEA Report, China is leading the solar water collector market (87.5 GW installations) and the dominant collector type is the evacuated tube collector, which represents 54.2% of the global market followed by the flat-plate collector with a market share of 32.6% [2.131].

Company	Coating	α	ε(100°C)	Stability (°C)
Siemens Germany	Al_2O_3 based cermet	0.96	0.1 (400°C)	400°C
Formely Solel Solar Systems Ltd	Mo-Al_2O_3	0.96	0.16 (350°C)	350-500°C in vacuum
	W-Al_2O_3	0.96	0.16 (350°C)	350-500°C in vacuum
Angelantoni-ENEA, Italy	Mo-SiO_2	0.94	0.13 (580°C)	580°C in vacuum
	W/W-Al_2O_3/ Al_2O_3	0.93	0.10 (400°C) 0.14 (550°C)	
SCHOTT, Germany	-	0.95	0.10 (400°C)	500°C in vacuum
Nitto Kohki, Japan	SS-C	0.93	0.04 (100°C)	300°C in vacuum
Alanod Solar, Germany	Sunselect (Cu) ($CrN–Cr_xO_y$)	0.95	0.05 (100°C)	-
	Mirotherms (Al)	0.95	0.05	-
	Mirosols (Al)	0.90	0.15	-
IKARUS Coating, Germany	a-C:H/Cr	0.92	0.08-0.09 (100°C)	250°C in air
S-Solar (Sunstrip), Sweden	Ni-NiO	0.96	0.10 (100°C)	300°C in air
PLASMA, Macedonia	TiC-/TiO_xN_y/AlN	0.95	<0.10 (100°C)	350°C in air
TurboSun, China	W-AlN	0.92-0.94	0.08-0.10 (350°C)	350-500°C in vacuum
	SS-AlN	0.94-0.95	0.12-0.14 (350°C)	
Schott(Spezialgas), Germany	Aluxid	0.95	0.05	280°C
Almenco-TiNOX, Germany	TiNOX energy Al	0.95	0.04 (100°C)	-
	TiNOX energy Cu	0.90-0.95	0.04-0.05 (100°C)	-
BlueTec, Germany	Eta Plus (cermet coating)	0.95	0.05 (100°C)	295°C

Table 2.5 List of commercially available mid and high temperature solar selective coatings

An Italian-German company called Almeco-TiNOX produces TiNOX energy, a commercial TiNxOy cermet on copper substrate [2.132] [2.5].Their products are TiNOX energy Al, TiNOX energy Cu and TiNOX artline. The coating has passed the International Energy Agency Task X Service Lifetime and Performance Criterion Tests. TiNOX energy Cu and TiNOX artline have an absorptance of 0.90-0.95 and emittance of 0.04-0.05 at 100°C.

The Center for PlasmaTechnologies-PLASMA developed and produced spectrally selective coatings based on titanium composites i.e.,TiC/TiO_xN_y/AlN for solar hot water collectors [2.133]. The coatings exhibited high thermal stability (450 °C), corrosion stability and good optical properties see Table 2.1.

BlueTec Germany used sputtering method to develop a new generation absorber (etaplus) for solar hot water applications [2.134]. The coating performance was evaluated by Fraunhofer Institute for Solar Energy Systems, ISE, Freiburg, Germany and found suitable for collector stagnation temperatures up to 295°C [134].

CrN/Cr_2O_3 mid–temperature solar selective coating developed using experimental design methods is commercially produced by Alanod Solar, Germany and the product name is Sunselect [2.135] [2.136] . The graded cermet based on chromium oxynitride with absorptance greater than 0.93 and emittance of 0.07 at 100°C was deposited on Cu substrates by DC magnetron sputtering technique. The results also showed that the graded CrN/Cr_2O_3 is durable enough for an application in ventilated flat plate collectors for domestic hot water system with a service lifetime of more than 25years [2.135].

Ni–NiO graded index coatings on aluminium substrates are commercially produced by S-Solar, Sweden [2.137] [2.138]. The coating consists of three layers: a nickel barrier layer, a selectively absorbing Ni–NiO layer and an antireflection coating and has passed stability tests conducted in accordance with the requirements of the International Energy Agency,Task X. The tests included checking the durability of the surface against condensation, sulphur oxide and high temperatures. Sunstrip's test results were approved and the values correspond to a product lifespan of over 25years [2.139].

Schuler et al. developed transition metal containing amorphous hydrogenated carbon films (a-C:H/TM, TM = Ti, Cr) or transition metal containing silicon–carbon films (a-Si:C:H/TM) by combined PVD and PECVD process [2.140-2.141]. These coatings can be fabricated by sequential deposition of pure transition metal (Ti, Cr), a-C:H/TM and pure a-C:H. Accelerated aging tests indicated that the service life time of the a-C:H/Ti coatings was more than 25 years. The a-C:H/Cr coating has been reported to pass the accelerated aging tests and are commercially produced by IKARUS Coatings, Germany [2.142].

Luz International Ltd., USA has produced receiver tubes that use $Mo–Al_2O_3$ cermet coatings due to their excellent thermal stability in vacuum, however their thermal stability in air is low (<300°C) [2.143]. The $Mo–Al_2O_3$ cermet coatings were deposited using planar magnetron sputtering technology and are used in Solar Energy Generating Systems power plants.

Siemens, Germany (formerly Solel) have modified the $Mo–Al_2O_3$ cermet coating, their Universal Vacuum Air Collector (UVAC2008) receiver tube uses a novel Al_2O_3 based multilayer cermet, which exhibit higher thermal stability and has an absorptance of 0.97–0.98 and emittance of 0.07–0.10 at 400°C [2.144].

Solar Energy (ASE), Italy and Schott, Germany began produces receiver tubes (HEMS08) for CSP Technologies, where the thermal exchange fluid is a molten salt entering at 290°C in the solar field and coming out at 550°C [2.145]. Therefore, the receiver tube and the solar selective coating have to be stable up to 580°C. The HEMS08 receiver tubes are coated with selective coatings of Mo–SiO_2 (or) W–Al_2O_3 [146] [167] and these are thermally stable at 580°C in vacuum. They have also developed graded TiN–AlN cermet with AlN or Al_2O_3 antireflection coating exhibiting absorptance of 0.95 and emittance of 0.12 at 580°C [2.147].

A large number of mid- and high temperature solar selective coatings have been developed by PVD methods such as evaporation, ion plating, pulsed laser deposition, cathodic arc evaporation and sputtering since 1970's. Amongst these magnetron sputtering method has been widely used for large area deposition of solar selective coatings.

In this thesis, we have designed femtosecond laser surface structured ferromagnetic nanorods in Al_2O_3 matrix selective solar absorbers using electrochemical methods anodization and electrodeposition. This Co and Ni nanorods in Al_2O_3-based cermet have been among the first class of selective solar absorbers if one considers results as reported in this literature survey dating from late 1980, the additional femtosecond laser surface nanostructuring enhances further their optical selectivity as shown for the first time in this research, this later aspect represents the originality of this contribution.

2.7. REFERENCES

[2.1] C.Donald, P. O'Neill, A. Ignatiev, Particulate nature of solar absorbing films: Gold black. Journal of Vacuum Science and Technology 14 (1977) 259–262.

[2.2] K. Kimoto, Y. Kamiya, M. Nonoyama, R. Uyeda, An electron microscope study on fine metal particles prepared by evaporation in argon gas at low pressure. Japanese Journal of Applied Physics 2 (1963) 702–713.

[2.3] L. Harris and E.R. Washwell, Optical and electrical properties of bismuth deposits doped with tellurium. Journal of the Optical Society of America 62 (1972)1162–1164.

[2.4] L. Harris, R.T. McGinnies, B.M. Siegel, The preparation and optical properties of goldblacks. Journal of the Optical Society of America 38 (1948) 582–588.

[2.5] N. Selvakumar, H.C. Barshilia, Review of physical vapor deposited(PVD) spectrally selective coatings for mid- and high-temperature solar thermal applications. Solar Energy Materials & Solar Cells 98 (2012) 1–23.

[2.6] G. Hass, H.H. Schroeder, H.F. Turner, Mirror coatings for low visible and high infrared reflectance. Journal of the Optical Society of America 46 (1956) 31–35.

[2.7] G.A Niklasson, C.G. Granqvist, Optical properties and solar selectivity of co-evaporated Co-Al_2O_3 composite films. J. Appl. Phys. 55 (1984) 3382-3410.

[2.8] D.M. Mattox, G.J. Kominiak, Deposition of semiconductor films with high solar absorptivity. Journal of Vacuum Science and Technology 12 (1975) 182–185.

[2.9] T.J. McMahon, S.N. Jasperson, PbS-Al selective solar absorbers. Applied Optics 13 (1974) 2750–2751.

[2.10] R. Marchini, R. Gandy, Selective absorption properties of lead sulfide-aluminum coatings as a function of lead sulfide thickness. Journal of Applied Physics 49 (1978) 390–391.

[2.11] L.E. Flordal, R. Kivaisi, Vacuum evaporated thin films for solar collectors. Vacuum 27 (1977) 399–402.

[2.12] P.J. Martin, R.P. Netterfield, W.G. Sainty, Spectrally selective PbS films produced by ion beam sputtering.Thin Solid Films 87 (1982) 203–206.

[2.13] W. Brunger, Vacuum 30 (1980) 125–127.

[2.14] G.L. Harding, Evaporated chromium black selective solar absorbers. Thin Solid Films 38 (1976) 109–115.

[2.15] C.G. Granqvist, G.A. Niklasson, Ultrafine chromium particles for photothermal conversion of solar energy. Journal of Applied Physics 49 (1978) 3512–3520.

[2.16] R.T. Kivaisi, Optical properties of selectively absorbing chromium films deposited at oblique angle of incidence. Solar Energy Materials 5 (1981) 115–127.

[2.17] F.H. Cocks, M.J. Peterson, Tellurium and selenium selective absorber thin films produced by gas-evaporation methods. Journal of Vacuum Science and Technology 16 (1979) 1560–1563.

[2.18] Y. Yin, D.R. McKenzie, W.D. McFall, Cathodic arc deposition of solar thermal selective surfaces. Solar Energy Materials and Solar Cells 44 (1996) 69–78.

[2.19] H. Randhawa, Cathodic arc plasma deposition technology. Thin Solid Films167 (1988) 175–186.

[2.20] F. Jahan, G.B. Smith, Investigation of angular selective optical properties of silver/titanium oxide cermet thin films.Thin Solid Films 333 (1998) 185–190.

[2.21] A. Marquez, G. Blanco, M.E.F. deRapp, D.G. Lamas, R. Tarulla, Properties of cupric oxide coatings prepared by cathodic arc deposition. Surface and Coatings Technology 187 (2004) 154–160.

[2.22] F. Garnich, E. Sailer, Cu–SiO_2/Cu–cermet selective absorbers for solar photothermal conversion. Solar Energy Materials 20 (1990) 81–89.

[2.23] D.R. McKenzie, Effect of substrate on graphite and other solar selective surfaces. Applied Optics 17 (1978) 1884–1888.

[2.24] Q.C. Zhang, D.R. Mills, New Cermet Film Structures with Much Improved Selectivity for Solar Thermal Application. Appl. Phys. Lett. 60(5) (1992) 545-547.

[2.25] Q.-C. Zhang, D.R. Mills, High solar performance selective surface using bi-sublayer cermet film structures. Solar Energy Materials and Solar Cells 27 (1992) 273–290.

[2.26] M. Okuyama, K. Furusawa, Y. Hamakawa, Ni cermet selective absorbers for solar photothermal conversion. Solar Energy 22 (1979) 479–482.

[2.27] D.R. McKenzie, Gold, silver, chromium and copper cermet selective surfaces for evacuated solar collectors. Applied Physics Letters 34 (1979) 25–28.

[2.28] R.N. Schmidt, K.C. Park, High-temperature space-stable selective solar absorber coatings. Applied Optics 8 (1965) 917–925.

[2.29] R.E. Peterson, J.W. Ramsey, Thin film coatings in solar-thermal power systems. Journal of Vacuum Science and Technology 12 (1975) 174–181.

[2.30] C.E. Kennedy, Review of Mid- to High-Temperature Solar Selective Absorber Materials, NREL/TP-520-31267, National Renewable Energy Laboratory,Colorado, July 2002.

[2.31] Z.Y. Nuru, C.J. Arendse, T.F.G. Muller and M. Maaza, Structural and optical properties of $Al_xO_y/Pt/Al_xO_y$ multilayer absorber. Maters. Scie. & Eng. B 117 (2012) 1194-1199.

[2.32] H.G Craighead, R. Bartynski, R.A. Buhrman, L.Wojcik, A.J. Sievers, Metal/insulator composite selective absorbers. Solar Energy Materials 1 (1979) 105–124.

[2.33] H.G. Craighead, R.E. Howard, J.E Sweeney, R.A. Buhrman, Graded-index Pt–Al_2O_3 composite solar absorbers. Applied Physics Letters 39 (1981) 29–31.

[2.34] L. Rebouta, A. Sousa, P. Capela, M. Andritschky, P. Santilli, A. Matilainen, K. Pischow N.P. Barradas, E. Alves, Solar selective absorbers based on Al_2O_3:W cermets and AlSiN/AlSiON layers. Solar Energy Materials & Solar Cell 137 (2015) 93-100.

[2.35] J. Tua, J.H. Gao, S. Hui, D. Lou, H.L. Zhang, L.Y. Liang, A.P. Jinc, Y.S. Zou, H.T. Cao, Alloyed nanoparticle-embedded alumina nanocermet film: A newattempt to improve the thermotolerance. Applied Surface Science 331 (2015) 285–291.

[2.36] A. Antonaia, A.Castaldo, M.L. Addonizio, S.Esposito, Stability of W-Al_2O_3 cermet based solar coating for receiver tube operating at high temperature. Solar Energy Materials & Solar Cells 94 (2010) 1604–1611.

[2.37] M. Kotilainen, K.Mizohata, M.Honkanen, P. Vuoristo, The temperature-induced ageing of solar thermal absorbers of plain and anodized aluminium substrates. Solar Energy Materials and Solar Cells 134 (2015) 244–251.

[2.38] J.A. Thornton, J.L. Lamb, Sputter deposited Pt–Al_2O_3 graded cermet selective absorber coatings. Solar Energy Materials 9 (1984) 415–431.

[2.39] J.A. Thornton, J.L. Lamb, Sputter deposited Pt–Al_2O_3 selective absorber coatings. Thin Solid Films 83 (1981) 377–385.

[2.40] J.A. Thornton, J.L. Lamb, Sputter-deposited $Al_2O_3/Mo/Al_2O_3$ selective absorber coatings. Thin Solid Films 72 (1980) 101-110.

[2.41] J.A. Thornton, J.L. Lamb, Thermal stability studies of sputter-deposited multilayer selective absorber coatings. Thin Solid Films 96 (1982) 175–183.

[2.42] M. Mast, K. Gindele, M. Kohl, Ni/MgF_2 cermet films as selective solar absorbers. Thin Solid Films126 (1985) 37–42.

[2.43] T.K. Vien, C. Sella, J. Lafait, S. Berthier, Pt-Al_2O_3 selective cermet coatings on superalloy substrates for photothermal conversion up to 600°C. Thin Solid Films 126 (1985) 17-22.

[2.44] T.S. Sathiaraj, R.Thangaraj, A. Sharbaty, M. Bhatnagar, O.P. Agnihotri, Ni–Al_2O_3 selective cermet coatings for photothermal conversion up to 500°C. Thin Solid Films190 (1990) 241–254.

[2.45] J.C.C. Fan, P.M.Zavracky, Selective black absorbers using MgO/Au cermet films. Applied Physics Letters 29 (1976) 478–480.

[2.46] J.C.C. Fan, S.A. Spura, Selective black absorbers using rf-sputtered Cr_2O_3/Cr cermet films. Applied Physics Letters 30 (1977) 511–513.

[2.47] H.C. Barshilia, N.Selvakumar, K.S. Rajam, A. Biswas, Structure and optical properties of pulsed sputter deposited Cr_xO_y/Cr/Cr_2O_3 solar selective coatings. Journal of Applied Physics103 (2008) 023507:1–023507:11.

[2.48] Y. Yin, Y. Pan, L.X. Hang, D.R. McKenzie, M.M.M. Bilek, Direct current reactive sputtering Cr–Cr_2O_3 cermet solar selective surfaces for solar hot water applications.Thin Solid Films 517 (2009) 1601–1606.

[2.49] R. Pettit, R.R. Sowell, I.J. Hall, Black chrome solar selective coatings optimized for high temperature applications. Solar Energy Materials 7 (1982) 153–170.

[2.50] R.B. Pettit, Accelerated temperature aging of black chrome solar selective coatings. Solar Energy Materials 8 (1983) 349–361.

[2.51] D.R. McKenzie, Production of solar absorbing cermet films by dual cathode DC magnetron sputtering.Thin Solid Films 62 (1979) 317–325.

[2.52] H.C. Barshilia, P.Kumar, K.S. Rajam, A. Biswas, Structure and optical properties of Ag–Al_2O_3 nanocermet solar selective coatings prepared using unbalanced magnetron sputtering. Solar Energy Materials and Solar Cells 95 (2011) 1707–1715.

[2.53] G.L. Harding, Sputtered metal carbide solar-selective absorbing surfaces. Journal of Vacuum Science and Technology 13 (1976)1070–1072.

[2.54] G.L. Harding, Sputtered metal silicide solar selective absorbing surfaces. Journal of Vacuum Science and Technology 15 (1978) 65–69.

[2.55] G.L. Harding, B. Window, Graded metal carbide solar selective surfaces coated on to glass tubes by a magnetron sputtering system. Journal of Vacuum Science and Technology 16 (1979) 2101–2104.28Deut12.

[2.56] C. Wyon, J. Valignat, Elaboration and characterization of a sputtered copper-stainless steel-amorphous carbon solar selective surface for use in evacu-ated collectors. Solar Energy Materials 11 (1985) 435–446.

[2.57] R. Blickensderfer, D.K. Deardorff, R.L. Lincoln, Spectral reflectance of TiN_x and ZrN_x films as selective absorbers. Solar Energy 19 (1977) 429–432.

[2.58] H.C. Barshilia, N. Selvakumar, K.S. Rajam, D.V.S. Rao, K. Muraleedharan, A. Biswas, TiAlN/TiAlON/Si_3N_4 tandem absorber for high temperature solar selective applications. Applied Physics Letters 89 (2006) 191909:1–191909:3.

[2.59] H.C. Barshilia, N. Selvakumar, K.S. Rajam, D.V.S. Rao, K. Muraleedharan, Deposition and characterization of TiAlN/TiAlON/Si_3N_4 tandem absorbers prepared using reactive direct current magnetron sputtering. Thin Solid Films 516 (2008) 6071–6078.

[2.60] H.C. Barshilia, N. Selvakumar, K.S. Rajam, Thermal stability of TiAlN/TiAlON/Si_3N_4 tandem absorbers prepared by reactive direct current magnetron sputtering. Journal of Vacuum Science and Technology A 25 (2007) 383–390.

[2.61] H.C. Barshilia, V.K. William Grips, K.S. Rajam, Solar Selective Coating Having Higher Thermal Stability Useful for Harnessing Solar Energy and a Process for the Preparation Thereof. (2009) US Patent No. 7585568 B2.

[2.62] H.C. Barshilia, N. Selvakumar, K.S. Rajam, A. Biswas, Optical properties and thermal stability of TiAlN/AlON tandem absorber prepared by reactive DC/RF magnetron sputtering. Solar Energy Materials and Solar Cells 92 (2008) 1425–1433.

[2.63] H.C. Barshilia, N. Selvakumar K.S. Rajam A. Biswas,Spectrally selective NbAlN/NbAlON/Si_3N_4 tandem absorber for high-temperature solar applications. Solar Energy Materials and Solar Cells 92 (2008) 495–504.

[2.64] H.C. Barshilia, N. Selvakumar, G. Vignesh, K.S. Rajam, A. Biswas, Optical properties and thermal stability of pulsed sputter deposited $Al_xO_y/Al/Al_2O_3$ multilayer absorber coatings. Solar Energy Materials and Solar Cells 93 (2009) 315–323.

[2.65] T. Eisenhammer, Quasicrystal films: numerical optimization as a solar selective absorber. Thin Solid Films 1 (1995) 270.

[2.66] A. Haugeneder, T. Eisenhammer, A. Mahr, J. Schneider, M. Wendel, Oxidation of quasicrystalline and crystalline AlCuFe thin films in air. Thin Solid Films 307 (1997)120–125.

[2.67] T. Eisenhammer, A.Haugeneder, A. Mahr, High-temperature optical properties and stability of selective absorbers based on quasicrystalline AlCuFe. Solar Energy Materials and Solar Cells 54 (1998) 379–386.

[2.68] N.Selvakumar, H.C.Barshilia, K.S.Rajam, A.Biswas, Structure,optical properties and thermal stability of pulsed sputter deposited high temperature $HfO_x/Mo/HfO_2$ solar selective absorbers. Solar Energy Materials and Solar Cells 94 (2010) 1412–1420.

[2.69] S.Yue, S.Yueyan, W.Fengchun, High-temperature optical properties and stability of Al_xO_y–AlN_x–Al solar selective absorbing surface prepared by DC magnetron reactive sputtering. Solar Energy Materials and Solar Cells 77 (2003) 393–403.

[2.70] J.H. Schon, G.Binder, E. Bucher, Performance and stability of some new high-temperature selective absorber systems based on metal/dielectric multilayers. Solar Energy Materials and Solar Cells 33 (1994) 403–416.

[2.71] J.I. Gittleman, E.K. Sichel, Y. Arie, Composite semiconductors: selective absorbers of solar energy. Solar Energy Materials 1 (1979) 93–104.

[2.72] C. Sella, A. Kaba, S. Berthier, J. Lafait, Low cost selective absorber based on a Fe-Al_2O_3 cermet film. Solar Energy Materials 16 (1987) 143-154.

[2.73] D. Atasi, K.Chattopadhyay, H.C. Barshilia, B. Basu, Colored selective absorber coating with excellent durability. Thin Solid Films 620 (2016) 17–22.

[2.74] X-H. Gao, C-B. Wang, Z-M. Guo, Q-F. Geng, W.Theiss, G. Liu, Structure, optical properties and thermal stability of Al_2O_3-WC nanocomposite ceramic spectrally selective solar absorbers. Optical Materials 58 (2016) 219-225.

[2.75] X.-H. Gao, Z.-M. Guo, Q.-F. Geng, P.-J. Ma, A.-Q. Wang, G. Liu, Microstructure, chromaticity and thermal stability of SS/TiC-WC/Al_2O_3 spectrally selective solar absorbers. Solar Energy Materials & Solar Cells 164 (2017) 63–69.

[2.76] L. Rebouta, A. Sousa, M. Andritschky, F. Cerqueira, C.J. Tavares, P. Santilli, K. Pischow, Solar selective absorbing coatings based on AlSiN/AlSiON/$AlSiO_y$ layers. Applied Surface Science 356 (2015) 203–212.

[2.77] D. Atasi, A. Biswas, P. Sarkar, S. Kashyap, K. Chattopadhyay, H.C. Barshilia, B. Basua, Enhancing spectrally selective response of W/WAlN/WAlON/Al_2O_3 – Based nanostructured multilayer absorber coating through graded optical constants. Solar Energy Materials and Solar Cells 176 (2018) 157–166.

[2.78] H. Wang, H. Alshehri, H. Su, L. Wang, Design fabrication and optical characterizations of large-area lithographyfree ultrathin multilayer selective solar coatings with excellent thermal stability in air. Solar Energy Materials and Solar Cells 174 (2018) 445–452.

[2.79] I. Heras, E. Guillén, F. Lungwitz, G. Rincón-Llorente, F. Munnik, E. Schumann, I. Azkona, M. Krause, R. Escobar-Galindo, Design of high-temperature solar-selective coatings based on aluminium titanium oxynitrides $Al_yTi_{1-y}(O_xN_{1-x})$. Part 1: Advanced microstructural characterization and optical simulation. Solar Energy Materials and Solar Cells 176 (2018) 81–92.

[2.80] X-H Gao, H-X Guo, T-H Zhou, G. Liu, Optical properties and failure analysis of ZrC-ZrOx ceramic based spectrally selective solar absorbers deposited at a high substrate temperature. Solar Energy Materials and Solar Cells 176 (2018) 93–99.

[2.81] T.X. Wang, Q.H. Zhao, X.X. Chen, The Fabrication and Properties of Anodizing steel solar selective coating. Solar Energy 12(1) (1991) 62-66.

[2.82] Y.W. Zhao, H.F. Huang, Y.B. Zhang, The Optical Properties of Anodizing Aluminum solar selective coating. Solar Energy 6(2) (1985) 135-141.

[2.83] G.E. McDonald, Solar Energy 17 (1975) 119–122.

[2.84] C.P. Lampert, in Second Annual Conference on Absorber Surfaces for Solar Receivers. (1979), Gounder, CO.

[2.85] I.T. Ritchie, S.K. Sharma, J. Valignat, J. Spitz, Solar Energy Materials 2 (1979) 167–176.

[2.86] R.B. Pettit, R.R. Sowell, I.J. Hall, Solar Energy Materials 7 (1982) 153–170.

[2.87] V. Saxena, R. Uma, Rani, A.K. Sharma, Studies on ultra high solar absorber black electroless nickel coatings on aluminum alloys for space application. Surface & Coatings Technology 201 (2006) 855–862.

[2.88] A.R. Shashikala, A.K Sharma, D.R Bhandari, Solar selective black nickel–cobalt were on aluminium alloys. Solar Energy Materials and Solar Cells 91 (2007) 629-635.

[2.89] W. Kruidhof, M. van der Leij, Cobalt oxide as a spectrally selective material for use in solar collectors. Solar Energy Materials 2 (1979) 69-79.

[2.90] D. Ding, H. Wu, X. Yu, Air-stable $NiFeCrO_x$ selective absorber for mid-to-high temperature application. Solar Energy 113 (2015) 43–47.

[2.91] S. N. Kumar, L.K. Malhotra, K.L. Chopra, Nickel Pigmented Anodized Aluminium as Solar Selective Absorbers. Solar Energy Materials 7 (1983) 439-452.

[2.92] N.M. Nahar, G.H. Mo, A. Ignatiev, Development of an Al_2O_3-Co Selective Absorber for Solar Collectors. Thin Solid Films 172 (1989) 19- 25.

[2.93] T. Tesfamichael, Characterisation of Selective Solar Absorbers. Experimental and Theoretical Modeling. Ph.D. Dissertation. Sweden: Uppsala University; (2000).

[2.94] K. Figen, E. Waclelgard, M. Sohmen, Electrochemical characterisation of Al_2O_3 –Ni Thin Film Selective Surface on Aluminium. Turk J Chem 23 (1999) 381-391.

[2.95] A. Cuevas, L. Martínez, R. Romero, E.A. Dalchiele, R. Marotti, D. Leinen, J.R. Ramos-Barrado, F. Martin, Electrochemically grown cobalt-alumina composite layer for solar thermal selective absorbers. Solar Energy Materials & Solar Cells130 (2014) 380–386.

[2.96] A. Wazwaz, J. Salmi, H. Hallak, R. Bes, Solar thermal performance of a nickel pigmented aluminium oxide selective absorber. Renewable Energy 27 (2002) 277–292.

[2.97] M. Zemanova, M. Chovancova, Z. Galikova, P. Krivosık, Nickel electrolytic colouring of anodic alumina for selective solar absorbing films. Renewable Energy 33 (2008) 2303–2310.

[2.98] D.W. Ding, M.C. Long, W.M. Cai, Y.H. Wu, D.Y. Wu, C.Chen, In-situsynthesis of photocatalytic $CuAl_2O_4$-Cu hybrid nanorod arrays. Chem.Commun. (2009) 3588–3590.

[2.99] A. Santibanez, M. Herrera-Trejo, J. Oliva, A.I. Martinez, Electrochemical deposition of Ni-Fe alloys into porous alumina for solar selective absorbers. Superlattices and Microstructures 100 (2016) 973-982.

[2.100] Z. Chen, T. Boström, Accelerated ageing tests of carbon nanotube spectrally selective solar absorbers. Solar Energy Materials & Solar Cells157 (2016) 777–782.

[2.101] M.A. Estrella-Gutiérrez, F.I. Lizama-Tzec, O. Arés-Muzio, G. Oskam, Influence of a metallic nickel interlayer on the performance of solar absorber coatings based on black nickel electrodeposited onto copper. Electrochimica Acta 213 (2016) 460–468.

[2.102] S. John, Electrodeposition of Nickel Black Solar Absorber Coatings. (1997) Central Electrochemical Research Institute, Karaikudi India.

[2.103] K.N. Srinivasan, N.V. Shanmugam, M.Selvam, S. John, B.A. Shenoi, Nickel -black solar absorber coatings. Energy Convers. Mgmt 24 (1984) 255-258.

[2.104] M. Voinea, A. Duta, Electrochemical deposition of black nickel solar absorber coatings on copper substrate for solar thermal applications. Journal of optoelectronics and advanced materials 9 (2007) 1454 - 1456.

[2.105] F. Kadirgan, Electrochemical Nano-Coating Processes in Solar Energy Systems. International Journal of Photoenergy (2006) 1-5.

[2.106] C. Bogatu, M. Voinea, A. Duta, I.M. Pelin, G.C. Chitanu, The electrochemical deposition Cu/CuO_X solar selctice coatings with controlled morphology. Revue Roumaine de Chimie 54(3) (2009) 235–241.

[2.107] R.L.P. Teixeira, J.G. Filho, L.C. de Lima, R.A. Simão, MFM and XPS analysis of black nickel solar absorber electrocoating on nanostructured copper. Programa de Engenharia Metalúrgica e de Materiais, UFRJ, Brazil.

[2.108] S. Jafari, S.M. Rozati, Characterization of black chrome films prepared by electroplating technique. Solar Thermal Applications (2011), Sweden: World Renewable Energy Congress.

[2.109] T. Abendroth, H. Althues, G. Mäder, P. Härtel, S. Kaskel, E. Beyer, Selective absorption of Carbon Nanotube thin films for solar energy applications. Solar Energy Materials & Solar Cells143 (2015) 553–556.

[2.110] B. Cheng, K.K. Wang, K.P. Wang, M. Li, W. Jiang, B.J. Cong, C.L. Song, S.H. Jia, G.R. Han, Y. Liu, Preparation and characterization of porous carbon–titania nanocomposite films as solar selective absorbers. Journal of Alloys and Compounds 635 (2015) 129–135.

[2.111] E. Sani, L. Mercatelli, M. Meucci, A. Balbo, C. Musa, R. Licheri, R. Orrù, G. Cao, Optical properties of dense zirconium and tantalum diborides for solar thermal absorbers. Renewable Energy 91 (2016) 340-346.

[2.112] C. Zhang, Z. Yang, K. Wu, X. Li, Design of a symmetric nanovoid resonator for silicon-based single-nanowire solar absorbers. Nano Energy 27 (2016) 611–618.

[2.113] A.G. Avila, E.C. Barrera, L.A. Huerta, S. Muhl, Cobalt oxide films for solar selective surfaces, obtained by spray pyrolisis. Solar Energy Materials & Solar Cells 82 (2004) 269–278.

[2.114] M. Kotilainen, R. Krumpolec, D. Franta, P. Souček, T. Homola, D.C. Cameron, P. Vuoristo, Hafnium oxide thin films as a barrier against copper diffusion in solar absorbers. Solar Energy Materials & Solar Cells 166 (2017) xxx–xxx.

[2.115] E. Ollier, N. Dunoyer, H. Szambolics, G. Lorin, Nanostructured thin films for solar selective absorbers and infrared selective emitters. Solar Energy Materials and Solar Cells 170 (2017) 205–210.

[2.116] A.A. Ziabari, A.B. Khatibani, Optical properties and thermal stability of solar selective absorbers based on Co-Al_2O_3 cermets. Chinese Journal of Physics 000 (2017) 1–10.

[2.117] L. Kaluza, A.S. Vuk, B. Orel, Structural and Spectroscopic Analysis of Sol-gel Processed $CuFeMnO_4$ Spinel and $CuFeMnO_4$/silica Films for Solar Absorbers. Sol- Gel Science and Technology 20 (2001) 61-83. .

[2.118] L. Kaluza, B. Orel, G. Drazic et al. Sol-gel Derived CuCoMnOx Spinel Coatings for Solar Absorbers: Structural and Optical Properties. Solar Energy Materials and Solar Cells 70 (2001) 187-201.

[2.119] T. Bostrom, Solution-Chemically derived spectrally selective solar absorbers. Ph.D. Dissertation. Sweden Uppsala: University; (2006).

[2.120] Z. Li, J. Zhao, L. Ren, Solar Energy Materials and Solar Cells 105 (2012) 90–95.

[2.121] X. Wang, C. Li, G. Chen, L. He, H. Cao, B. Zhang, Selective fabrication of Cu/Cu_2O nanowires using porous alumina membranes in acidic solution. Solid State Science 13 (2011) 280–284.

[2.122] Z. Li, J. Zhao, L. Ren, Aqueous solution-chemical derived Ni–Al_2O_3 solar selective absorbing coatings. Solar Energy Materials & Solar Cells 105 (2012) 90–95.

[2.123] S. Khamlich, O.Nemraoui, N. Mongwaketsi, R. McCrindle, N.Cingo, M. Maaza, Black Cr/a-Cr_2O_3 nanoparticles based solar absorbers. Physica B 407 (2012)1509–1512.

[2.124] S.Khamlich, R. McCrindle, Z.Y. Nuru, N.Cingo, M.Maaza, Annealing effect on the structural and optical properties of Cr-Cr_2O_3 monodispersed particles based solar absorbers. Applied Surface Science 265 (2013) 745-749.

[2.125] N. Mongwaketsi, S.Khamlich, B. Klumperman, R. Sparrow, M. Maaza, Synthesis and characterization of porphyrin nanotubes/rods for solar radiation harvesting and solar cells. Physica B407(2012) 1615–1619.

[2.126] K.K. Wang, Z.Z. Wu, C.J. Peng, K.P. Wang, B. Cheng, C.L. Song, G.R. Han, Y. Liu, A facile process to prepare crosslinked nano-graphites uniformly dispersed in titanium oxide films as solar selective absorbers. Solar Energy Materials & Solar Cells 143 (2015) 198-204.

[2.127] M. Joly, Y. Antonetti, M. Python, M. Gonzalez, T. Gascou, J-L. Scartezzini, A. Schuler, Novel black selective coating for tubular solar absorbers based on a sol–gel method. Solar Energy 94 (2013) 233–239.

[2.128] G. Katumba, L. Olumekor, A. Forbes, G. Makiwa, B. Mwakikunga, J. Lu, E. Wackelgard, Optical, thermal and structural characteristics of carbon nanoparticles embedded in ZnO and NiO as selective solar absorbers. Solar Energy Materials & Solar Cells 92 (2008) 1285– 1292.

[2.129] T. Boström, S. Valizadeh, J. Luc, J. Jensen, G. Westin, E. Wäckelgård, Structure and morphology of nickel-alumina/silica solar thermal selective absorbers. Journal of Non-Crystalline Solids 357 (2011) 1370–1375.

[2.130] Q.-C. Zhang, Stainless-steel–AlN cermet selective surfaces deposited by direct current magnetron sputtering technology. Solar Energy Materials and Solar Cells 52 (1998) 95–106.

[2.131] W. Weiss, F. Mauthner, Solar Heat Worldwide, AEEINTEC and IEA Solar Heating and Cooling Programme, May (2010).

[2.132] TiNOX Energy, commercial TiN_xO_y cermet on Cu substrate. <www.almeco-tinox.com>.

[2.133] A. Bittar, D. Cochrane, S. Caughley, I. Vickeridge, Study of TiO_xN_y thin film selective surfaces produced by ion assisted deposition. Journal of Vacuum Science and Technology A 15 (1997) 223–229.

[2.134] Bluetec eta plus coating. <www.bluetec-germany.com>.

[2.135] W. Graf, F.Brucker, M. Kohl, T.Troscher, V. Wittwer, L.Herlitze, Development of large area sputtered solar absorber coatings. Journal of Non-Crystalline Solids 218 (1997) 380–387.

[2.136] Sunselect (CrN/Cr_2O_3 on Cu substrate) coatings, <http://alanodsolar.com/opencms/opencms/Absorption/Produkte.html>.

[2.137] E. Wackelgard, G. Hultmark, Industrially sputtered solar absorber surface. Solar Energy Materials and Solar Cells 54 (1998)165–170.

[2.138] T. Tesfamichael, E. Wackelgard, Angular solar absorptance and incident angle modifier of selective absorbers for solar thermal collectors. Solar Energy 68 (2000) 335–341.

[2.139] <http://en.ssolar.com/>.

[2.140] A.Schuler, J.Geng, P.Oelhafen, S.Brunold, P.Gantenbein, U.Frei, Application of titanium containing amorphous hydrogenated carbon films (a-C:H/Ti) as optical selective solar absorber coatings. Solar Energy Materials and Solar Cells 60 (2000) 295–307.

[2.141] A. Schuler, I.R. Videnovic, P. Oelhafen, S. Brunold, Titanium-containing amorphous hydrogenated silicon carbon films (a-Si:C:H/Ti) for durable solar absorber coatings. Solar Energy Materials and Solar Cells 69 (2001) 271–284.

[2.142] P.Oelhafen, A. Schuler, Nanostructured materials for solar energy conversion. Solar Energy 79 (2005) 110–121.

[2.143] M. Lanxne, Z. Elgat, Solar selective absorber coating for high service temperatures produced by plasma sputtering. Proceedings of the Society of Photo-Optical Instrumentation Engineers1272 (1990) 240–249.

[2.144] <http://www.energy.siemens.com/hq/en/power-generation/renewables/solar-power/concentrated-solar-power/receiver.htm>.

[2.145] <http://www.archimedesolarenergy.com/receiver_tube.htm>.

[2.146] S. Esposito, A. Antonaia, M.L. Addonizio, S. Aprea, Fabrication and optimiza-tion of highly efficient cermet-based spectrally selective coatings for high operating temperature. Thin Solid Films 517 (2009) 6000–6006.

[2.147] A. Antonaia, S. Esposito, G. Nobile, S. Aprea, L.M. Addonizio, Spectrally selective surface coating of the receiver tube of a solar concentrator, and method for the manufacture thereof,World Intellectual Property Organization, WO 2005/121389 A1, 2005.

CHAPTER 3

THEORETICAL BACKGROUND OF SELECTIVE SOLAR ABSORBERS

This chapter gives a general introduction to the fundamental theories used to build laser structured ferromagnetic nanorods embedded in alumina matrix. It starts with thin film optics and the physical background of spectrally selective absorbers. As any optical phenomenon is connected with the interaction of electromagnetic radiation with matter, it is worth to understand the basic electromagnetic wave theory that governs the physics of well-designed spectrally selective absorbing surfaces. This chapter will therefore describe how electromagnetic waves interact with matter in thin films; it also includes Effective Medium Theories Maxwell Garnett as well as the Bruggeman effective medium model for inhomogeneous materials. The last section is on surface structuring, the main interest of this section is to conduct a quick review of the available structuring methods and introduce the reader to the most applicable ones in the solar industry.

3.1 THIN FILM OPTICS

An optical coating consists of a combination of thin film layers that create interference effects used to enhance transmission or reflection properties for an optical system. How well an optical coating performs is dependent upon the number of factors, including the number of layers, the thickness of each layer and the differences in refractive index at the layer interfaces. The transmission properties of light are predicted by wave theory. One outcome of the wave properties of light is that waves exhibit interference effects. Light waves that are in phase with each other undergo constructive interference, and their amplitudes are additive. Light waves exactly out of phase with each other (by 180°) undergo destructive interference, and their amplitudes cancel. It is through the principle of optical interference that thin film coatings control the reflection and transmission of light [3.1].

When designing a thin film, though the wavelength of light and angle of incidence are usually specified, the index of refraction and thickness of layers can be varied to optimize performance. As refraction and thickness are adjusted these will have an effect on the path length of the light rays within the coating which, in turn, will alter the phase values of the propagated light. As light travels through an optical component, reflections will occur at the two interfaces of refractive index change on either side of the coating [3.1]. In order to

minimize reflection, ideally there should be a 180° phase shift between these two reflected portions when they recombine at the first interface. This phase difference correlates to a λ/2 shift of the sinusoid wave, which is best achieved by adjusting the optical thickness of the layer to λ/4. Fig. 3.1 shows an illustration of this concept.

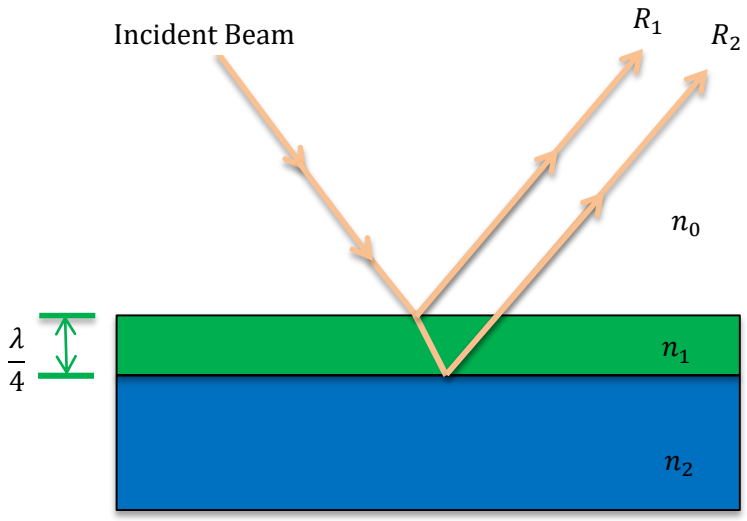

Figure 3.1: 180° phase shift for an air (n_0)/film (n_1) interface between the two reflected beams (R_1, R_2), resulting in destructive interference of the reflected beams.

Index of refraction influences both optical path length (and phase), but also the reflection properties at each interface. The reflection is defined through Fresnel's Eqn. 2.1, which provides the amount of reflection that will occur from the refractive index change at an interface at normal incidence [3.1]:

$$R = \frac{(N-1)^2}{(N+1)^2} \qquad 3.1$$

The intensity of reflected light is not only a function of the ratio of the refractive index of the two materials, but also the angle of incidence and polarization of the incident light. If the incident angle of the light is altered, the internal angles and optical path lengths within each layer will be affected, which also will influence the amount of phase change in the reflected beams [3.1]. It is convenient to describe incident radiation as the superposition of two plane-polarized beams, one with its electric field parallel to the plane of incidence (p-polarized) and the other with its electric field perpendicular to the plane of incidence (s-polarized). When a non-normal incidence is used, s-polarized and p-polarized light will reflect differently at each interface which will cause different optical performances at the two polarizations.

Determining the refractive index, *n*, and the absorptance (absorption coefficient), *k*, of a coating are two important parameters in thin film research. In real materials, the polarization does not respond instantaneously to an applied field [3.2]. This causes dielectric loss, which can be expressed by the complex index of refraction defined by Eqn. 2.2:

$$N = n + ik \qquad 3.2$$

where:

N = the complex refractive index

i = the square root of -1

n = the refractive index

k = the absorption index

Here, k indicates the amount of absorption loss when the electromagnetic wave propagates through the material. The term k is often called the extinction coefficient in physics. Both n and k are dependent on the wavelength. In most circumstances k > 0 (light is absorbed).

3.2 OPTICAL CHARACTERIZATION OF A SELECTIVE SOLAR ABSORBER

When incident light strikes a surface of a solid material, some part of the incident light is reflected, some part is absorbed, and some part is transmitted. Reflectance, transmittance and absorptance are the three parameters which describe characteristics of a selective solar absorber surface, they are wavelength dependent. For a given incident angle θ, reflectance, $R(\lambda)$ is the fraction of incident light at a specific wavelength λ that is reflected by the surface, absorptance, $\alpha(\lambda)$ is the fraction of incident radiation that is absorbed by the surface and transmittance, $T(\lambda)$is the fraction of incident light that passes through the surface.

To calculate the absorption coefficient (re: absorptance, extinction) of a thin film the transmission and absolute reflectance spectra of the material needs to be acquired (it follows that the material cannot be opaque).

Energy conservation [3.3] gives Eqn. 2.3 which describes the theory:

$$\alpha(\lambda) + R(\lambda) + T(\lambda) = 1 \qquad 3.3$$

If the surface is opaque the transmittance $T(\lambda)$is equal to zero and the angular solar absorptance can be expressed in terms of the angular reflectance:

$$\alpha(\lambda) = 1 - R(\lambda) \quad 3.4$$

The emittance is described as the ability of a surface to radiate thermal power. It is the ratio of the radiant energy emitted by the heated surface to the radiant energy emitted by the blackbody at the same temperature and wavelength. According to Kirchoff's law, for an opaque object it can be concluded that the absorptance is equal to the emittance [3.4].

As $\varepsilon(\lambda) = \alpha(\lambda)$: 3.5

$$\varepsilon(\lambda) = \alpha(\lambda) = 1 - R(\lambda) - T(\lambda) \quad 3.6$$

If the surface is opaque the transmittance, $T(\lambda)$is equal to zero and the angular absorptance can be expressed in terms of the angular reflectance:

$$\varepsilon(\lambda) = \alpha(\lambda) = 1 - R(\lambda) \quad 3.7$$

R(λ,θ) is the sum of both collimated and diffuse reflectance. The performance of spectrally selective materials depends on reliable characterization of their optical properties [3.5-3.6].

The performance of a candidate solar absorber can be characterized by its absorptance and emittance. The total normal solar absorptance is the weight average of the spectral absorptance with the spectral solar irradiance and integrating over the wavelengths in which the solar radiation reaches the absorber surface, as shown in Eqn. 2.8. For high temperature applications (>400 ˚C), the integral limits are fixed at $\lambda_{\min} = 300\ \text{nm}$ and $\lambda_{\max} = 50000\ \text{nm}$ [3.5-3.6].

$$\alpha = \frac{\int_{\lambda_{\min}}^{\lambda_{\max}} I_{sol}(\lambda)[1 - R(\lambda)]d\lambda}{\int_{\lambda_{\min}}^{\lambda_{\max}} I_{sol}(\lambda)d\lambda} \quad 3.8$$

Thermal emittance is defined as a fraction of radiant energy emitted by the heated surface as compared with the radiation energy emitted by the blackbody at the same temperature and wavelength. It is a weighted average typically measured at room temperature, though it can be measured at other temperatures. Emittance defined in Eqn. 3.9 is frequently reported from reflectance data fitted to blackbody curves:

$$\varepsilon(\mathrm{T}) = \frac{\int_{\lambda_{\min}}^{\lambda_{\max}} [1 - \rho(\lambda, \mathrm{T})] B(\lambda, \mathrm{T}) d\lambda}{\int_{\lambda_{\min}}^{\lambda_{\max}} B(\lambda, \mathrm{T}) d\lambda} \qquad 3.9$$

B(λ,T) is the emitted spectral irradiance of a blackbody at temperature T and wavelength λ.

$$B(\lambda, \mathrm{T}) = \frac{c_1}{\lambda^5 \left[e^{\left(\frac{c_2}{\lambda \mathrm{T}}\right)} - 1 \right]} \qquad 3.10$$

where c_1=3.7405x10^{8} Wμm^{4} m^{-2} and c_2=1.43879x10^{4} μm K, which are Planck's first and second radiation constants, respectively.

The actual performance of an absorber at high temperatures may not correspond to the calculated emittance [3.5-3.6]. This is because small errors in measured ρ can lead to large errors in small values of ε. In addition, for some materials the measured emittance data at two different temperatures may simply be different.

Solar reflectance measurements are usually performed in the wavelength range 0.3-2.5 μm at near normal (θ = 2) angle of incidence using standard spectrophotometers. The solar absorptance is characterized at near normal incidence for which the sun is at the zenith angle relative to the absorber [3.5-3.6]. When the sun is at other elevations than the zenith, i.e oblique incidence the near normal solar absorptance must be modified using the angle of incidence modifier.

To evaluate the performance of solar absorber material, the absorptance and emittance are usually combined in the figure of merit *f* called selectivity. High value of *f* indicates high performance, which is defined as:

$$f = \frac{\alpha}{\varepsilon} \qquad 3.11$$

3.3 ELECTROMAGNETIC RADIATION AND ABSORPTION

A plane electromagnetic wave propagating along the x-axis through an absorbing medium at time *t* is defined by its electric field component, *E(x,t)* described by the following progressive wave equation 3.12 [3.5-3.7]:

$$E = E_0 \exp(-\mathrm{k}\omega x/c + i(\mathrm{k}\omega x/c - \omega t)) \qquad 3.12$$

E_0 is the initial amplitude of the electromagnetic wave of angular frequency ω before it enters the medium. The speed of light in vacuum is denoted c.

From Maxwell's equations on electromagnetic theory, the speed of light in a vacuum is related to the permittivity of free space, (the degree to which a medium can resist the flow of charge, defined by the ratio of the electric displacement to the intensity of the electric field that produces it), and the permeability of free space (the ratio of the magnetic flux density in a solid to the external magnetic field strength inducing) is expressed by [3.5-3.7]:

$$c = \frac{1}{\sqrt{\mu_0 \varepsilon_0}} \qquad 3.13$$

The velocity of propagation through the solid of complex refractive index, is related $N = n + ik$ to the speed of light in a vacuum, *C*, by Eqn. 3.14

$$\nu = \frac{c}{N} \qquad 3.14$$

$$\frac{1}{\nu} = \frac{n}{\mathrm{c}} - \frac{ik}{\mathrm{c}} \qquad 3.15$$

Therefore, substituting $\frac{1}{\nu}$ into equation 2.12 gives:

$$E = E_0 \exp i2\pi f t \exp\left(\frac{-2\pi f \mathrm{k} x n}{c}\right) \exp\left(\frac{-2\pi f \mathrm{k}\omega n}{c}\right) \qquad 3.16$$

where the last exponential term is the measure of the damping factor or extinction coefficient

The power P or intensity of an incident wave through a solid is the conductivity σ of the solid multiplied by the square of the electric field vector [3.5-3.7]. Using the damping factor

term, the fraction of the incident power that has propagated from position (*0*) to a distance x through the material with conductivity is given σ by:

$$\frac{P(x)}{P(x)} = \frac{\sigma E^2(x)}{\sigma E^2(0)} \exp\left(\frac{-4\pi f \mathrm{k} x}{c}\right) \qquad 3.17$$

from which the absorption coefficient α can be expressed in terms of the extinction coefficient as:

$$\alpha = \frac{4\pi f \mathrm{k}}{c} \qquad 3.18$$

The velocity of light in a vacuum is $C = f\lambda$, and the power or intensity is $P = E_0 \exp -\alpha x$ which is known as Lambert's law of absorption, by which radiation is absorbed to an extent that depends on the wavelength of the radiation and the thickness and nature of the medium [3.5-3.7].

Due to Maxwell's equations, the complex dielectric function is related to the complex index of refraction in a non-magnetic medium by:

$$\varepsilon = N^2 \qquad 3.19$$

The real and imaginary parts of the dielectric function ε are given by:

$$\varepsilon = \varepsilon_1 + i\varepsilon_2 = (n \pm ik)^2 \qquad 3.20$$

One obtains $n \pm ik$ by choosing the form of the plane-wave solution to Maxwell's equations as$\exp(\omega t \pm q.r)$. This choice also determines signs in the Lorentz-Oscillator formula for lattice vibrations [3.5-3.7]. We have chosen the tabulated n and k because it is then an easy matter to obtain the relations of Eqn. 3.21 as well as the intensity based reflectivity *R* (Eqn. 3.22):

$$\varepsilon_1 = n^2 + k^2 \text{ and } \varepsilon_2 = 2nk \qquad 3.21$$

Generally, the real part of the refractive index relates to the phase of the wave, the imaginary part describes a damping of the amplitude in the direction of propagation and the dielectric function is more suited when we describe the microscopic effects inside a solid. For the normal incidence, the reflectivity is [3.8]:

$$\mathrm{R} = \left|\frac{(\mathrm{N}-1)^2}{(\mathrm{N}+1)^2}\right| = \frac{1 - n^2 + k^2}{1 + n^2 + k^2} \qquad 3.22$$

2.3.1 The Lorentz model

An incident electromagnetic field will cause various types of oscillators in matter to perform forced oscillations. The Lorentz model is a classical model for the response of bound charge or electron to an EM wave, it expresses the complex dielectric constant as a function of material parameters such as resonance frequency, damping constant and plasma frequency [3.9-3.10].

$$\frac{d^2\mathbf{r}}{dt^2} + \Gamma \frac{dy}{dx} + {\omega_0}^2\mathbf{r} = -\left(\frac{e}{m}\right) E_x \qquad 3.23$$

m is the mass of the electron,

e is the magnitude of the electron charge,

Γ is the dumping force,

E_x is the local electric field acting on the electron as the driving force.

ω_0 is the resonance frequency

To solve equation, assume

$$\boldsymbol{R}(t) = De^{-i\Gamma t} \qquad 3.24$$

Substituting Eqn. 3.24 into 3.23 and solving for Dgives:

$$\boldsymbol{R}(t) = \frac{eE_0}{m}\left(\frac{e^{-i\omega t}}{{\omega_0}^2 - \omega^2 i\Gamma\omega}\right) \qquad 3.25$$

The induced dipole moment due to the charge displacement is given by:

$$\boldsymbol{P}(t) = -e.\boldsymbol{R}(t) = \frac{e^2E_0}{m}\left(\frac{e^{-i\omega t}}{{\omega_0}^2 - \omega^2 i\Gamma\omega}\right) \qquad 3.26$$

If there are N atoms per unit volume, the induced polarization vector through the volume is given by:

$$\boldsymbol{P}(w) = N\langle\boldsymbol{P}(t)\rangle = \chi_e\,\mathbf{E} \qquad 3.27$$

The polarization of the material is proportional to the strength of the electric field. The polarization factor characterizes the polarization density of the medium under the influence of the electric field and it excludes the vacuum contribution [3.9-3.10]. The constant of proportionality is called the electrical susceptibility of the material.

$$\varepsilon = 1 + 4\pi N \qquad 3.28$$

Using the polarizability for one electron, the real ε_1 and imaginary ε_2 parts of the dielectric function become:

$$\varepsilon_1 = n^2 + k^2 = 1 + \frac{4\pi N e^2}{m}\left(\frac{1}{({\omega_0}^2 - \omega^2) - i\Gamma\omega}\right) \qquad 3.29$$

Using Eqns. 3.21 and 3.26,

$$\varepsilon_2 = 2nk = \frac{4\pi N e^2}{m}\left(\frac{\Gamma\omega}{({\omega_0}^2 - \omega^2)^2 - i\Gamma\omega}\right) \qquad 3.30$$

where:

$$\omega_p^2 = \frac{Ne^2}{m\varepsilon_0} \qquad 3.31$$

ω_p is called the plasma frequency, it corresponds to the photon energy position where ε_1 is approximately zero. As ω_p increases the amplitude of ε_1 and ε_2 increases too.

If the electrons in plasma are displaced from a uniform background of ions, electric fields will be built up in such a direction as to restore the neutrality of the plasma by pulling the electrons back to their original positions [3.9-3.10]. Because of their inertia, the electrons will overshoot and oscillate around their equilibrium positions with a characteristic frequency known as the plasma frequency.

- **At high frequencies $\boldsymbol{\omega >> \omega_0}$** , the amplitude vanishes. Has a physical significance of the frequency at which the system resonates or absorbs strongly. In this case the absorption becomes less significant, as expected in a frequency range away from resonance. Eqns. 3.29 and 3.30 are reduced to:

$$\varepsilon_1 = 1 + \omega_p{}^2 . \frac{\omega^2}{\omega^4 + \Gamma^2 \omega^2} \quad \text{and} \quad \varepsilon_2 = \omega_p{}^2 . \frac{\Gamma\omega}{\omega^4 + \Gamma^2 \omega^2} \qquad 3.32$$

- **At low frequencies $\boldsymbol{\omega \ll \omega_0}$** the response is below resonance, frequency ω is less than ω_0 and the amplitude has a medium finite value and is in phase with Eqns. 3.29 and 3.30 is rewritten as:

$$\varepsilon_1 = 1 + \frac{\omega_p{}^2}{\omega_0{}^2} . \frac{1}{1 + \left(\frac{\Gamma\omega}{\omega_0{}^2}\right)^2} \quad \text{and} \quad \varepsilon_2 = \omega_p{}^2 . \frac{\Gamma\omega}{\omega^4 + \Gamma^2 \omega^2} \qquad 3.33$$

- At resonance frequency $\boldsymbol{\omega = \omega_0}$, the amplitude is imaginary and maximum when denominator is minimum. There is also a 90° phase shift between v

For dielectric aluminium oxide, the Lorentz oscillatory model can be used to model the ionic oscillation with the resonant absorption located suitably above the UV. Fig. 3.2 illustrates the optical properties (n, k and normal bulk reflectance R) of Al_2O_3 in the UV-VIS-NIR region [3.11]. One can observe that the refractive index is greater than the extinction coefficient, $n > k, k = 0$ the material becomes transparent

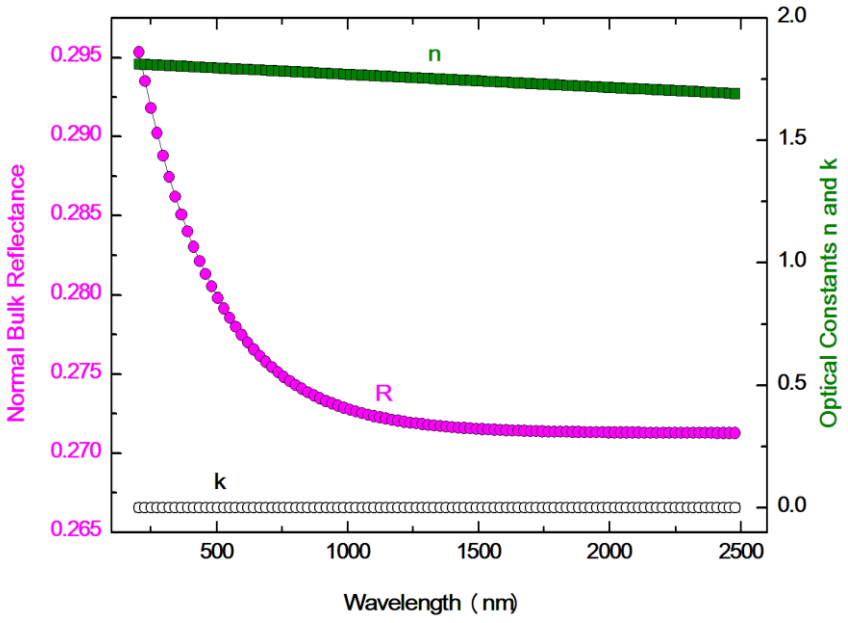

Figure 3.2: Optical properties (*n*, *k*, and normal bulk reflectance R) of Aluminium oxide as a function of wavelength

2.3.2 Drude Model

Drude's model (1900) developed by Paul Drude was constructed in order to explain the transport properties of conduction electrons in metals (due to intra-band transitions in a quantum-mechanical interpretation). It is based on the kinetic theory of electrons in a metal that assumes that the material has motionless positive ions and a non-interacting electron gas [3.9-3.10]. The Drude model is an extension of the Lorentz model to a case where the restoring force and the resonance frequency are zero ($m{\omega_0}^2 x = 0,\ {\omega_0}^2 \to 0$). Using this condition in Eqn. 2.29 and 2.30, the real ε_1 and imaginary ε_2 parts of the dielectric function become:

$$\varepsilon_1 = 1 - \frac{{\omega_p}^2}{\omega^2 - \Gamma^2} \qquad \text{and} \qquad \varepsilon_2 = \frac{{\omega_p}^2 . \Gamma}{\omega(\omega^2 - \Gamma^2)} \qquad 3.34$$

- If $\boldsymbol{\omega > \omega_p}$ the optical frequency is greater than the plasma frequency; the imaginary part ε_2 of the dielectric function tends to zero, this indicates that $k \to 0$, and the refractive index of the metal is almost real [3.9-3.10]. At this high frequency the reflectivity decreases and the metal becomes transparent; the electrons in the metal cannot react fast enough to the incident electric field.

- If $\boldsymbol{\omega < \omega_p}$ the optical frequency is less than the plasma frequency; the real part ε_1 of the dielectric function ε becomes negative. At this frequency no EM field can penetrate the totally reflective metal, the optical constants n and k of the metal are complex.

- If $\boldsymbol{\omega = \omega_p}$, the optical frequency is less than the plasma frequency; the real part ε_1 of the dielectric function tends to zero. This indicates that all electrons oscillate in phase throughout the metal propagation length.

Cobalt and Nickel are metals belonging to the iron group, they are not real free electron metals. Fig. 3.3 and Fig. 3.4 show the optical properties (*n*, *k* and normal bulk reflectance R) of cobalt and nickel respectively [3.11]. The reflectance in the solar range shows a noticeable slope towards short wavelengths, and this is caused by the low energy interband transitions

among the d-electrons [3.10]. The optical properties also show that $k > n > 0$ results in negative dielctric constant which indicates that light is rejected by metals.

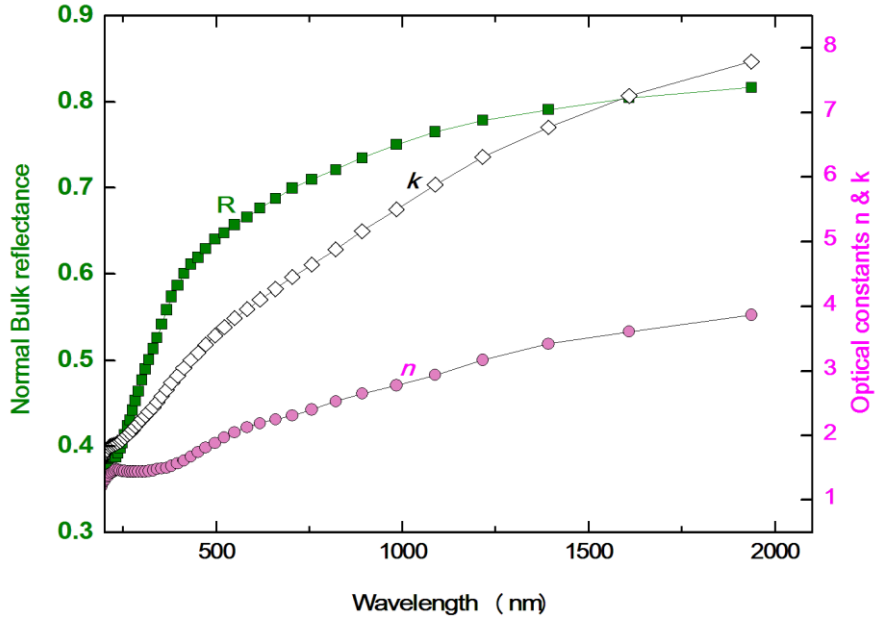

Figure 3.3: Optical properties (n, k, and R) of cobalt illustrated as function of wavelength

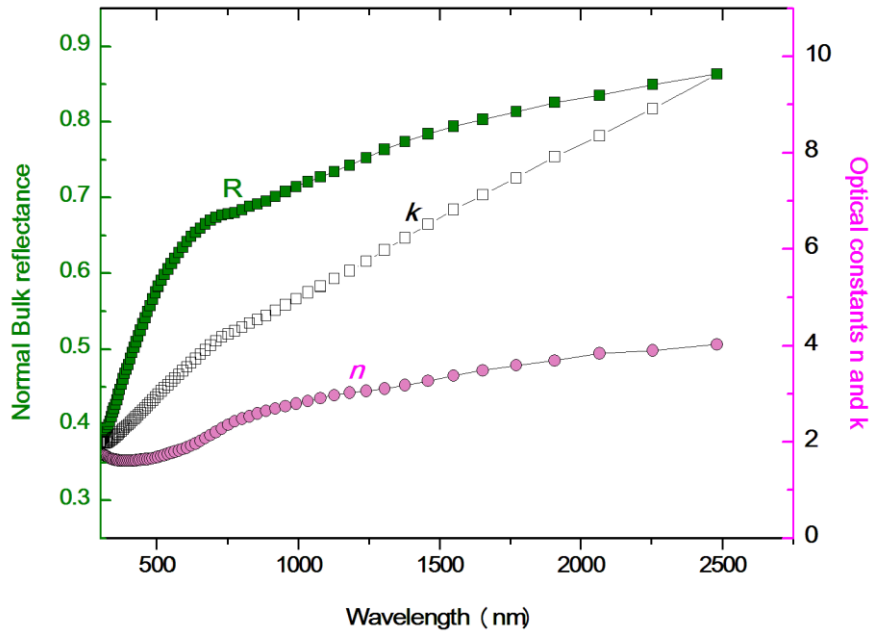

Figure 3.4: Optical properties (n, k, and R) of cobalt illustrated as function of wavelength

3.4 MULTILAYER REFLECTION

As shown in Fig. 3.1 a fraction of light is reflected from the surface which can be a single or more layers. A branch of optics that deals with very thin structured layers of different materials is called thin film optics. In order to exhibit thin-film optics, the thickness of the layers of material must be of the order of the wavelengths of visible light (about 500 nm) [3.7]. Layers at this scale can have remarkable reflective properties due to light wave interference and the difference in refractive index between the layers, air, and substrate. The reflection of a multilayer consisting of several thin, flat and homogeneous films with known optical constants can be calculated typically according to the matrix method [3.12]. However, for two- and three-layer thin films, it is more convenient to use a summation method by extending equations used in the single layer case as shown below.

For a single homogeneous thin film, two boundaries are considered for the optical behaviour. The numbering of the boundary adheres to the convention of optical multilayer, i.e. counting from the top to the substrate. Thus, complex amplitude reflection on the first (air/thin film) and second (thin film/substrate) boundaries are presented as r_1, r_2 in Eqns. (3.35) and (3.36) respectively assuming semi-infinite of materials exists on both sides [3.12]:

$$r_1 = \frac{N_0 + N_1}{N_0 + N_1} \qquad 3.35$$

$$r_2 = \frac{N_1 - N_2}{N_1 + N_2} \qquad 3.36$$

Where N_0, N_1, N_2 are the complex optical constants of air (vacuum), thin film, and substrate material respectively. The complex amplitude reflection of such homogeneous thin film is expressed in Eqns. (3.37) [3.12].

$$r = \frac{r_1 + r_2 e^{-2i\delta_1}}{1 + r_1 r_2 e^{-2i\delta_1}} \qquad 3.37$$

The change in phase is given by:

$$\delta_1 = -\frac{2\pi}{\lambda} N_1 d_1 \qquad 3.38$$

Where d_1 is the film thickness, λ is the wavelength and the term $e^{-2i\delta_1}$ contains phase shift information and is further expressed by:

$$e^{-2i\delta_1} = \exp -4\pi\, k_1\, {}^{\mathrm{d}}/_{\lambda} \cos 4\,\pi\, {}^{\mathrm{d}}/_{\lambda} + i\sin\pi n_1\, {}^{\mathrm{d}}/_{\lambda} \qquad 3.39$$

In the above Eqn. (3.39), the factor $4n_1\, {}^{\mathrm{d}}/_{\lambda}$controls the periodicity of sine, cosine functions, which determine thin film interference property [3.7].

For double layers, there are three interfaces. Eqns. (3.35) and (3.36) is extended to the third interface having amplitude reflection:

$$r_2 = \frac{N_2 - N_3}{N_2 + N_3} \qquad 3.40$$

Similarly, the phase change in layer 2 is expressed as:

$$\delta_2 = -\frac{2\pi}{\lambda} N_2 d_2 \qquad 3.41$$

Starting from the base layer, i.e. layer 2, the total reflected amplitude between boundary 2 and 3 is

(compared with equation (3.37)) [3.7]:

$$r_{L2} = \frac{r_2 + r_3 e^{-2i\delta_2}}{1 + r_2 r_3 e^{-2i\delta_2}} \qquad 3.42$$

Then the total reflection of double layer can then be obtained by replacing r_2 with the term r_{L2} in equation (3.42),

$$r = \frac{r_1 + r_{L2} e^{-2i\delta_1}}{1 + r_1 r_{L2} e^{-2i\delta_2}} \qquad 3.43$$

Following the same procedures from the above equations to three layers the total reflection obtained can be calculated by:

$$r = \frac{r_1 + r_{L3}e^{-2i\delta_1}}{1 + r_1 r_{L3}e^{-2i\delta_2}} \qquad 3.44$$

2.5 EFFECTIVE MEDIUM THEORY

Effective Medium Theory is employed for the metal-dielectric composite coatings. For composite media consisting of small particles in a dielectric matrix, the dielectric constant is assumed to be equivalent to the dielectric constants of the homogeneous constituents. In effective medium theory, we adopt the quasistatic approximation which requires that the size of the grains is much less than the wavelength of the incident light. Generally, metal-dielectric composite solar selective coating is prepared by sputtering and the particle sizes is less than the wavelength of the solar and infrared region. Thus, the optical properties of the composite coatings can be calculated by Effective Medium Theory. The most commonly used Effective Medium Theories are the Maxwell-Garnett and Bruggeman models [3.13-3.14].

Consider two different media A and B (A is embedded in the B), with specific volume fractions i.e. fill factors f_A and f_B, where $f_B = 1 - f_A$ with their respective dielectric constants ε_A and ε_B. According to Electrostatics, we can obtain the following equation [3.13-3.14]:

$$\frac{\varepsilon - \varepsilon_h}{\varepsilon + 2\varepsilon_h} = f_A \frac{\varepsilon_A - \varepsilon_h}{\varepsilon_A + 2\varepsilon_h} + f_B \frac{\varepsilon_B - \varepsilon_h}{\varepsilon_B + 2\varepsilon_h} \qquad 3.45$$

where ε is the dielectric constant of the composite and ε_h is the dielectric constant of surrounding medium. The Maxwell-Garnett model assumes that composite medium has a separated grain structure In Maxwell-Garnett model, when A is embedded in B and B is the surrounding medium ($f_B > f_A$) $\varepsilon_h = \varepsilon_B$. Then the Maxwell-Garnett equation is:

$$\frac{\varepsilon - \varepsilon_B}{\varepsilon + 2\varepsilon_B} = f_A \frac{\varepsilon_A - \varepsilon_B}{\varepsilon_A + 2\varepsilon_B} \qquad 3.46$$

The Bruggeman Model is considered an aggregate structure based on random mixture of the two components. It is valid when the size of the inhomogeneities is much smaller than the

wavelength of the incoming electromagnetic radiation [3.13-3.14]. The model calculates the effective dielectric function ε_{Br} given by:

$$0 = f_A \frac{\varepsilon_A - \varepsilon_{Br}}{\varepsilon_A + 2\varepsilon_{Br}} + (1 - f_A) \frac{\varepsilon_B - \varepsilon_{Br}}{\varepsilon_B + 2\varepsilon_{Br}} \qquad 3.47$$

2.6 DIFFERENT TECHNIQUES OF SURFACE STRUCTURING

The most common micro patterning methods are: optical photolithography, e-beam lithography, imprint lithography, replica molding, micro contact printing, laser writing, holographic patterning and direct laser interference patterning [3.15]. Existing micro-structuring techniques can be categorized into two main groups depending on their processing; one, the methods, which require a mechanical process such as printing, molding or embossing and two, those process that are activated by light, ions or electrons such as optical lithography, laser writing, holographic patterning and direct laser interference patterning . In general, a lithographic technique is built upon following key elements: A pre-designed set of patterns in the form of a mask or a master, a means to mediate the transfer or replication patterns, a responsive medium, which is usually a functional material capable of serving as the resist for subsequent steps.

2.6.1 Optical lithography

In optical lithography, printing is done by projection the image of the pattern onto the substrate using a light source, photo-mask and negative or positive photo-resist.

2.6.2 E-beam lithography

Electron beam lithography is a method with higher resolution than optical lithography, which removes the resist film by its focused electron beam [3.15]. It is not suitable for large patterning area and needs expensive apparatus but it has the advantage that no mask is required.

2.6.3 Laser structuring

- **Laser structuring using photo-resist**

A focused laser beam scans a substrate coated with a polymer resin containing a unique dye to create a desired hardened polymer structure according to the preprogrammed

pattern. To get 2D structures a photo-resist layer is exposed twice against of focal point of laser pattern [3.16]. In comparison to that, holographic method is faster and is done by interfering two or more laser beams. The resulted pattern is then recorded in an exposed photo-resist film.

- **Direct laser structuring**

This technique uses interference of 2 or more laser-beams, like in holographic laser patterning but no photo-resist or special active medium is required. Compared to the more common lithography methods for surface roughening of solar absorbers, the novelty of laser interference micro patterning lies in the fact that only one processing step is required [3.15]. It enables direct processing of the probe itself rather than the exposure of the photo resist film. Using laser micro-structuring, surface micro- patterns from 2 up to 20 µm can easily be created in only one simple step by femto- or nano-second laser pulses, see Fig. 3.5 below.

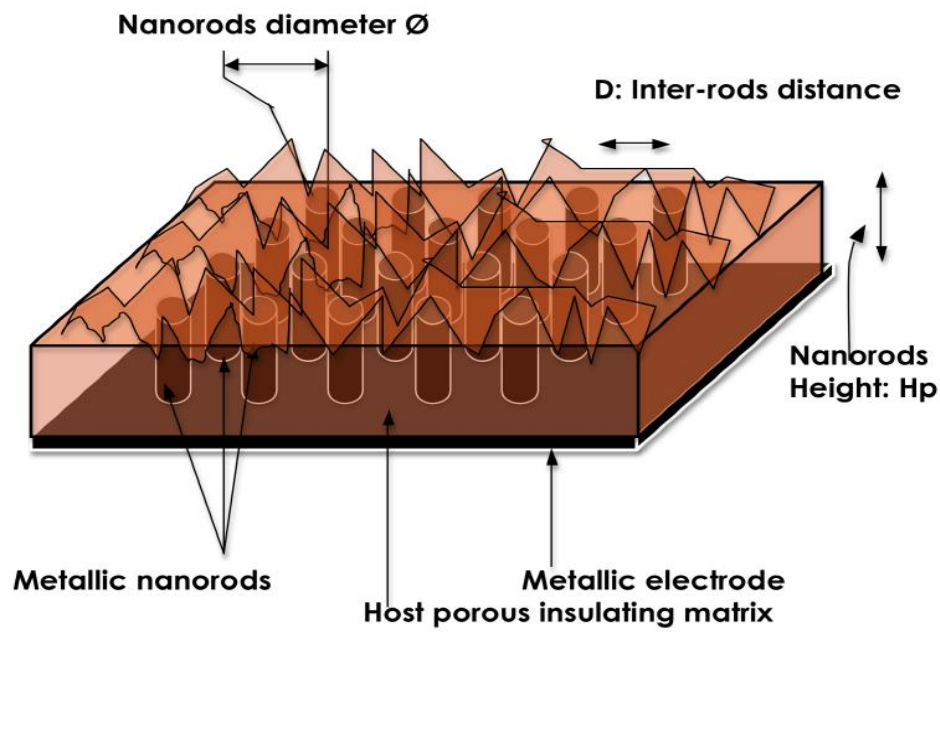

Figure 3.5: Schematic configuration of the laser surface structured selective solar absorber consisting of vertically oriented Co nanorods in porous Al_2O_3

The method is based on the formation of interference patterns, which are produced when two or more coherent laser beams are overlapped on the surface of a material. The only

requirement is the absorption ability of the material at wavelength of the incoming laser beam [3.15].

Micro-structuring characteristics like pattern period and pattern depth can be controlled by the laser parameters like wavelengths, pulse width, pulse number and the power. In direct structuring of metal substrates the periodical heat source produces the local heating of the metal through photo-thermal interaction at the interference maxima positions [3.17]. Different metallurgical effects such as melting, resolidification and phase formation are also happening in this point. These effects permit the texturing of the metallic surfaces, which can be exploited to produce structured solar-absorber.

Imprint structuring

In imprint (embossing) technology, a structured elastomeric mold is used to deform an active material deposited on a substrate. The active layer can be UV- or thermally curable material or a deformable material with high thixotropic characteristic. The elasticity and low surface energy of the mold allows it to be released easily. After thermal curing of embossed resist layer, a glassy layer is obtained, the structure is ready and the desired material can be deposited on it.

Thermal curing of imprint micro-structured inorganic sol-gel materials would lead to 70% shrinkage [3.15]. Therefore structure heights of only few nanometers are obtainable. The shrinkage rate of such materials can be reduced by adding organic components, like Polyethylene oxide.

3.7 REFERENCES

[3.1] F. Padera, UV/Vis Spectroscopy. (2013), PerkinElmer Inc. Shelton, CT USA.

[3.2] M. Rand, Spectrophotometric Thickness Measurement for Very Thin SiO_2 Films on Si, Journal of Applied Physics 41(1970) 2.

[3.3] W.L. Wolfe, G.J. Zissis, The infrared handbook, Environmental Research Institute of Michigan. (1989), Washington DC.

[3.4] C.E. Kennedy, Review of Mid- to High-Temperature Solar Selective Absorber Materials, NREL/TP-520-31267, National Renewable Energy Laboratory, Colorado, July 2002.

[3.5] K. Gelin, Preparation and Characterization of Sputter Deposited Spectrally Selective Solar Absorbers, Ph.D. Dissertation. Sweden: Uppsala University; (2004).

[3.6] T. Bostrom, Solution-Chemically derived spectrally selective solar absorbers. Ph.D. Dissertation. Sweden Uppsala: University; (2006).

[3.7] Z.Y. Nuru, Spectrally selective $Al_XO_Y/Pt/Al_XO_Y$ solar absorber coatings for high temperature solar-thermal applications. Ph.D. Dissertation, South Africa: University of Western Cape; (2014).

[3.8] O.S Heavens, Optical properties of thin solid films. (1991), New York: Dover Publications.

[3.9] F. Wooten, Absorption and Dispersion, in Optical Properties of Solids. (1972), New York: Academic Press, pp 42-55.

[3.10] S. Zhao, Spectrally Selective Solar Absorbing Coatings Prepared by dc Magnetron Sputtering. Ph.D. Dissertation, Sweden: Uppsala University; (2007).

[3.11] D.W. Lynch, W.R. Hunter, Optical constants of metal, in Handbook of Optical Constants of Solids. (1985), USA: Academic Press, Inc.

[3.12] O.S. Heavens, Thin Film Optics, in Optical Properties of Thin Solid Films. (1954), New York: Dover publications, Inc. 46-50.

[3.13] G. A. Niklasson, C.G. Granqvist, Optical properties and solar selectivity of co-evaporated $Co\text{-}Al_2O_3$ composite films. J. Appl. Phys. 55 (1984) 3382-3410.

[3.14] G.A. Niklasson, C.G. Granqvist, O. Hunderi, Effective Medium Models for the Optical Properties of Inhomogeneous Materials. Applied Optics 20 (1981) 26-30.

[3.15] M. Nejati, Cermet based solar selective absorbers; further selectivity improvement and developing new fabrication technique, Ph.D. Dissertation. University of Saarlandes; (2008).

[3.16] A.F. Lasagni, Advanced design of periodical structures by Laser Interference Metallurgy in the micro/nano scale on macroscopic areas. Saarland University, Saarbrücken (2006). 28Deut12.

[3.17] M. von Allmen, A. Blatter, Laser-Beam Interactions with Materials. 2nd ed. (1995), Berlin: Springer

CHAPTER FOUR

EXPERIMENTAL METHODS

In this thesis, we have designed femtosecond laser surface structured ferromagnetic Co and Ni nanorods in Al_2O_3 matrix selective solar absorber coating using electrochemical methods anodization and electrodeposition. This particular method was selected out of the other fabrication techniques used to prepare cermet- based spectrally selective solar absorbers namely:Physical and chemical vapor deposition (Evaporation, Sputtering), Electroplating, Anodization, Painting and Solution-based methods that were extensively discussed in Chapter 2. The coatings made by anodization have been found to be thermally stable so they can work at high temperature. Al_2O_3 based cermets coatings have been extensively investigated as specrally selective solar absorbers because of their excellent optical properties and thermal stabilities.

4.1 SAMPLE PREPARATION

High purity (99.997%) aluminium sheets with 0.5mm thickness from Sigma Aldrich were used as substrate. The sheets were cut into samples of size 2cm x 1cm using a cutting machine from the laboratory and then annealed under high vacuum at 500^{o}C for 3 hours.

To remove the dust and impurities, the aluminium substrates are degreased in acetone for a few seconds. After cleaning with the acetone the surface looks shiny and clear, cleaning of the sample contributes to better results without misleading impurity peaks and traces. The sample is held using a sample holder in order to avoid contact impurities and fingerprints from the hand. To remove the acetone the sample is then cleaned with methanol for few seconds and etched in potassium hydroxide before being thoroughly rinsed with deionized water.

4.2 PREPARATION SETUP

Anodization is usually conducted using an electroanalytical system under constant cell potential. A modern electroanalytical system for volammetric measurements consists of an electrochemical cell, a potentiostat, and a data acquisition system/computer, see Fig. 4.1. A potentiostat is an electronic device which uses a dc power source to apply an accurate and controlled potential, and monitors the current produced by allowing small currents to be drawn into the system without changing the voltage [4.1-4.2].

Figure 4.1: Electroanalytical System

The electrochemical cell where the electro chemical measurements are carried out consists of a working electrode (WE), counter electrode (CE) and electrolytic solution. The purpose of the electrolytic solution is to provide ions to the electrodes during oxidation and reduction.

The counter electrode also known as auxiliary electrode is an electrode which is used to close the current circuit in the electrochemical cell. It does not participate in the electrochemical reaction and it is ordinarily made of inert materials like graphite, gold, Pt, and glassy carbon.

In this case an electropolished aluminium foil (Al) serves as an anode and a platinum mesh (Pt.) as a counter-electrode (cathode). 0.5M oxalic acid was used as the electrolyte. Both the electrode and cathode are immersed into the electrolyte to form a complete circuit. The data acquisition system produces the resulting voltammogram, and the Autolab PGSTAT(Potentiostat/Galvanostat) 302N shown in Fig. 4.1 was used for anodizing and electrodeposition. In potentiostatic mode the PGSTAT will accurately control the potential of the CE against the WE while in galvanostatic mode the current flow between the WE and CE is controlled and continuously monitored.

4.3 ANODIZATION

The first step in the thesis work is to work on anodization. Anodizing is an electrolytic process which is used to increase the thickness of the oxide layer on the surface of metal. The process is called "anodizing" because the part to be anodized forms the anode of the circuit. The samples that have been cleaned and annealed are anodized for formation of nanopores on the aluminium film using oxalic acid for 2 hours, 4 hours, 7hours and 9 hours in an electrolytic cell as shown in Fig. 4.1.

A 10V DC power supply is used and the current is calculated to be 30mA, which is shown in the calculations below. The entire process is carried out at low temperature of 5^{o}C. A glass beaker that contains the electrolyte is placed on the holder and the sample is attached to the sample holder and then dipped into the solution until the marked area. The sample side that has to be anodized is placed facing the platinum cathode for better anodization. After this process, the sample is rinsed with de-ionized water very gently and then quick dried using dry air in the chamber.

The Chronoamperometry technique of the Autolab PGSTAT 302N that measures current against time was selected for steady growth of the nanorods.

During the anodization process, the pores nucleate randomly on the surface with a broad size distribution, for this research oxalic acid is used as electrolyte.

4.4 FACTORS AFFECTING THE GROWTH OF NANORODS

It is now accepted that the growth occurs exclusively at the pore basemetal/oxide interface, and oxide dissolution is uniformly distributed over the whole of the nanorods

One of the important factors that affect assembly of porous alumina is the applied potential. The interpore distance and the thickness of the barrier oxide layer are directly proportional to the applied potential. The type and concentration of the electrolyte for a given potential has to be selected properly to obtain self-ordered pore growth. All these factors are taken into consideration for formation of the pores [4.3-4.4].

4.4.1 Anodizing potential and Current density

The majority of experiments are performed under potentiostatic conditions, which involves the application of a constant potential and monitoring the anodization current. In contrast, galvanostatic growth has been less investigated; it seems to be more difficult to control the morphology of the anodic NTs under a galvanostatic regime [4.5]. The applied potential usually ranges from 5 to 30 V and 10 to 60 V in aqueous and organic electrolytes, respectively [4.6-4.7]. The applied potential determines the electric field strength across the oxide, thus affecting the migration of ions and ultimately the nanotube diameter. A linear relationship between the applied potential and the diameter of the NTs is generally observed up to 60 V [4.6]. A linear dependence relationship also exists between the thickness of the barrier layer at the base of the NTs and the applied potential. However there are also exceptions to this rule. For example, Yin et al. reported an inverse relationship between the potential and NTs diameter at potentials larger than 100 V and attributed their findings to the diffusion of water being the rate limiting step under such conditions. Similar observations were also reported by Su and Zhou, who found that the pore diameter of porous anodized nanostructures drops when the applied potential exceeds a critical value (generally above 60 V), which is deter-mined by the electrolyte and has an influence on the dissociation of water (and on the current density) and therefore on the porosity and the pore size of the anodic film. Clearly the anodizing potential and the modality by which it is applied (i.e. the potential) [4.6].

4.4.2 Electrolyte pH and concentration

The pH of the anodizing solution in this case the oxalic acid affects the ability of the electrolyte to dissolve the forming oxide, an increase in the acidic environment leads t higher oxide dissolution rates [4.8]. The concentration of the oxalic acid has to be kept low to minimize dissolution, but it also has to be at a level sufficient to ensure NR growth.

Ageing of an electrolyte is another factor into account which help to synthesize well defined NRs. When an anodizing solution is aged by resusing its electrical conductivity increases as a results of higher content built up from previous anodization cycles. A higher ion concentration translates into a lower rate of chemical dissolution; hence it is important in establishing the condition required for maximizing oxide growth.

4.4.3 Anodizing time

Identification of the optimal anodizing time for a given set of conditions (electrolyte, potential, fluorine concentration, etc.) is required to extend the maximum length of the NTs. When working in aqueous media, the conditions are far too aggressive to allow the NTs to grow any longer than a few mm [4.6]. Such a thickness is usually reached within minutes from the onset of the anodization process, however the anodizing time usually ranges from 30 min to 2 h in order to allow the structure to rearrange itself and increase the degree of self-order. In contrast, the growth process in organic electrolytes is much slower and dissolution phenomena are not as significant as in water, although conditions still need to be tuned for optimal growth. As a result, by extending the anodization time from several hrs up to a day, it is generally possible to obtain NRs over 100 mm long [4.6]. One of the issues associated with employing long anodizing times in an organic electrolyte is over-dissolution of the NRs in some areas. As discussed, when using an organic solution it is common to observe a porous layer on top of the NTs, which is a remnant of the initial barrier layer formed during the early stages of anodization [4.6]. The nanotubular layer develops under-neath and it is assumed that there are preferential paths for the organic electrolyte, hence over-dissolution is not homogenous over the entire NR structure.

4.4.4 Temperature

Temperature is another major factor to be considered. During the process of anodization, low temperature is maintained to prevent the oxide from being dissolved in the acidic solution and local heating at the bottom of the pores. Another reason to maintain the constant temperature is to monitor the speed of growth which is directly proportional to the temperature [4.6]. To maintain equilibrium growth and prevent excessive heat generation, the temperature is kept at room temperature for anodizing for small time intervals. In order to maintain low temperatures, a water bath is used for high-time-interval anodization. The entire experimental setup is placed inside the water bath and constant temperature is chosen for all the experimental setups in order to maintain the equilibrium growth. If the temperature is not maintained constant, the substrate melts away due to excessive heating [4.6].

4.5 BARRIER AND POROUS ALUMINA

The porous-type and barrier type alumina consists of two oxide layers, the inner and the outer oxide layer. The inner layer , adjacent to the oxide/metal interface consists of high-purity alumina, whereas the outer oxide layer consists of alumina with anions incorporated and is adjacent to the electrolyte/oxide interface. The applied voltage determines the thickness of the barrier layer though there are some changes in the electrolytes and the temperatures [4.9].

The anodization of Al thick film in an electrolyte helps in the formation of the structure consisting of an Al base, alumina barrier layer separating the Al from the nanoporous membrane and the nanoporous Al membrane. The three major parameters which characterize the structure of the porous alumina membrane are the pore diameter, pore spacing and barrier layer thickness [4.9]. The barrier layer is a solid alumina layer that separates the nanoporous membrane from the supporting Al foil.

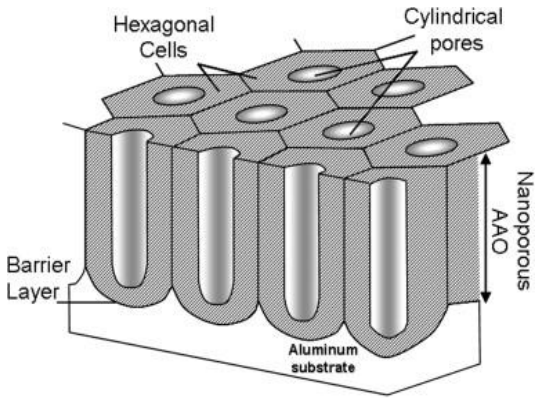

Figure 4.2: Barrier and Porous alumina

4.5.1 Pore Formation

During the anodization process, a solid alumina barrier layer is formed during the first few minutes. Non-uniform thickening of the barrier layer leads to the pore formation due to the current concentration. The pore size, pore spacing and barrier layer thickness are dependent upon the anodization voltage. During the oxidation process, volume expansion takes place that leads to mechanical stress and repulsive forces between neighbourhood pores, causing them to self organize in hexagonal pore arrays [4.8]. During the anodization of aluminium,

oxide is grown at the anode and the hydrogen gas is evolved at the cathode. The governing equation in this process is:

$$2Al + 3\,H_2O = Al_2O_3 + 3H_2 \qquad 4.1$$

4.5.2 Calculations

To find the current required in the anodization process, the current density is taken as constant throughout the experiments and the area to be anodized is calculated and the current is measured using the following equation:

$$I = J \times A \qquad 4.2$$

where I = required current

J = current density taken as constant throughout the experiment as 10 mA/cm^2

A= area to be anodized measured in cm^2

To calculate the area, the length and width of the sample is measured using a vernier calipers for accurate readings.

A = 1.2 cm x 2.5cm = 3.0 cm^2

J = 10 mA/cm^2

By substituting the values of J and A in Eqn. 4.2

I = 10 mA/cm^2 x 3.0 cm^2 = 30 mA

The final current required for the process is calculated as 30 mA.

4.5.3 Summary of the Anodization Process

1. The Al sheet is cut into samples of 1in x 1.5in length
2. The samples are then cleaned with acetone for few minutes to remove any oily or greasy substances that are formed on the surface.
3. The sample is rinsed with methanol to remove the acetone.
4. The sample is rinsed with de-ionized water.
5. Electropolishing: The sample is then electropolished in solution of 1:3 mixture of perchloric acid and ethanol for 10 sec using Pt. as the cathode and Al as anode.
6. The electropolished Al sheet is rinsed with D.I. water and dried.
7. Masking: the other side of the sample is masked using nail polish.

8. The sample (Al anode) is anodized using 0.5 M oxalic acid and Pt. cathode.
9. The same process is repeated by changing the time in periodic intervals (i.e., 2hrs, 4hrs, 7hrs, 9hrs,)

After the samples have been anodized in oxalic acid, they show the hexagonal pores which are detected using AFM and SEM, discussed in detail in the next chapter. To summarize, the pores are hexagonal in structure and the size and the diameter of the pores vary by the type of the acid and the anodization conditions. The next step is to fill these pores with cobalt. To fill the pores, the electrochemical deposition method is adapted and cyclic voltammetry is one of the electrochemical deposition methods.

4.6 ELECTRO-DEPOSITION OF MAGNETIC NANOWIRES

After anodization, the nanopores form on top of the Al with one end open and the other end attached to the Al substrate by a thin alumina barrier layer. The barrier layer underneath the pores blocks the dc current because of its large resistance of 10^{10} to 10^{12} cm.

The composition of the chemical bath was 0.6g nickel sulphate, 0.6g cobalt sulphate, 0.6g magnesium sulphate, 0.6g ammonium sulphate and 0.6g boric acid H_3BO_3 in 30ml distilled water. The ammonium sulphate improves the conductivity of the solution and the magnesium sulphate improves the coloring condition. An ac voltage of 15V (current density 20mA) was applied for 40min at room temperature. To reveal the characteristics of the Co-Ni nanocylinders- Al_2O_3 cermet coating created, high resolution observation of the microstructure was done using SEM(Scanning electron microscopy). The coating showed metallic cobalt and nickel nanorods of about 300nm long grown within the pores of the alumina, one in each pore starting to grow from the pore base.

4.6.1 Cyclic Voltammetry

Cyclic voltammetry is an electrochemical technique that measures current as a function of voltage, it can also be used for electroanalysis inorder to obtain information about an analyte. In addition to that, the information about the analyte is obtained by measuring the current as the potential is varied [4.10-4.11]. In the cyclic voltammetry method the voltage is swept between two values V_1 and V_2. (See Fig. 4.3). When the voltage reaches V_2 it sweeps back;

the scan is reversed and reaches the voltage V_1. This inversion can happen multiple times in the same experiment. The potential is applied between the working and the reference electrodes and the current is measured between the counter and the working electrode as shown in Fig. 4.3.

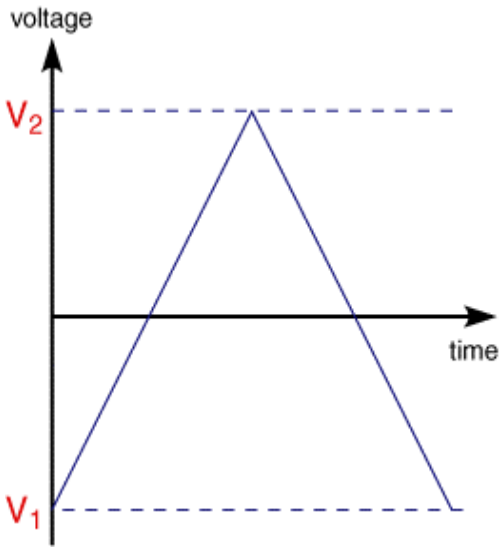

Figure 4.3: Cyclic Voltammetry Voltage Sweep

The graph is plotted between the current (I) and the potential (E). As shown in Figure 4.4, for any analyte which can be reduced or oxidized, the forward scan produces a peak. The current will increase till it reaches the reduction potential of the analyte. Once the point is reached it starts falling down. When the applied potential is reversed it will reoxidize the product from the intial reaction and produces the current of reverse polarity. Both the oxidation and the reduction peaks look alike but in different directions [4.10-4.11].

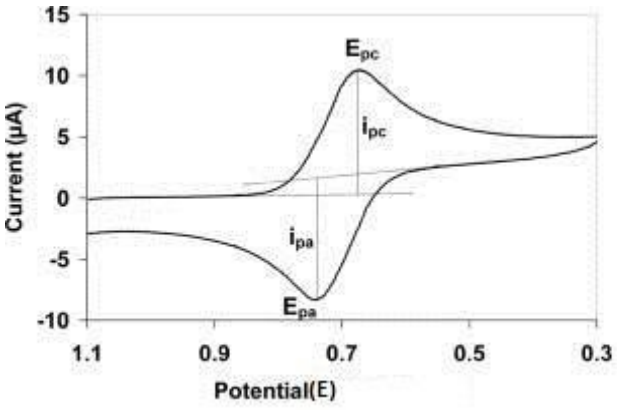

Figure 4.4: Typical Cyclic Voltammogram Instrumentation

The cyclic voltammetry system consists of an electrolysis cell, a potentiostat, data acquisition system (usually a laptop), and a current-to-voltage converter. The electrolysis cell consists of the working, reference, and counter electrodes as shown in Fig. 4.1. The potentiostat used in the present thesis work is the Autolab PGSTAT 302N. The device uses the power source to produce a potential and the smallest currents in the system can be drawn without changing the voltage. The electrolyte produces the required ions into the solution. The electrolyte used is the nickel and cobalt sulphate solution as the aim is to deposit Ni & Co into the substrate, i.e., anodized Al template. Therefore the working electrode is taken as the Al template into which the ferromagnetic Ni and Co are deposited. The current-to voltage converter measures the resulting current, and the data acquisition system produces the resulting voltammogram. Initially the CV is performed for four cycles on the anodized Al template. The sample is then tested under SEM to look for the presence of cobalt and nickel.

4.7 OPTICAL CHARACTERISATION

4.7.1 Spectrophotometers

The optical properties of the solar absorbers are often investigated using spectrophotometers which measure reflectance and transmittance. Spectrophotometry is a method to measure how much a chemical substance absorbs light by measuring the intensity of light as a beam of light For the solar selective coatings, the spectrometers are of interest especially when they cover the wavelength range of solar spectrum (0.3~2.5 μm) and the infrared region are of interest [4.12-4.15].

Depending on the type of measurements to be done, different kinds of spectrophotometers have been used. There are two major classes of devices: single beam and double beam. A double beam spectrophotometer compares the light intensity between two light paths, one path containing a reference sample and the other the test sample. A single-beam spectrophotometer measures the relative light intensity of the beam before and after a test sample is inserted [4.12-4.15]. Although comparison measurements from double-beam instruments are easier and more stable, single-beam instruments can have a larger dynamic range and are optically simpler and more compact. In this research work the Lambda 900 shown in Fig. 4.5 and Cary 5000 UV–vis–NIR spectrophotometer was used for the optical measurements [4.16]. Lambda 9 is a versatile spectrometer operating in the ultraviolet visible

(UV–vis) spectral ranges. In addition, the Lambda operates in the near infrared regions. The spectrometer features a double-beam, double monochromator, ratio recording optical system.

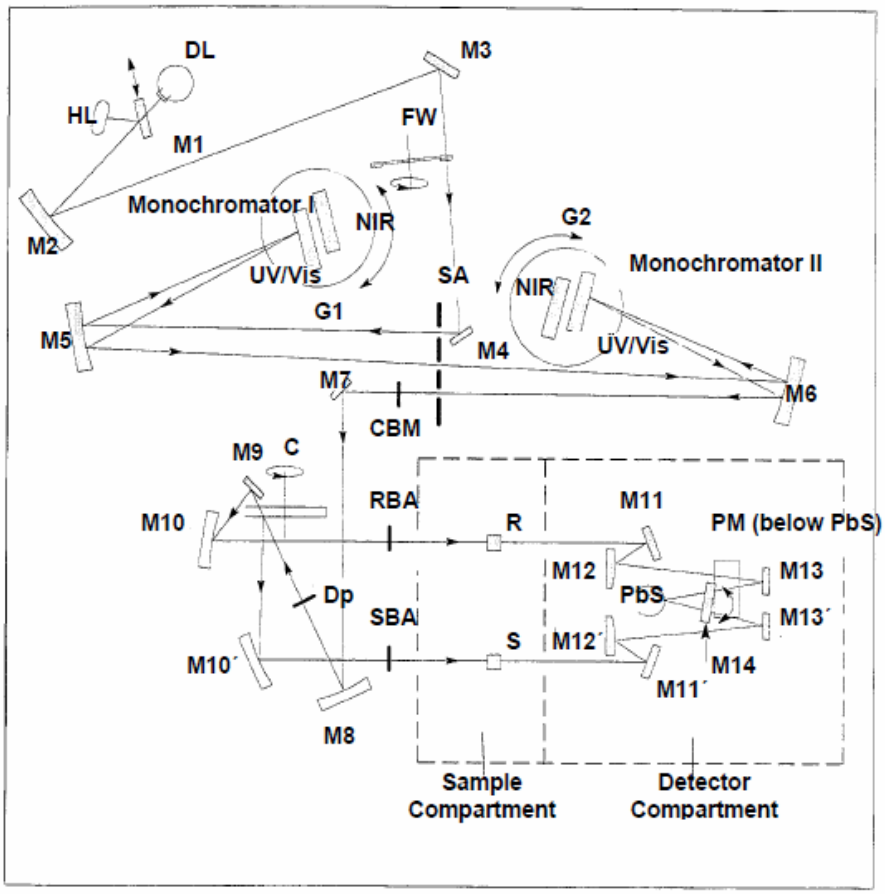

Figure 4.5: Schematic of Optical System Lambda 800/900 spectrometer [4.16].

Historically spectrophotometers use a monochromator containing a diffraction grating to produce the analytical spectrum. The grating can either be movable or fixed. If a single detector such as a photomultiplier tube or photodiode is used, the grating can be scanned stepwise so that the detector can measure the light intensity at each wavelength which will correspond to each step [4.12-4.15]. Arrays of detectors, such as charge coupled devices (CCD) or photodiode array (PDA) can also be used. In such systems, the grating is fixed and the intensity of each wavelength of light is measured by a different detector in the array. In addition, most modern mid-infrared spectrophotometers use a Fourier transform technique to acquire spectral information. The technique is called Fourier Transform Infrared Spectroscopy (FTIR) [4.12-4.15].

The FTIR spectrophotometer that is based on a system called a Michelson interferometer to collect a spectrum doesn't use a monochromator. The interferometer consists of a source, beam splitter, two mirrors, a laser and a detector [4.17-4.19]. The source emits polychromatic light beam that enter the beam splitter that divides the beam into two. One part is transmitted to a moving mirror that moves back and forth at a constant velocity which is timed according to very precise laser wavelength in the system. The second part is reflected to a fixed mirror. The polychromatic beams are reflected from the mirrors recombine creating interference pattern called an interferogram since some of the wavelengths recombine constructively and some destructively. [4.17-4.19], The interferogram goes from the beam splitter and interacts with the sample which absorbs some energy, the portion that is transmitted and finally reaches the detector. The detector signal is sent to a computer and the fast Fourier transform algorithim is used to process the interferogram, the result is displayed as a single beam spectrum.

Another common type of spectrometer is a dispersive instrument, which uses a white light source as one or more grating monochromators to create light with a certain wavelength and intensity [4.17, 4.19]. The source energy is sent through both a sample and a reference path then directed to a diffraction grating. The grating similar to a prism separates the wavelengths of light in the spectral range and directs each wavelength individually through a slit to the detector. The light that impinges on a surface is either reflected, transmitted or absorbed. A detector measures the intensity of the light one wavelength at a time with the slit monitoring the spectral bandwidth and the grating moving to select the wavelength being measured. The instrument scans over a wavelength interval and creates a spectrum of reflectance or transmittance data as a function of the wavelength relative a reference measurement [4.17, 4.19].

The measurements of total or diffuse reflectance and transmittance of scattering samples were performed with instruments equipped with integrating spheres. An integrating sphere is coated with a completely diffuse and highly reflecting surface. The detector measures the intensity from the homogeneously illuminated sphere wall, which is proportional to the radiation scattered in any direction from the sample. Normally the sphere is coated with diffuse barium sulphate or Teflon in the UV/Vis/NIR wavelength ranges and diffuse gold for infrared wavelengths.

4.8 NON-OPTICAL CHARACTERISATION

4.8.1 Scanning Electron Microscopy (SEM)

A Scanning Electron Microscope (SEM) is a powerful magnification tool that utilizes focused beams of electrons rather than light to form an image. SEM produces high-resolution, black and white, three-dimensional images that provide information on the topography, morphology and composition of a sample. An electron gun at the top of the microscope see Fig. 4.6 generates a beam of energetic electrons by heating a metallic filament. The electrons follow a vertical path down the column of the microscope and onto a series of electromagnetic lenses.

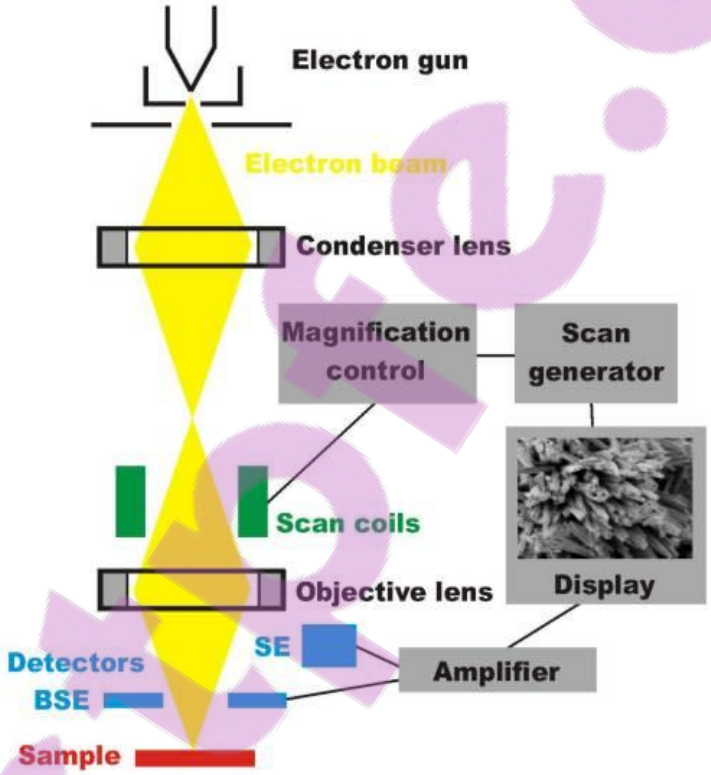

Figure 4.6: Schematic representation of Scanning Electron Microscope

These lenses are tubes, wrapped in coil and referred to as solenoids; they focus and direct the beam down towards the sample. The interaction between the incident electrons and the surface of the sample is determined by the acceleration rate of incident electrons, which carry significant amounts of kinetic energy before getting focused onto the sample. When the incident electron beam hits the sample, energetic electrons (backscattered or secondary) are released from the surface of the sample. Detectors collect these electrons and convert them to

a signal that is sent to a monitor producing an image, the scatter patterns made by the electron-sample interaction yields information on size, shape, texture and composition of the sample. Backscatter electrons are incidental electrons reflected backwards; their images provide composition data related to element and compound detection. Diffracted backscatter electrons determine crystalline structures as well as the orientation of minerals and micro-fabrics. X-rays, emitted from beneath the sample surface, can provide element and mineral information. The advantages of using SEM include higher magnification (up to 10 nm) a greater depth of view, higher-resolution and, ultimately, a more detailed surface picture which makes SEM one of the most heavily used instruments, invaluable in a variety of science, research and industry applications. The SEM investigations for the laser surface structured Co nanorods in alumina cermet were obtained by a Nova NanoSEM 230 scanning electron microscope.

4.8.2. Energy Dispersive X-ray spectroscopy (EDS)

EDS is an analytical technique used for the elemental analysis of a sample. Its characterisation capabilities are based on the fact that each element has a unique atomic structure that allows unique set of peaks on its X-ray emission spectrum [4.20]. A high energy beam of charged particles such as electrons or Xrays is focused into the sample being studied the incident beam excites electrons from different shells and other electrons from higher energy shells fill the hole created the difference between the energy shells is released in form of X-rays. The number and energy of the emitted X-rays are measured by the EDS, the characteristic X-ray lines these are of the difference in energy between shells and the atomic structure of the emitting element. SEMS often have a microprobe for EDS and in this study the same SEM system was used for EDX analysis [4.20].

4.8.3 X-Ray Diffraction

X-ray diffraction technique is a versatile analytical technique and one of the best non-destructive techniques for the analysis of crystals to identify the atomic and molecular structure. They determine the various chemical, physical and crystallographic properties of materials and thin films [4.21].

In a single-crystal X-ray diffraction measurement a crystal is mounted on a goniometer that is used to position the crystal at different rotations, this device comprises of two independent drives that provide accurate and precise motion of the sample stage and detector [4.22]. When

the surface of the crystals is hit with a finely focused monochromatic beam (fixed wavelength) of X-rays at certain incident angles, the wavelengths of the scattered X-rays interfere constructively and the reflected X-rays produced have diffraction pattern of regularly spaced spots known as reflections. For the interference to occur it must satisfy the Braggs law; only then will the diffracted beam leave the crystal with the same angle as the incident ray [4.23]. The scattering is elastic and the scattered X-rays have the same wavelength as the incoming X-ray.

Bragg's Law

XRD uses the principle of Bragg's law which was explained by physicists Sir W.H. Bragg and his son Sir W.L. Bragg in 1913. It uses the property of crystal lattices to diffract monochromatic light into many specific directions. This causes the interferences of the waves scattered at the successive planes, which are defined by Bragg's equation as shown in Fig. 4.7 [4.24]

$$n\lambda = 2d \sin\theta \quad (\mathrm{n} = 1,2,3,4 \ldots .) \qquad 4.3$$

where λ is the wavelength of the incident x-ray

n is the order of a reflection

d is the distance between parallel lattice planes

θ is the angle between the incident beam and a lattice plane, known as Bragg angle

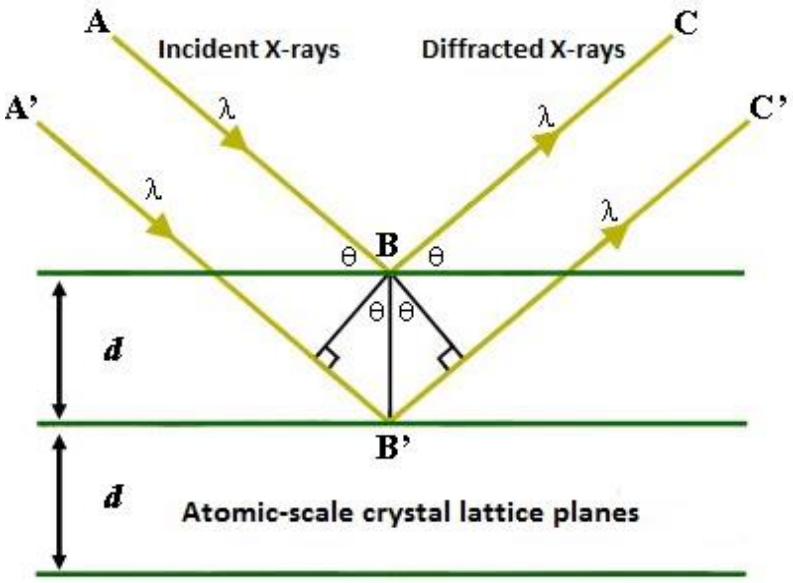

Figure 4.7: Illustration of Bragg's Law

When the pathlength in the crystal $(2d \sin\theta)$ is a multiple of the wavelength, constructive intereference occurs and diffracted intensity is obtained. In general the d-spacing is a function of the lattice parameters (a, b, c) and angles (α, β, γ) defining the unit cell, and the Miller indices (*h, k, l*) denoting a particular reflection. The geometry of the crystal lattice determines the positions of the peaks in an X-ray diffraction pattern [4.22]. As the material increases in symmetry, the peaks in its diffraction pattern get fewer. The diffracted intensities associated with those peaks are determined by the type and arrangement of the atoms within the crystal lattice.

The two-dimensional images taken at different rotations are converted into a three-dimensional model of the density of electrons with the crystal using the mathematical method of Fourier transform combined with chemical data known for the sample. Many materials such as salts, metals, minerals, semiconductors as well as various inorganic, organic and biological molecules can form crystals. X-ray crystallography has been fundamental in the development of many scientific fields. In its first decades of use, this method determined the size of atoms, the lengths and types of chemical bonds, revealed the structure and function of many biological molecules including vitamins, drugs, proteins and DNA. X-ray crystallography is still the chief method for characterizing the atomic structure of new materials and in discerning materials that appear similar by other experiments.

4.8.4 Atomic Force Microscopy (AFM)

Atomic force microscoy(AFM) is a very high resolution technique for studying the surface morphology at nanoscale. In this study the surface roughness influences light trapping ability of the selective nanomaterial therefore it needs to be correctly analysed. The information is gathered by "feeling" the surface with a mechanical probe cantilever with a sharp tip (probe) that is used to scan the specimen surface [4.11]. Piezoelectric elements that facilitate tiny but accurate and precise movements on (electronic) command enable the very precise scanning done while monitoring the change in cantilever deflection with a split photodiode detector.

The cantilever is typically silicon or silicon nitride with a tip radius curvature on the order of nanometers. When the tip is brought into proximity of a sample surface, forces between the tip and the sample lead to a deflection of the cantilever [4.11]. If the tip was scanned at a constant height, a risk would exist that the tip collides with the surface causing damage. Hence, in most cases a feedback mechanism is employed to adjust the tip-to-sample distance

to maintain a constant force between the tip and the sample .Digital Instrument Dimension 3000 AFM with a resolution in accompany with Nanoscope V720 software was used to study the surface roughness.

4.8.5 Rutherford Backscattering Spectrometry (RBS)

Backscattering spectrometry is a method that provides accurate depth information about the stoichiometry, elemental area density and impurity distributions in the near surface region of bulk materials and in thin films. RBS is based on collisions between an energetic incident ion and a target nucleus [4.25]. If the interaction between the incident particle and target nuclei can be described by Coulombic forces, the scattering is defined as Rutherford, which derives its name from Lord Ernst Rutherford, who first presented the concept of atoms having nuclei. Due to a large number of interactions, it's important to find out how much energy will be transferred in a collision or what the scattering angle will be. The differential cross section is the fundamental parameter that is developed, and it gives the measure of the transferring energy T in the range to a target atom or the probability into the some angle between θ_c and $\theta_c + d\theta_c$. The differential cross section has units of area and when integrated over all angles is the total cross section [4.25-4.27].

$$\frac{d\sigma(\theta_c)}{d\Omega} = \frac{b}{\sin\theta_c}\left|\frac{\mathrm{db}}{\mathrm{d}\theta_c}\right| \qquad 4.4$$

Consider a condition where the interaction between colliding particles is purely Coulombic, as in the case for Rutherford scattering. If the projectile is described by mass and atomic number M_1 and Z_1 and the target nucleus described by mass and atomic number M_2 and Z_2. The interatomic potential for Coulomb interaction is given by

$$\mathrm{V(r)} = \frac{Z_1 Z_2 e^2}{\mathrm{r}} \qquad 4.5$$

Where r is the distance of separation between the two nuclei. Consider the following substitutions

$$\mathrm{u} = \frac{1}{\mathrm{r}} and\ \alpha = Z_1 Z_2 e^2 \qquad 4.6$$

$$\mathrm{V(u)} = \alpha\,\mathrm{u} \qquad 4.7$$

Using the classical scattering integral that gives the angular trajectory information for two-body central force scattering given in

$$\theta_c = \pi - 2\mathrm{b} \int_{\mathrm{r_{min}}}^{\infty} \frac{dr}{r^2 \left[1 - \frac{V(r)}{E_c} - \left(\frac{b}{r}\right)^2\right]} \qquad 4.8$$

The angular scattering equation becomes

$$\theta_c = \pi - 2 \int_{0}^{1/\mathrm{r_{min}}} \frac{dr}{\left[\frac{1}{\mathrm{b}^2} - \frac{\alpha \mathrm{u}}{E_c \mathrm{b}^2} - u^2\right]^{1/2}} \qquad 4.9$$

Equation (4.8) can be integrated exactly by using the integral solution

$$\int \frac{d\mathrm{x}}{(\mathrm{a} + \mathrm{cx} + \mathrm{dx}^2)^{1/2}} = \frac{-1}{(-\mathrm{d})^{1/2}} \sin^{-1}\left(\frac{\mathrm{c} + 2\mathrm{dx}}{(\mathrm{q})^{1/2}}\right) \qquad 4.10$$

By substitutions, the solution to Eqn 4.8 is given by

$$\theta_c = \pi - 2\left[\sin^{-1}\left(\frac{-\left(\mathrm{bu} + \frac{\alpha}{2E_c \mathrm{b}}\right)\alpha \mathrm{u}}{\left(1 + \frac{\alpha^2}{4{E_c}^2 \mathrm{b}^2}\right)^{1/2}}\right)\right]_0^{1/\mathrm{r_{min}}} \qquad 4.11$$

Using the following expression from angular momentum that relates the distance of closest approach, $\mathrm{r_{min}}$, to the ion energy, E_c, and the form of the inter-atomic potential $V(\mathrm{r_{min}})$ [4.28]

$$0 = 1 - \frac{V(\mathrm{r_{min}})}{E_c} - \frac{\mathrm{b}^2}{\mathrm{r_{min}^2}} \qquad 4.12$$

Using change of variables defined by Equations (4.6) and (4.7), and solving (4.12) using the quadratic equation, we can express b in terms of θ_c to obtain Equation (4.13) below:

$$\sin\left(\frac{\theta_c - \pi}{2} \pm \frac{\pi}{2}\right)\theta_c = \pi - 2\sin^{-1}\left(\frac{-\left(\mathrm{bu} + \frac{\alpha}{2E_c\mathrm{b}}\right)\alpha\mathrm{u}}{\left(1 + \frac{\alpha^2}{4{E_c}^2\mathrm{b}^2}\right)^{1/2}}\right) \quad 4.13$$

The trigomometric representation of Eqn. 4.13, allows us to construct a relationship between the impact parameter b and the scattering angle θ_c. Using the differential scattering cross section Eqn. (4.4) for scattering into a solid angle, Rutherford differential cross section is obtained as Eqn. (4.14) given below:

$$\frac{d\sigma(\theta_c)}{d\theta_c} = \frac{d\sigma(\theta_c)}{\mathrm{d}\Omega}\frac{\mathrm{d}\Omega}{\mathrm{d}\theta_c} = 2\pi\left(\frac{\alpha}{2E_c}\right)^2 \frac{\cos(\theta_c/2)}{\sin^3(\theta_c/2)} \quad 4.14$$

Advantages of the RBS are that the analysis depths using He ions are typically a few thousand nanometers, and depth profile information is obtained in a non-destructive manner. The results obtained do not require the use of a standard and are insensitive to the sample chemical bonding. In addition it is a quick and easy experiment to perform typically with data acquisition times of few tens of minutes [4.29-4.30].

The drawback of RBS is the low sensitivity for light elements, which often requires the combination of other nuclear bases methods like nuclear reation analysis (NRA) or elastic recoil detection analysis (ERDA). RBS does not provide any chemical bonding information which we can get from XPS. However, conventional RBS systems cannot analyse ultrathin films since the depth resolution is only about 10 nm using surface barrier detector [4.29-4.30].

4.8.6 Raman spectroscopy

Raman spectroscopy is the measurement of the wavelength and intensity of inelastically scattered light from molecules used to provide information on a sample's chemical composition and molecular structure [4.31]. This spectroscopic technique used in condensed matter physics and chemistry to study vibrational, rotational, other low-frequency modes in a system and optical quasiparticles in matter.

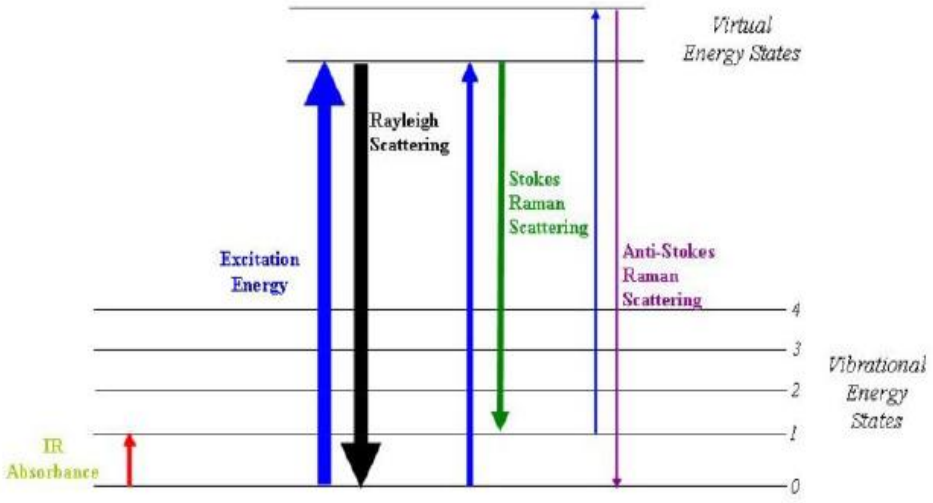

Figure 4.8: The Raman Effect [4.31].

The Raman process involves inelastic scattering of a photon when it is incident on the electrons in a molecule and the scattered light has been weakly modulated by the characteristic frequencies of the molecule. Raman will measure the difference between the wavelengths of the incident radiation and the scattered radiation [4.31]. When in elastically-scattered, the photon loses some of its energy to the molecule by the Stokes process as indicated in Fig.4.8. It can then be experimentally detected as a lower-energy scattered photon. The photon can also gain energy from the molecule by the anti-Stokes process also shown in Fig. 4.8. Raman selection rules are based on the polarizability of the molecule or the "deformability" of a bond or a molecule in response to an applied electric field. To be Raman active a molecule must have anisotropic polarizability.

Every molecule has vibrational modes (states). Vibrational modes are quantized and will absorb photons of a specific energy (IR spectroscopy), or steal that same amount of energy from an incident photon and change the wavelength of the scattered photon (Raman spectroscopy).

To make a Raman measurement, we will need the components below illustrated in Fig. 4.9.

- **Monochromatic light source** typically a laser. This implies potential of laser damage because some samples very sensitive to laser energy.
- **Sampling optics**. A way of focusing the laser onto the sample and then collecting the Raman scatter.

- **Rejection filter**. A way of removing the scattered light that is not shifted (changed in colour).
- **Spectrometer and detector**. This is often a single grating spectrometer and CCD detector.

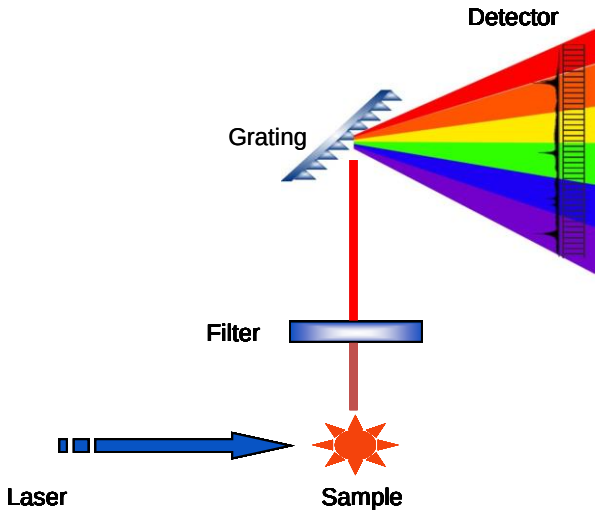

Figure 4.9 Raman Measurement

- Most of the identifying signatures are in the 500-1500 cm^{-1} range
- Carbonyl group in the 1600-1900cm^{-1} range is good at differentiating similar chemicals.
- With a good filter, Raman can show lattice vibrational modes down at 200cm^{-1} which describes the physical structure of the sample [4.31].

4.9 DIRECT LASER STRUCTURING

A laser consists of a gain medium, a mechanism to energize it, and something to provide optical feedback. The gain medium is a material with properties to amplify light by way of stimulated emission. Stimulated emission is the process by which an incoming photon of a specific frequency can interact with an excited atomic electron (or other excited molecular state), causing it to drop to a lower energy level. The liberated energy transfers to the electromagnetic field, creating a new photon with identical phase, frequency, polarization and

direction of travel as the photons of the incident wave. Light of a specific wavelength that passes through the gain medium is amplified (increases in power) [4.20, 4.32]. For this to occur the gain medium is supplied with energy in form of an electric current or as light at a different wavelength in a process called pumping.

A laser differs from other sources of light in that it emits light coherently, that is the waves have constant phase difference and the same frequency. The property of coherence is the basis for commercial applications of the laser; lasers are used in cutting and welding materials, optical disk drives, laser printers, barcode scanners, laser surgery, skin treatments, fiber-optic, free-space optical communication. Spatial coherence describes the correlation between waves at different points in space, it allows a laser to be focused to a tight spot, enabling applications such as laser cutting and lithography [4.20, 4.32]. Temporal coherence describes the correlation between waves observed at different moments in time. high temporal coherence allows a laser to emit light with a very narrow spectrum, i.e., can emit a single color of light. This property can be used to produce pulses of light as short as a femtosecond.

The femtosecond laser is an ultrafast laser emitting extremely short electromagnetic pulses with a duration well below one picosecond (1ps = 10^{-12}s), that is in the domain of femtosecond (fs). In optics the generation of such short pulses is achieved with the technique of mode locking. A mode-locked laser is capable of emitting extremely short pulses on the order of picoseconds or femtoseconds. These pulses will repeat at the round trip time, that is the time it takes light to complete one round trip between the mirrors comprising the resonator [4.20, 4.32]. Due to the Fourier limit (also known as the energy-time uncertainity), a pulse of such short temporal length has a spectrum spread over a considerable bandwidth. Such a gain medium must have a gain bandwidth sufficiently broad to amplify those frequencies. An example of a suitable material is titanium-doped artificially grown sapphire(Ti:sapphire) which has a very wide gain bandwidth and can thus produce pulses of only a few femtoseconds duration.

In this work, a femtosecond fiber laser pulsing at the fundamental wavelength of 1064 nm, repetition rate of 78.5 MHz and pulse duration of 290 fs was used to surface structure the thin films. The FP1064-fs series is a high power ultrafast fiber laser which utilizes efficient pulse compression to provide high quality optical pulses of less than 300fs. Designed for the most

demanding scientific and industrial applications, the laser delivers high average powers while maintaining exceptional beam quality and femtosecond pulse duration. The FemtoPower FP1064 is flexible; Laser delivery is from a passively-cooled compact remote head which includes the pulse compressor, beam delivery optics, optical isolation and optional frequency conversion.

The Co-alumina samples were finally mounted on an X-Y motorized stage programmed to execute an X-Y translations in a form of parallel lines while the laser was irradiating perpendicularly the sample with a waist of about ~100 μm above the sample in order to avoid excessive ablation of the coating but sufficiently enough to structure the surface. The spot diameter on the sample at $1/e^2$ intensity was measured with a camera (Primes, model Micro Spot Monitor) and could be tuned with a variable beam expander.

4.10 REFERENCES

[4.1] A. Bard, L. Faullkner, Electrochemical Methods-Fundamental and Applications. (2000) 2nd Edition, John Wiley and Sons.

[4.2] Metrohm Autolab (2011), Instruction manual.

[4.3] D.J. Sellmyer, M. Zheng, R. Skomski, Magnetism of Fe, Co and Ni nanowires in self-assembled arrays. Journal of Physics: Condensed Matter 13 (2001) R433-R460.

[4.4] G.D. Sulka, A. Eftekhari, Highly Ordered Anodic Porous Alumina Formation by Self-Organized Anodizing (2010).

[4.5] L.V. Taveira, J.M. Macak, K. Sirotna, L.F.P. Dick, P. Schmuki, Journal of Electrochemical Society 153 (2006) B137-B143.

[4.6] D. Regonini, A. Satka, D. Allsopp, A. Jaroenworaluck, R. Stevens, C.R. Bowen, Journal of Nanoscience and Nanotechnology (2009) 4410-4416.

[4.7] J.M. Macak, H. Tsuchiya, A. Ghicov, K. Yasuda, R. Hahn, S. Bauer, P. Schmuki, Current Opinion Solid State Material Science 11 (2007) 3-18.

[4.8] J.M. Macak, H. Tsuchiya, P. Schmuki, Angewandte Chemie International 14 (2005) 2100-2102.

[4.9] S.K Koney, Electrochemical Fabrication of ZnO Nanowires in Anodized Aluminum Template Using Cyclic Voltammetry. MSc. Dissertation. Illinoius: Northern Illinoius University; (2000).

[4.10] G.F.V. Voort, Chemical and Electrolytic Polishing, ASM Handbook Metallography and Microstructures. ASM International 9 (2004) 281-293.

[4.11] K.M. Lang, D.A. Hite, R.W. Simmonds, R. McDermott, D.P. Pappas, J.M. Martinis, Conducting atomic-force microscopy for nanoscale tunnel barrier characterization. Review of Scientific Instruments 75 (2004) 2726–2731.

[4.12] ASTM, Practice for Describing and Measuring Performance of UV/VIS/near-IR Spectrophotometers. ASTM E 275 (1989), Philadelphia.

[4.13] F. Grum, R.J. Becherer, Radiometry in Optical Radiation Measurements vol . 1. Academic, NY, 115 (1979).

[4.14] J.J. Hsia, National Scales of Spectrometry in the U.S., ed. C. Burgess and K.D. Mielenz. (1987), Amsterdam: Advances in Standards and Methodology in Spectrophotometry, Elsevier.

[4.15] J.M. Palmer, The measurement of transmission, absorption, emission and reflection. Chapter 25. University of Arizona.

[4.16] Lambda 800/900 User's Guide. (2003), USA: PerkinElmer Instruments LLC.

[4.17] K. Gelin, Preparation and Characterization of Sputter Deposited Spectrally Selective Solar Absorbers, Ph.D. Dissertation. Sweden: Uppsala University; (2004).

[4.18] T. Tesfamichael, Characterisation of Selective Solar Absorbers. Experimental and Theoretical Modeling. Ph.D. Dissertation. Sweden: Uppsala University; (2000).

[4.19] ThermoNicolet. Theory of Infrared Spectroscopy Instrumentation, www.thermo.com/nicolet.

[4.20] M. Nejati, Cermet based solar selective absorbers; further selectivity improvement and developing new fabrication technique, Ph.D. Dissertation. University of Saarlandes; (2008).

[4.21] B.E. Warren, X-ray Diffraction, Chapter 4. (1990), General Publishing Company.

[4.22] J. Formica, X-Ray Diffraction, Chpt. 8: Handbook of Instrumental Techniques for Analytical Chemistry. (1997), New Jersey: Prentice-Hall, Inc.

[4.23] G.N. Eby, Principles of Environmental Geochemistry.(2004), Brooks/Cole-Thomson Learning, 212-214.

[4.24] W.L. Bragg, The Diffraction of Short Electromagnetic Waves by a Crystal. (1913), Proceedings of the Cambridge Philosophical Society 17: 43.

[4.25] M. Nastasi, J.W. Mayer, Y. Wang, Ion Beam Analysis: Fundamentals and Applications. (2015), Boca Raton: Taylor & Francis Group, CRC Press. 28Deut12.

[4.26] M. Bozoian, Handbook of modern ion beam analysis. 2nd ed ed. Y. Wang & M. Nastasi. (2009), Warrendale PA: Materials Research Society.

[4.27] W.-K. Chu, J.W. Mayer, M.-A Nicolet, Backscattering spectrometry, Chap. 2. (1978), New York: Academic Press.

[4.28] M. Nastasi, J.W. Mayer, J. Hirvonen, Ion–solid interactions: Fundamentals and applications. (1996), Cambridge: Cambridge University Press.

[4.29] A. Hallén, Brief introduction to Rutherford Backscattering Spectrometry. (2012).

[4.30] M. Mayer, Rutherford Backscattering Spectrometry (RBS). (2003), Garching, Germany: Max-Planck-Institut f¨urPlasmaphysik, EURATOM Association.

[4.31] K. Kaviyarasu, Basic Principles of Raman Spectroscopy and its Applications. (2016), iThemba LABS: Capetown.

[4.32] A. E. Siegman Lasers. (1986), University Science Books.

CHAPTER FIVE

RESULTS AND DISCUSSIONS

The results presented in this chapter include optical measurements, microstructural and compositional analysis of the optimized femtosecond laser surface structured Co nanocylinders-Al_2O_3 cermet and optimized Co-Ni nanocylinders-Al_2O_3 cermet. The focus was on characterising the structural and optical performance of the optimized single and double ferromagnetic metal nanocermets and investigating the effect of the laser surface nanostructuring on its performance as a selective solar absorber. While their structural and chemical properties were investigated by X-ray diffraction (XRD), scanning electron microscopy (SEM), energy dispersive spectrometry (EDS), Raman spectroscopy and atomic force microscopy (AFM), their optical characteristics were investigated by total reflectance and infrared emissivity measurements done using the UV-VIS-NIR spectrophotometer and emissometer respectively. This chapter also reports the effect of annealing on the structural and optical properties of the laser surface structured Co nanocylinders-Al_2O_3 cermet solar absorber coating annealed in air for 2h at different temperatures.

5.1 STRUCTURAL CHARACTERISATION OF TUBULAR COBALT NANOCOMPOSITES

5.1.1 Scanning electron microscopy of the nanocomposites

The SEM micrograph below Fig. 5.1a shows the top view (basal plan) of the aluminium substrate prior the anodization process. The surface has been cleaned with acetone and methanol to remove any impurities; it is generally shiny, clear and slightly rough. The electropolishing process causes the surface to be less rough; it removes the grooves due to the mechanical procedure used in the fabrication of the commercial aluminium sheets [5.1-5.3].

Different anodizing conditions yield different pore diameters, wire lengths and centre-to-centre spacings. For example anodizing Al in 15% sulphuric acid at 10V dc yields pores having a diameter of about 8nm and an interval spacing increases to about 70nm and 110nm respectively. However under specific conditions, highly ordered hexagonal pore arrays are produced. First, it was found that the pre-annealing of Al substrate before anodization is a necessary goal to achieve this step. The Al grain size is 100 to 200μm after annealing at

500°C in nitrogen or high vacuum for 3 hours. Second a two-step anodization process is employed. The Al is first anodized in 3% oxalic acid at 40V for 15minutes, resulting in a 'textured' surface. Then the formed oxide layer is removed by wet chemical etching in a mixed solution of 0.2M chromic acid and 0.4M phosphoric at 60°C. Subsequently, the sample is re-anodized for a longer time (0.5 to 12h) using the same parameters as in the first step.

Fig. 5.1b shows the SEM image of the porous alumina host matrix that was anodized by two steps at 10V DC in 0.3M oxalic acid at around 0-4°C. The pores on the surface can be seen and their pattern seems more regular than that got from the porous alumina host matrix designed by a single step anodization process at the same conditions for 7hrs. The average diameter of the pores is ~17nm, it was found that the lower the temperature the more regular the pore array. The activity of the H ion at the pore bases during anodization increases with the temperature.

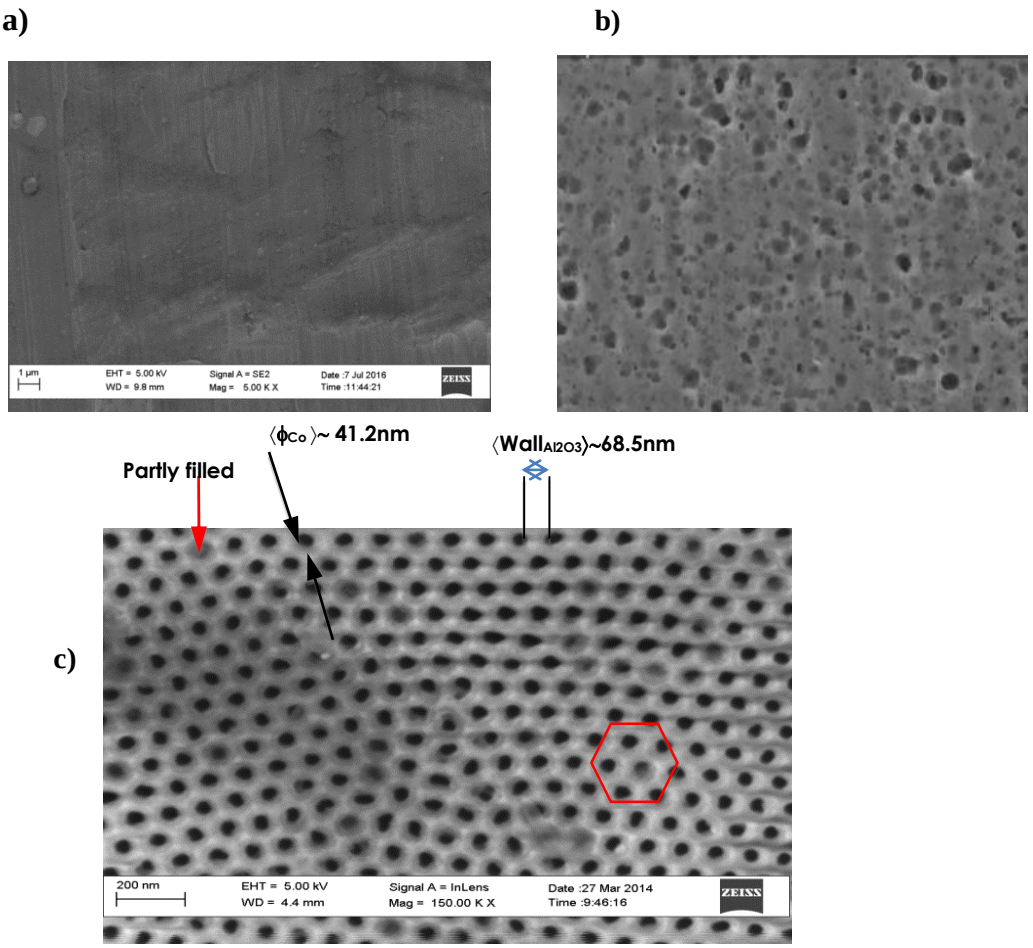

Figure 5.1: Scanning Electron Microscopy of (a) Aluminium substrate prior the anodization process, (b) Alumina host matrix designed at 10V, (c) Co nanocylinders-Al_2O_3 cermet designed at 30V

Pores opening towards the surface have been attributed to the chemical dissolution of the pore walls by the electrolyte during anodization. This result also indicates that the pore density of the alumina film increases at lower operation voltage [5.1-5.3].

This result indicates that the standard regular pore array of hexagonal pattern is obtained under higher voltage. The pore size of the anodic porous alumina is proportional to the operation voltage [5.1-5.3], the lower voltage of 10V is used for getting smaller sized pores. The morphology of the pores has also been improved by two-step anodization process. It is essential to note that the temperature and operation voltage are two of the most important factors in the process of fabrication of nanoporous alumina host matrix [5.1-5.3].
The surface morphology of the coatings affects the solar absorptance of the coating. The hexagonal like structure facilitates trapping of radiation so that the solar energy is absorbed by the black cermet to a greater extent.

5.1.2 AFM analysis the Laser surface structured Co-Al_2O_3 cermet.

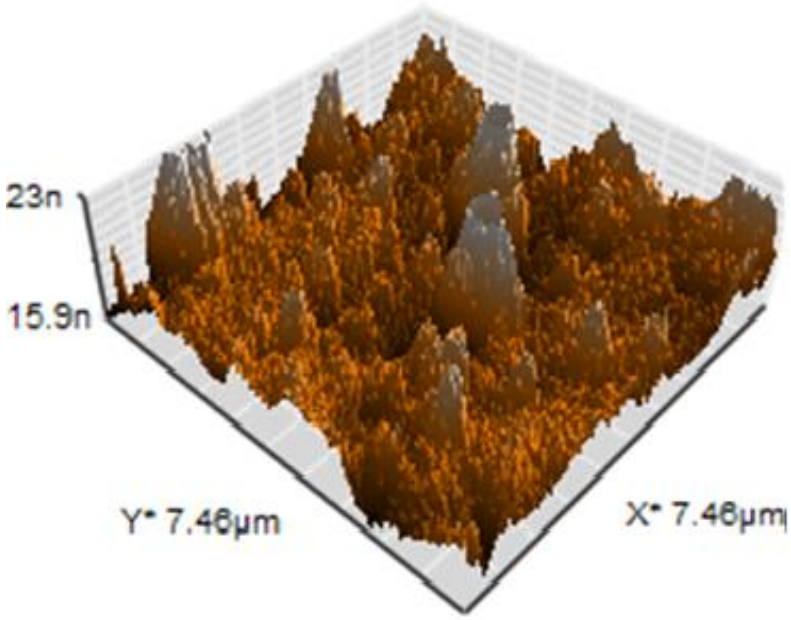

Figure 5.2: Three dimensional AFM topographic image of the optimized Co nanocylinders-Al_2O_3 cermet following the femtosecond laser surface structuring.

For investigation of the effect of laser surface texturing on surface morphology of the Co nanocylinders-Al_2O_3 cermet, AFM surface analysis was carried out and the micro-scans are

shown in Fig. 5.4. The surface exhibits significant roughness the root mean square of the surface roughness is about $\langle \sigma_{rms} \rangle$ ~38.9nm nearly 7 times more than the non-laser irradiated samples. This high surface roughness is can be explained by the highly ordered hexagonal structure of the Co-Al_2O_3 cermet and the femtosecond laser surface structuring.

More precisely, the laser surface texturing induces the formation of irregular conical like-shaped islands with an average roughness height of~ 41.7nm equivalent to the average root mean square of the surface roughness itself. The marked increase in roughness aspect ratio leds to higher selectivity. The irregular conical like shaped islands of the roughened surface trap light by multiple reflection and partial absorptions after each light-surface geometric interaction. In addition, the rough interface creates an increase in refractive index and lower surface reflection causing more light to enter into the active selective absorber layer.

This columnar laser induced surface structure could be due to a fast melting of Co and its partial diffusion out of the pores giving impression that the Co grows slightly out of the pores of the Al_2O_3 host matrix pores. This hypothesis is plausible in view of the refractory aspect of the Al_2O_3 host matrix and the relatively low melting temperature of Co. Furthermore, this hypothesis seems in agreement with the Electron Dispersion Spectroscopy (EDS) studies.

5.2 XRD OF TUBULAR COBALT NANOCOMPOSITES

5.2.1 X-ray diffraction of the Laser surface structured Co-Al_2O_3 cermet.

The result presented here has been published in MATPR721, Materials Today: Proceedings 2 (2015), pp. 4028-4037. Co diffraction peaks corresponding to reticular orientations of (100), (101) and (110) are observed. All observed Al and Co diffraction peaks coincide with those given within the Joint Committee on Powder Diffraction Standards (JCPDS) cards 00-004-0787 and 00-005-0727 of Al and Co structures respectively [5.4-5.5]. More precisely, the Bragg peaks are attributed to the face-centered cubic Al structure (space group Fm3m) with a unit cell parameter a = 4.04940Å and a closed packed hexagonal Co structure that is also face-centered cubic type, with a unit cell parameters a, and c of a = 2.50310Å and c = 4.06050Å.

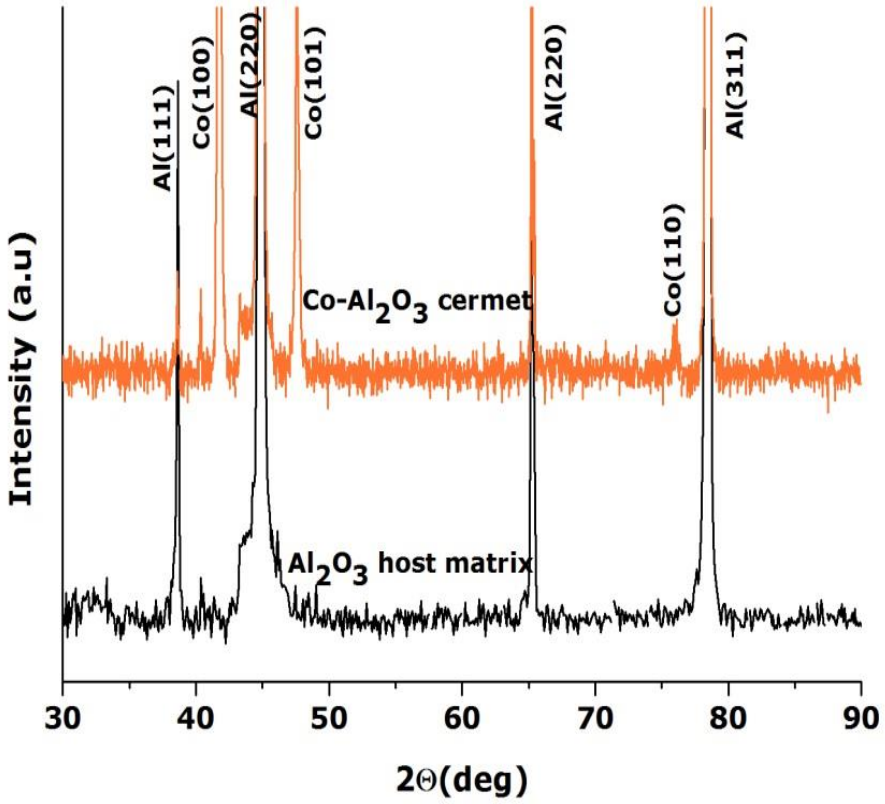

Figure 5.3: Typical X-Rays Diffraction of the optimized Co nanocylinders-Al_2O_3 cermet.

There are no diffraction peaks that correspond to the anodic alumina (Al_2O_3), implying that the host matrix Al_2O_3 surrounding the Co nanocylinders is crystallographically amorphous and the Al Bragg peaks are due to the Al substrate.

Likewise, no Co oxide or Co-Al based phases were detected indicating that there was no oxidation of Co nanocylinders and no interfacial interdiffusion between the Co nanocylinders and the Al_2O_3 host matrix at least at the level of the XRD detection limit. This result is in agreement with results reported by Darques and Cuevas [5.6-5.7]. A. Cuevas [5.6] investigated the effects of electrochemical variables, electrodeposition time and applied cell potential on the optical properties of electrochemically grown cobalt-alumina composite layer for solar thermal selective absorbers. Darques [5.7] studied how the microstructure of cobalt nanowires varies with the pH of the electrolyte. They used a three-probe electrodeposition system at room temperature, their cobalt nanowires presented a dominant fraction of the grains with the c-axis oriented perpendicular to the wires.

5.2.2 X-ray Diffraction of the Optimized (Co-Ni), nanocylinders -Al_2O_3 cermet.

Fig. 5.4 reports a typical X-Rays Diffraction of the dual ferrogmagnetic metal selective solar absorber coating optimized Co-Ni nanocylinders-Al_2O_3 cermet without any laser surface treatment. Co, Ni and Al diffraction peaks coincide with those given within the JCPDS cards 00-004-0787 and 00-005-0727 and 00-004-0850 of Al, Co and Ni structures, respectively. intensity Bragg peaks.

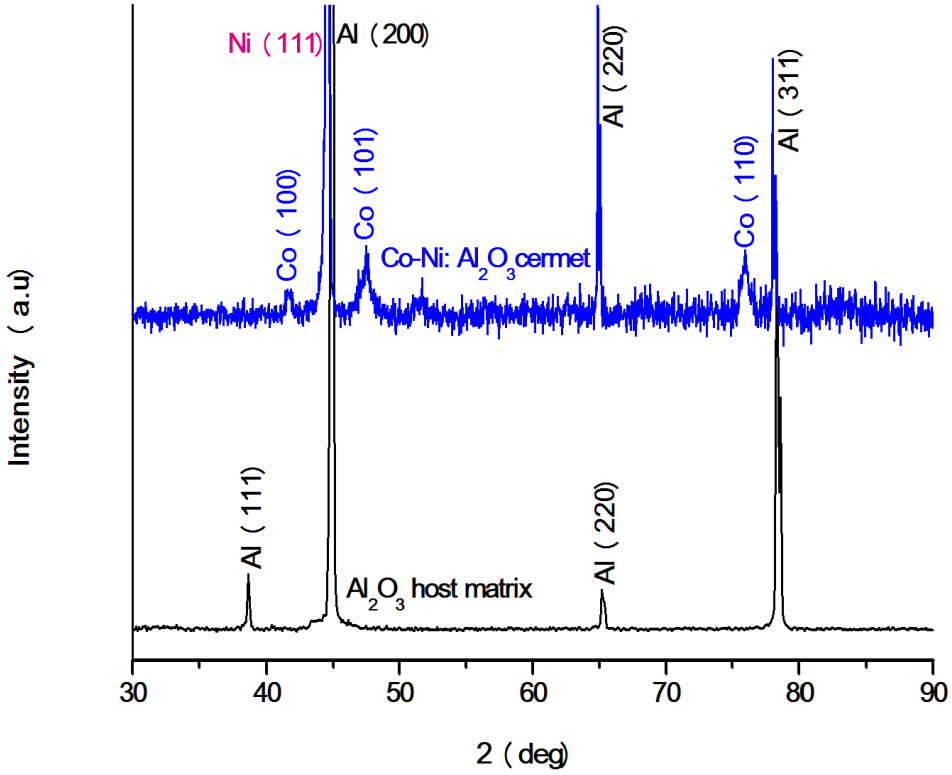

Figure 5.4: Typical X-Rays Diffraction of the optimized (Co-Ni) nanocylinders-Al_2O_3 cermet.

The alumina host matrix shows the following Al diffraction peaks (111), (220) and (222) of low intensity with (200) and (311) of higher intensity. The Co diffraction peaks corresponding to reticular orientations of (100), (002), (101), (102), (110), which as expected is similar to the diffraction pattern shown in Fig. 5.5 for the Co-Al_2O_3 selective cermet solar absorber coating. The XRD pattern also shows the presence of a major intensity Ni(111) peak which is in agreement with EDX data.

All Bragg peaks are attributed to the face-centered cubic Al structure (spacegroup Fm3m) with a unit cell parameter a = 4.049˚A and a closed packed hexagonal Co structure that is also face-centered cubic type, with a unit cell parameters a, and c of a = 2.503˚A and c = 4.061˚A; and face-centered hexagonal Ni structure (space group Fm3m) with unit cell parameter a = 3.52380˚A

Similar to the Co-Al_2O_3 cermet discussed above, the Co-Ni:Al_2O_3 selective absorber shows no diffraction peaks that correspond to the anodic alu-mina (Al_2O_3), inferring again that the host matrix Al_2O_3 surrounding the Co and nanocylinders is crystallographically amorphous and that the Al Bragg peaks are due to the Al substrate. Ni oxide, Co oxide, Co-Al, Ni-Al or Co-Ni based phases were not detected indicating that (103) are observed. It can be concluded no oxidation of Co and Ni nanocylinders and no interfacial interdiffusion. This result is in agreement with results reported by Darques[5.6], Cuevas[5.7] and those of the Co-Al_2O_3 cermet investigated.

5.3 EDS ANALYSIS TUBULAR COBALT NANOCOMPOSITES

The chemical composition analysis of the Co and Ni nanocylinders within the nanoporous anodized alumina host matrix was investigated by EDS measurement. The peak positions are specific to a particular element and intensity (height) is proportional to its relative abundance. The cobalt and nickel contents of Co-Al_2O_3 and (Co-Ni)-Al_2O_3 cermets are listed in the Tables 5.1 and 5.2.

5.3.1 EDS analysis of the Co-Al_2O_3 cermet

The EDS spectra shown in Fig 5.5 demonstrated 2 Co, Al and O intense energy related peaks onto a broad background peak. EDS is a complementary elemental analysis technique to XRD, the results obtained are in good agreement. Both spectra show the marked presence of cobalt, it can be concluded that the cermet designed is indeed electrochemically grown cobalt-alumina composite layer.

There are no B, S, or Na peaks which would originate from the used H_3BO_3, H_2SO_4, or NaOH solutions during the etching and electrodeposition phases. Table 5.1 reports the average elemental distribution within the 3 regions of the laser surface structured sample.

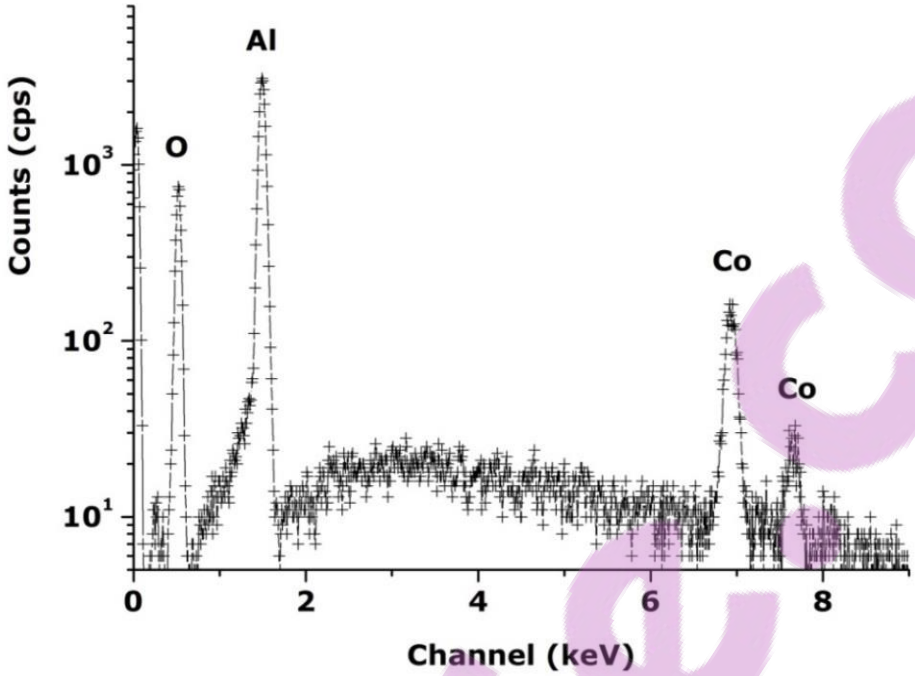

Figure 5.5: EDS spectrum of the Co nanocylinders within the nanoporous anodized alumina host matrix onto the Al substrate**.**

Element	Weight % (a)	(b)	(c)
O	30.65	59.64	44.38
Al	53.92	0.02	54.47
Co	15.43	40.34	1.14
Total	100	100	100

Table 5.1: EDS elemental analysis of the Co nanocylinders-Al_2O_3 cermet

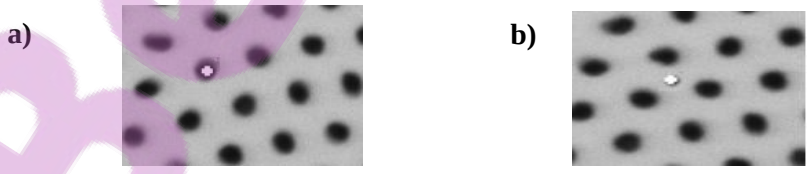

Figure 5.6: SEM images of regions a) and b) EDS elemental analysis of the alumina cermets.

The EDS confirms the presence of Co inside the Al_2O_3 pores. Region (a) represents the analysis made inside the alumina host matric pore as indicated by the white spot. The low Co weight percentage (15.4%) seems to indicate that the Co fills only a fraction of the pores following the laser irradiation. Region (b) shows the elemental analysis of the wall of the host matrix i.e. the conical-like columns shows a relatively large amount of Co & O with a minute amount of Al. Region (c) of the EDS analysis describes the elemental composition for the region in between the conical shaped islands sample centre. This section has 54.5 % Aluminium and 44.4% Oxygen with very low percentage of Co (1.1%). Yet, the electron probe beam will not only scan the indicated spot but its surroundings as well and inevitably pick the Al, Co and O, this EDS trend seems in agreement with the proposed Co melting/partial diffusion of Co hypothesis.

5.3.2 EDS analysis of the (Co-Ni) nanocylinders-Al_2O_3 cermet

Fig. 5.8 shows the result of the EDS analysis of the (Co-Ni) nanocylinders-Al_2O_3 cermet solar absorber deposited onto flexible Al substrate. This EDS spectra confirms that Co and Ni nanorods were successfully grown inside the host matrix pores. One can also see that the volume of the Co nanorods is larger than that of the Ni nanoparticles. This can be explained starting with the electrodeposition conditions, Ni and Co respond differently to the concentration of the electrolyte, electrodeposition time and current density. A larger percentage of Ni would probably require a higher current density and longer electrodeposition time.

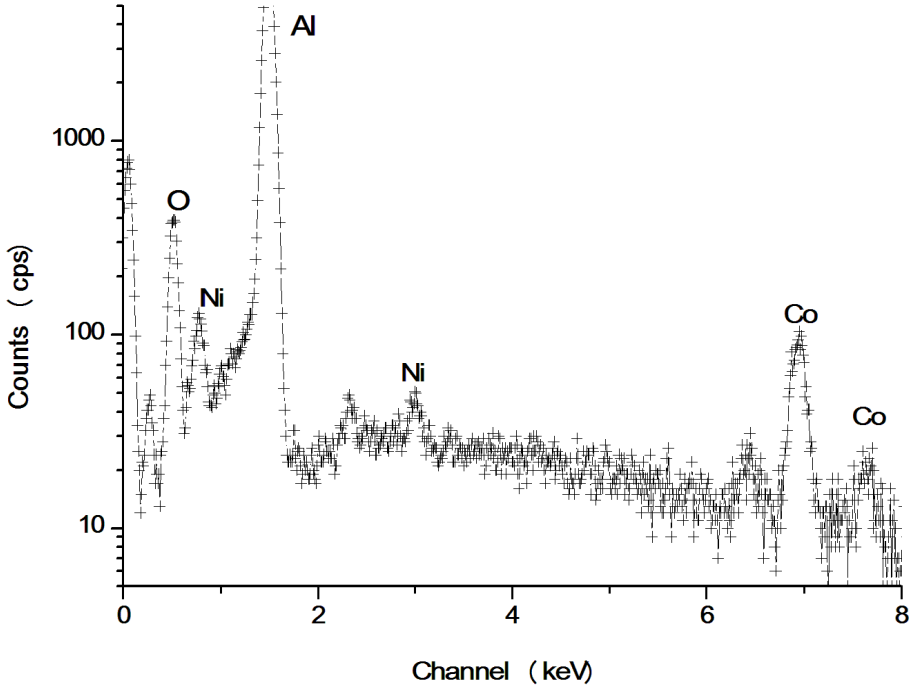

Figure 5.7: EDS spectrum of the Co-Ni nanocylinders within the nanoporous anodized alumina host matrix

Element	Weight % (a)	(b)
C	13.91	12.19
O	20.36	49.36
Al	62.85	35.65
Co	1.69	0.00
Ni	1.19	0.00
Total	100	100

Table 5.2: EDS elemental analysis of the Co nanocylinders-Al_2O_3 cermet

Region (a) shows the EDS scan that was taken inside the Al_2O_3 pores, this section has 62.9 % Aluminium and 20.4% Oxygen with low percentage of Co (1.7%) and Ni (1.2%).

Region (b) shows a relatively large amount of Al & O, 12.19% Carbon and the absence of Co and Ni. This EDS analysis of this region was done on the on the alumina wall as shown in Fig. 5.6 It can be seen from this result that there is no electrochemical deposition of cobalt and nickel on top of the alumina host matrix, the ferromagnetic metal ions are only inside the pores.

5.4 RBS ANALYSIS OF TUBULAR COBALT NANOCOMOSITES

Relatively to EDS, RBS offers an advantage in terms of spatial resolution and hence more adequate to shed-light on the Co diffusion if any, Fig. 5.7 reports the corresponding RBS profiles before and after laser surface structuring. While the RBS profiles seem to superpose below the Al channel' edge (about channel 550) including the O channel's edge, the Co profiles seem to be altered. More precisely, the Co depth distribution has been altered following the laser irradiation (Continuous line & cross data, channel region:~550 to ~800). Relative to the non irradiated phase (Dashed line &open circle data, channel region: ~550 to ~800), the Co depth pro-file of the laser irradiated sample seem to peak up at the surface. This appear to substantiate the diffusion of Co from the inner partof the pores towards the surface and hence would explain, a priori, the conical like-shaped islands formed on the surface observed in the AFM investigations (Fig. 5.4).

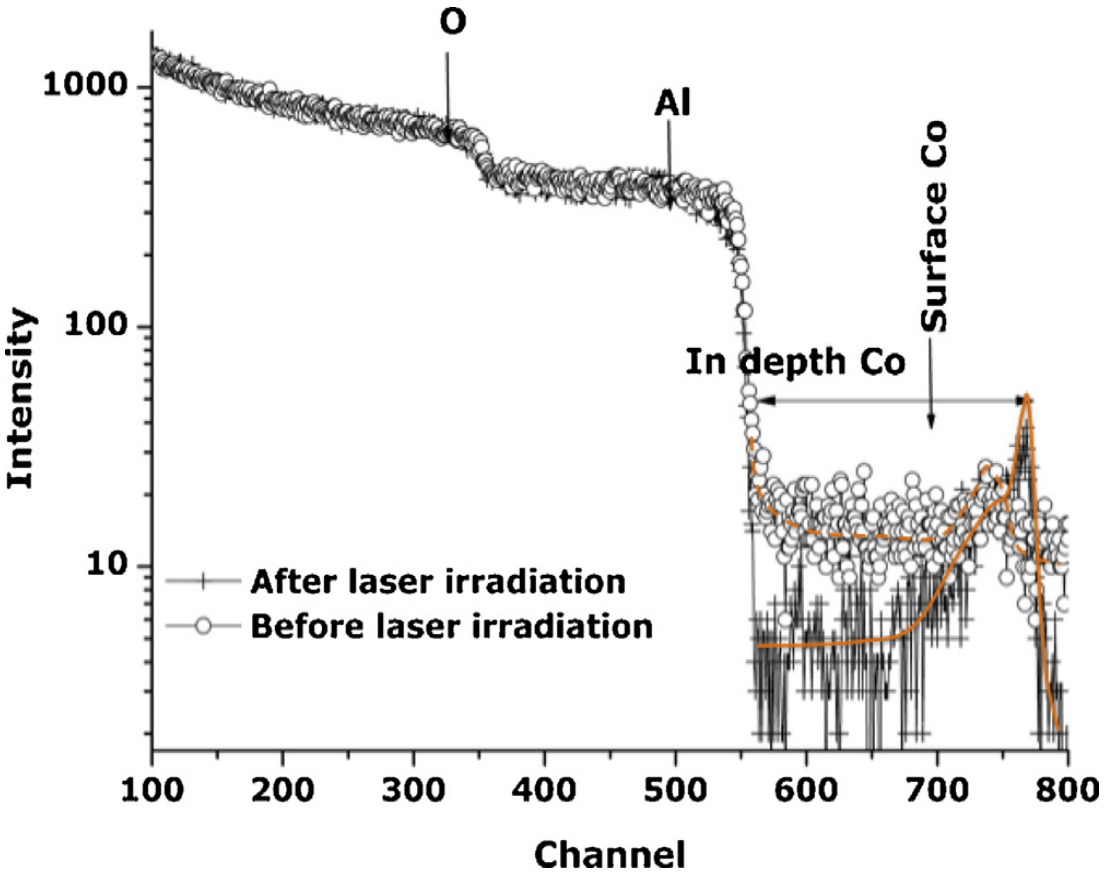

Figure 5.8: RBS chemical profiles of the optimized Co nanocylinders-Al_2O_3cermet before (Open circles) and after (Cross) the surface laser irradiation. Note the Co depth distri-bution within the non irradiated phase (Dashed line & open circle data) and following the laser irradiation (Continuous line & cross data) within the channel region: ~550 to ~800.

5.5. TOTAL REFLECTANCE AND THE INFRARED EMISSIVITY (ε) OF TUBULAR COBALT NANOCOMOSITES

This result was published in Applied Surface Science 347 (2015) 679–684. Reflectance measurements are carried out in order to investigate the spectral selectivity of the optimized Co-Al_2O_3 and Co-Ni:Al_2O_3 selective solar absorber cermets. A high spectral absorptance $\alpha(\lambda)$ is not enough for an effective selective solar absorber. This has to be complemented by a very low spectral emittance $\varepsilon(\lambda)$. The thermal emittance spectra on the optimized sample were acquired by an emissometer model AE1, which has an accuracy of 0.01 emittance units. The corresponding value at 100ºC is about $\varepsilon(\lambda)$~0.03.

5.5.1 Total Reflectance of Laser surface structured Co-Al_2O_3 cermet

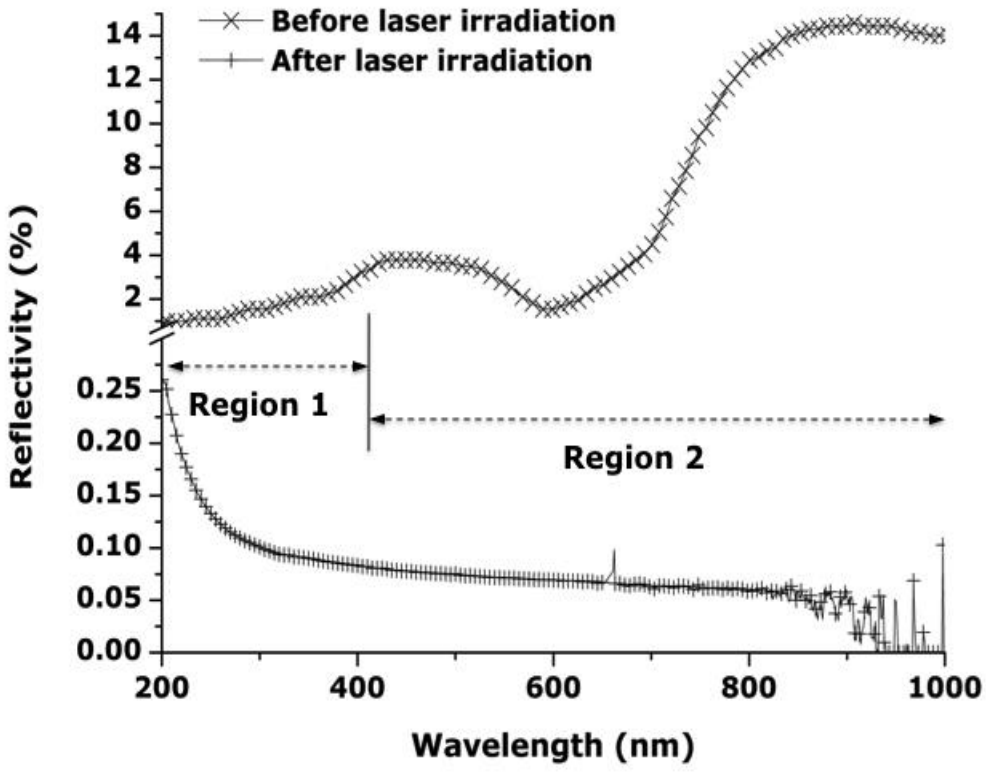

Figure 5.9: Total reflectance (specular and diffuse) of the laser surface structured selective solar absorber consisting of vertically oriented Co nanocylinders electrodeposited in porous Al_2O_3 deposited onto flexible Al sheets.

Fig. 5.9 indicates 2 regions: Region 1 (Bleu-UV:190-400 nm) and Region 2 (VIS-NIR: 400-1000 nm). In this latter region, the total reflectance is less than 0.1%. This very low value can be attributed to 2 aspects:

(i) The physical nature of the Co-Al_2O_3 cermet itself. The columnar, three-dimensional orientation of the Co nanocylinders within the oxidized Al_2O_3 host section would certainly increase the light trapping as in the case of selective solar absorbers consisting of metallic dendritic surface. Standard Co based cermets such as Co–Al_2O_3, Co_3O_4/Co, and Ni–Co_3O_4/Co nanocomposites are well known to exhibit high solar absorptance $\alpha(\lambda)$ and low emittance $\varepsilon(\lambda)$ (100 ◦C) coupled to a good thermal stability.

(ii) The 1-D shape of the Co nanocylinders conjugated to their parallel three-dimensional orientation. Comparatively, the current optimized laser surface irradiated Co nanocylinders-Al_2O_3 cermet exhibits a larger absorptance $\alpha(\lambda)$ of about 0.99 in the spectral range of 200-1000 nm; one can notice the limit of detection in the 900-1000 nm region where the reflectance is lower than 0.0005.

The elevated absorptance $\alpha(\lambda)$ of about 0.99 cannot be only explained by the nature of the Co-nanocylinders-Al_2O_3 and its initial morphology but by considering the femtosecond laser-induced surface structural features ranging from nanoscale to microscale as well. The observed highly reduced reflectance can result from several absorption mechanisms which include:

a) Anti-reflection effect of random sub-wavelength surface textures in terms of graded refractive index at the air/solid interface. The solar energy gets absorbed by multiple reflection and partial absorptions after each light-surface geometry interaction. For long wavelength the selective surface appears smooth and responds like a mirror because the thermal infrared wavelengths are greater than the dimensions of the surface features. Therefore the ultrafast laser surface structured Co nanocylinders-Al_2O_3 cermet does not need essentially an antireflection layer [5.8] .

b) Plasmonic effect also known as the quantum confinement effect. The surface plasmons confined to the surface interact strongly with light and they have the unique capacity to confine light to very small dimensions. The alumina host matrix is a good choice for a

template since the channel diameters are easily adjusted to sizes enabling quantum confinement [5.8-5.9].

c) The various sizes and shapes of the surface nanostructures that are smaller than light wavelength can also give rise to the enhanced absorptance [5.8-5.10].
Lastly, there are also contributions to absorption from surface structures that are greater than the light wavelength due to trapping of the light in cavities and Fresnel angular dependence of reflection. The overall effect of all these absorption mechanisms results in a strong broadband absorption of electromagnetic waves.

5.5.2 Model calculation of Laser surface structured Co-Al_2O_3 cermet

The reflectance spectra of the femto second laser surface structured Co-Al_2O_3 nanocermet was simulated using an optical spectrum simulation program called SCOUT software using the Bruggeman effective medium model [5.11]. Co and Al_2O_3 selected from the database available in the software and input data comprising of thickness and optical parameters (n and k values) were used to design the model of four layers. The software is used for the analysis of optical spectra by comparison of measurements (reflectance, transmittance, absorptance etc) and models (Tauc-Lorentz interband transition model, user-defined expressions for optical constants, imported dielectric functions, classical Drude model etc). It uses Fresnel formalism to calculate reflectance of the cermet and a downhill simplex method to minimize the fit deviation, which gives graphics to windows and data to text files an output [5.12-5.13]. Comparison between the simulated and experimental reflectance is used to validate the efficiency of the procedure in determining the complex refractive index. It is seen from Fig. 5.10 that there is a good agreement between the simulated and experimental reflectance spectra of the femto second laser surface structured Co-Al_2O_3 nanocermet.

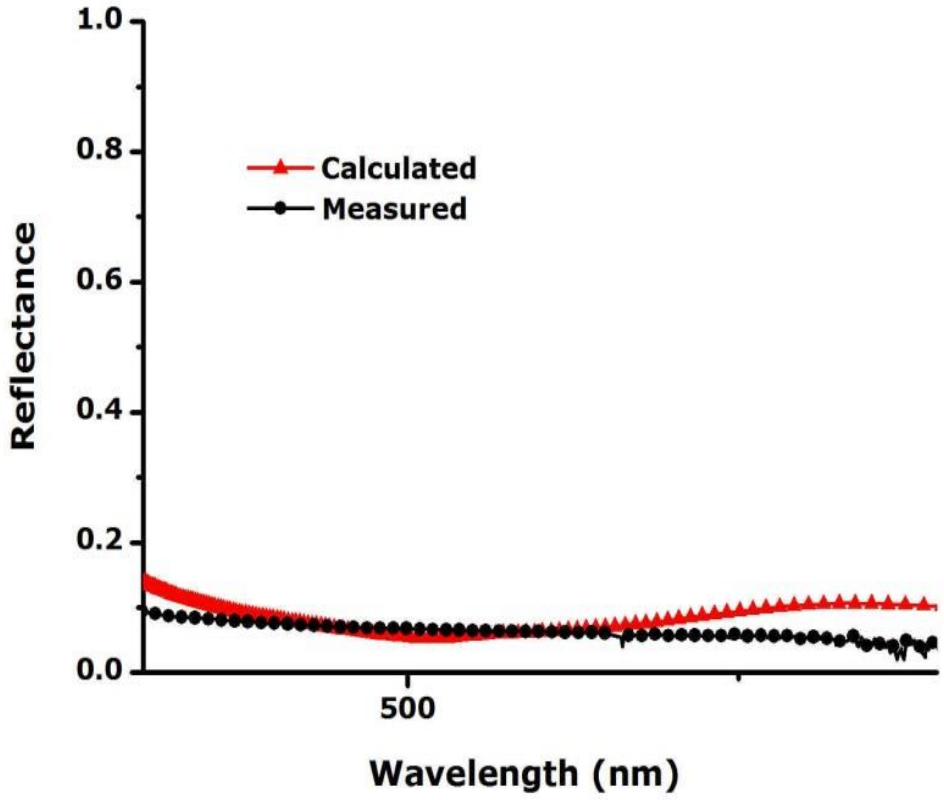

Figure 5.10: Comparison between the simulated and experimental total reflectance (specular and diffuse) of the laser surface structured Co-Al_2O_3 cermet

5.5.3 CV Electrodeposition of (Co-Ni) nanocylinders in Al_2O_3 host matrix

The Autolab PGSTAT 302N potentiostat setup was used for electrodeposition of Co and Ni nanocylinders in the alumina host matrix using the cyclic voltammetry (CV) technique. The electrolysis cell contained the electrolyte with composition nickel sulphate, cobalt sulphate magnesium sulphate ammonium sulphate and boric acid in 30ml distilled water. Two-electrode measurements are made using the Al host matrix as the working electrode and a platinum counter electrode. Fig 5.11 shows the change in the charge and current on the surface of the sample during electrodeposition and CV performed for 80cycles at scan rate 200Vs^{-1}

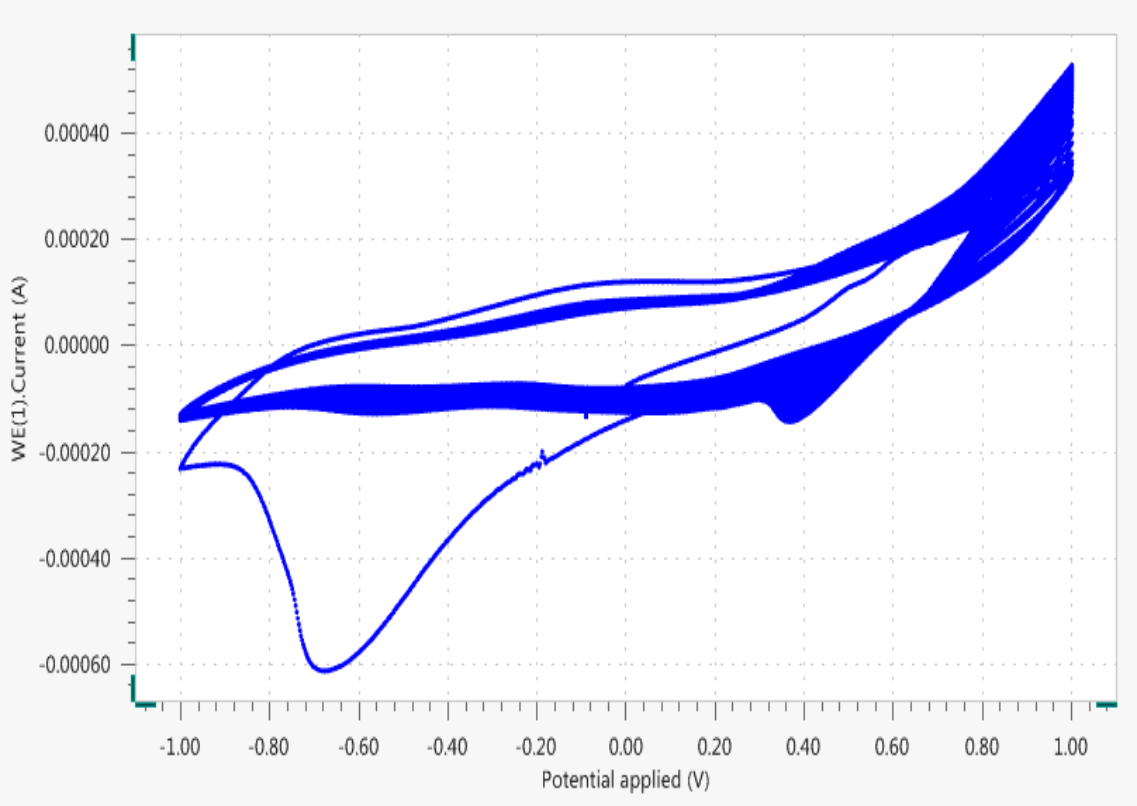

Figure 5.11: Electrodeposition of Cobalt and Nickel in the Alumina host matrix using CV for 90 cycles

By applying AC voltage, almost 100% of the pores were homogenously filled with the ferromagnetic nanorods, cobalt and nickel. This is most probably due to the rectifying nature of the barrier layer. The electrodeposited arrays cobalt and nickel follow the quasihexagonal structure and are uniform throughout the surface with a uniform nanowire density. If the rate of the electrodeposition is faster than the metal ion transportation, it can lead to a non-uniform growth and low filling rate of the pores on the surface. The optical properties (reflectance and emissivity depend on the particle shape, size, concentration of the article in the matrix, article distribution and local dielectric environment of the dielectric matrix. It was necessary that the CV is performed accurately enough to allow. The more regular and hexagonal the cermet's pore array is the stronger its absorbance

5.5.4 Total Reflectance of the optimized (Co-Ni) nanocylinders-Al_2O_3 cermets

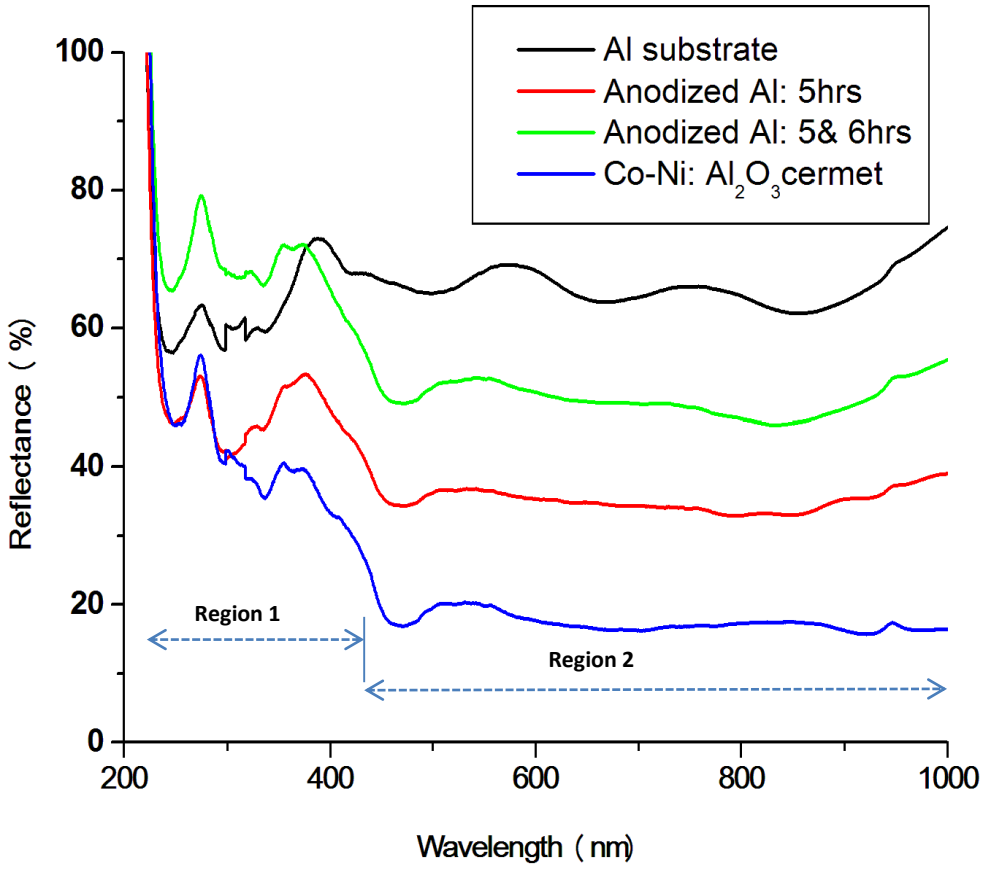

Figure 5.12: Total reflectance (specular and diffuse) of the laser surface structured selective solar absorber consisting of vertically oriented Co-Ni nanocylinders electrodeposited in porous Al_2O_3 deposited onto flexible Al sheets.

Fig. 5.12 shows typical reflectance curves at the various stages when designing the (Co-Ni)-Al_2O_3 cermet. Again as with the Co-Al_2O_3 cermet, there are 2 distinct regions: Region 1 (Bleu-UV: 190-400 nm) and Region 2 (VIS-NIR: 400-1000 nm). In Region 2, the reflectivity of the un-anodized Al substrate is ~ 70%. When anodized for 5hrs this value falls to 50%. In the case of the Al substrate that was designed by the two-step anodization process at temperature < 4°C for longer anodization time of 5 and 6 hrs, 35% reflectance is observed. Coating thickness as well as particle size, shape and orientation affect how strongly the optical properties are expressed across the solar and IR spectra. It was found that an increase in anodization time creates a thicker coating beneficial for high absorptance in the visible range, consequently the reflectivity value decreases from 50% of Al substrate anodized for 5hrs to 35% with the coating prepared by the two-step anodization process.

In addition, this 15% reduction in reflectivity and elevation in absorptance can be explained by shape and orientation of the Alumina host matrix developed. It is noted that the single-step 5hr anodization process resulted in a dense but no regular pattern, however, a two-step anodization method resulted in a more regular pore array which has a hexagonal shape. This particular 1-D shape and columnar type spatial orientation of the Alumina host matrix would certainly favour the light trapping by multiple reflections and partial absorption as in the case of selective absorbers with dendrite, needle-like microstructures on the same scale as the wavelength of the incident radiation.

The fourth and final reflectance curve in Fig. 5.11 belongs to the designed selective solar absorber consisting of vertically oriented Co-Ni nanocylinders electrodeposited in porous Al_2O_3 deposited onto flexible Al sheets. After electrodeposition of ferromagnetic Co-Ni nanocylinders in the Alumina host matrix that was developed by the two step anodization method, the reflectivity is reduced from 35% of the alumina host matric to ~ 15%. The Co-Ni nanocylinders into Alumina host matrix exhibited an optical absorptance $\alpha(\lambda) \sim 83\%$ and a relatively low emittance $\varepsilon(\lambda) \sim 0.12$ in the spectral solar range of 200-1100nm.

5.6 THE EFFECT OF ANNEALING ON THE PROPERTIES OF LASER SURFACE STRUCTURED Co- Al_2O_3 SOLAR ABSORBER

The laser surface structured Co nanocylinders-Al_2O_3 cermets were annealed at various temperatures in a hydrogen atmosphere for 2h to study the annealing temperature dependence of the structural, chemical and optical properties of the particles grown on aluminium substrates by standard electrodeposition. In addition to optical efficiency, thermal stability is also an important requirement for solar absorber coatings. The study of the thermal stability in solar absorber coatings is very important as the degradation of the coatings at higher operating temperatures results in a decrease in solar absorptivity and an increase in thermal emissivity. As before the structural and optical properties of the annealed samples are investigated by X-ray diffraction (XRD), Raman spectroscopy, scanning electron microscopy (SEM), energy dispersive spectrometry (EDS), and total reflectivity and emissivity using Cary 5000 UV–VIS–NIR spectrophotometer.

5.6.1 Scanning electron microscopy (SEM) of Annealed Coatings

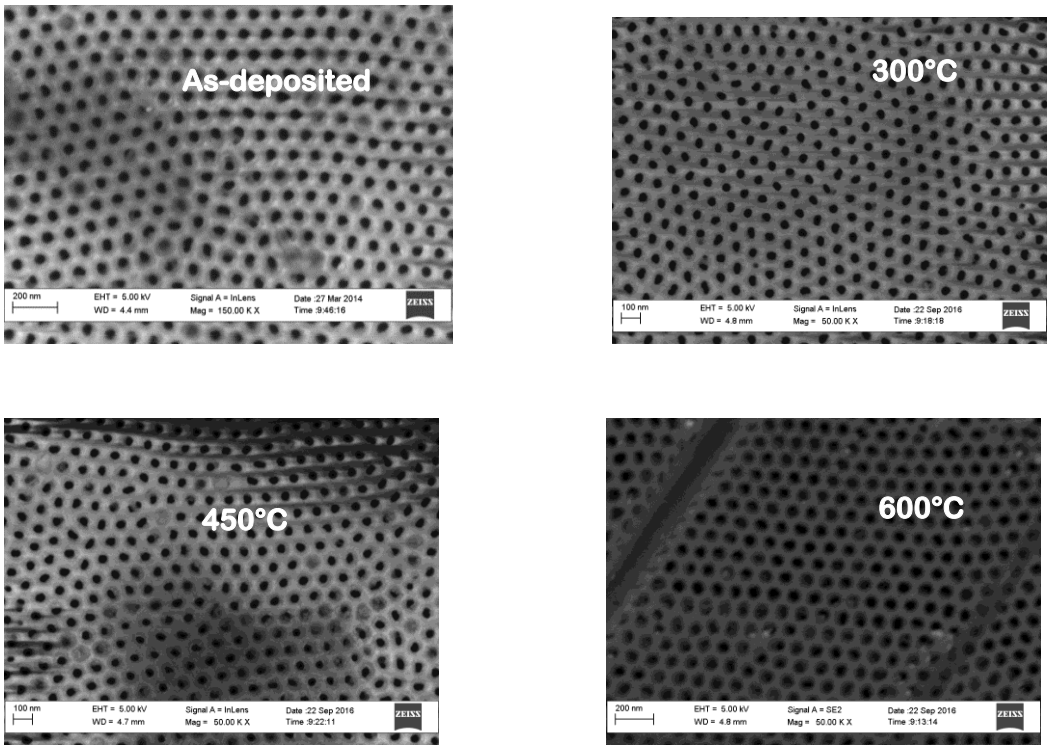

Figure 5.13: shows the surface morphology of laser surface structured Co-Al_2O_3 cermet solar absorber as deposited and heat treated at different temperatures 300ºC, 450ºC and 600ºC in air for 2 h.

Fig. 5.13 represents the surface morphology of the laser surface structured selective solar absorber consisting of vertically oriented Co nanocylinders in Al_2O_3 host matrix deposited onto Al substrate, after annealing in air for 2h at temperatures 300ºC, 450ºC and 600ºC.
As expected the SEM micrographs of the three annealed cermets exhibit the well-arranged hexagonal array observed throughout the surface forming a porous surface structure.
A typical columnar growth of Co nanocylinders in Al_2O_3 host matrix similar to the original as-deposited cermet is observed for all the annealed samples with centre to centre distance ~53.7nm, ~ 70.2nm. When the annealing temperature increases to 600ºC, the grain size of the cermet becomes larger which can be linked to the annealing. Heat-treatment normally causes an increase of the crystallite size by providing enough energy for the coagulation of a large number of nanoparticles [5.14].

At 600ºC the surface of the annealed Al_2O_3 show some lumps. Though these can be confused to formation of Co_2O_3 from the oxidation of cobalt, they are most likely a result of the coating used to prepare the sample for analysis by SEM. In general SEM analysis shows that the regular hexagonal structure of the porous alumina host matrix containing cobalt nanocylinders does not change after annealing treatment. Condensation caused a decrease of absorptance by cracking the surface, this can be prevented by applying a protective layer on the surface [5.15].

5.6.2 EDS analysis of Annealed Coatings

Fig. 5.14 shows the EDS analysis laser surface structured selective solar absorber consisting of Co nano-cylinders electrodeposited in porous Al_2O_3 host matrix deposited onto flexible Al substrate after annealing in air for 2 h temperatures 300ºC, 450ºC and 600ºC in air for 2 h.
EDS spectra showed only sharp peaks from aluminium, oxygen and from the cobalt nanoparticles, confirming the pure nature of the prepared laser surface structured Al_2O_3-Co cermet solar absorber coatings. Annealing up to 600°C shows a barely any change in the Oxygen and aluminium signal, however there is a change in the composition of cobalt. This behaviour is to be expected as it agrees with the fact that the Al_2O_3 host matrix have excellent thermal stabilities implying its composition will remain constant at the three different annealing temperatures. At temperatures up to 600ºC the intensity of the Co peak remains constant which implies good adhesion between the Co atoms and the alumina cermet. The choice of dielectric material is very important for the performance of a selective solar absorber. In this study Al_2O_3 has been selected as the dielectric host matrix for the cermet

coating due to its high thermal stability as evidenced by the constant oxygen and aluminium signal in the EDS spectra in Fig.5.14. The Al_2O_3 host matrix also exhibits an interesting property of low refractive index (n=1.65) and this gives it the ability to reduce the front surface reflections of the laser surface structured selective Al_2O_3-Co nanocermet coating.

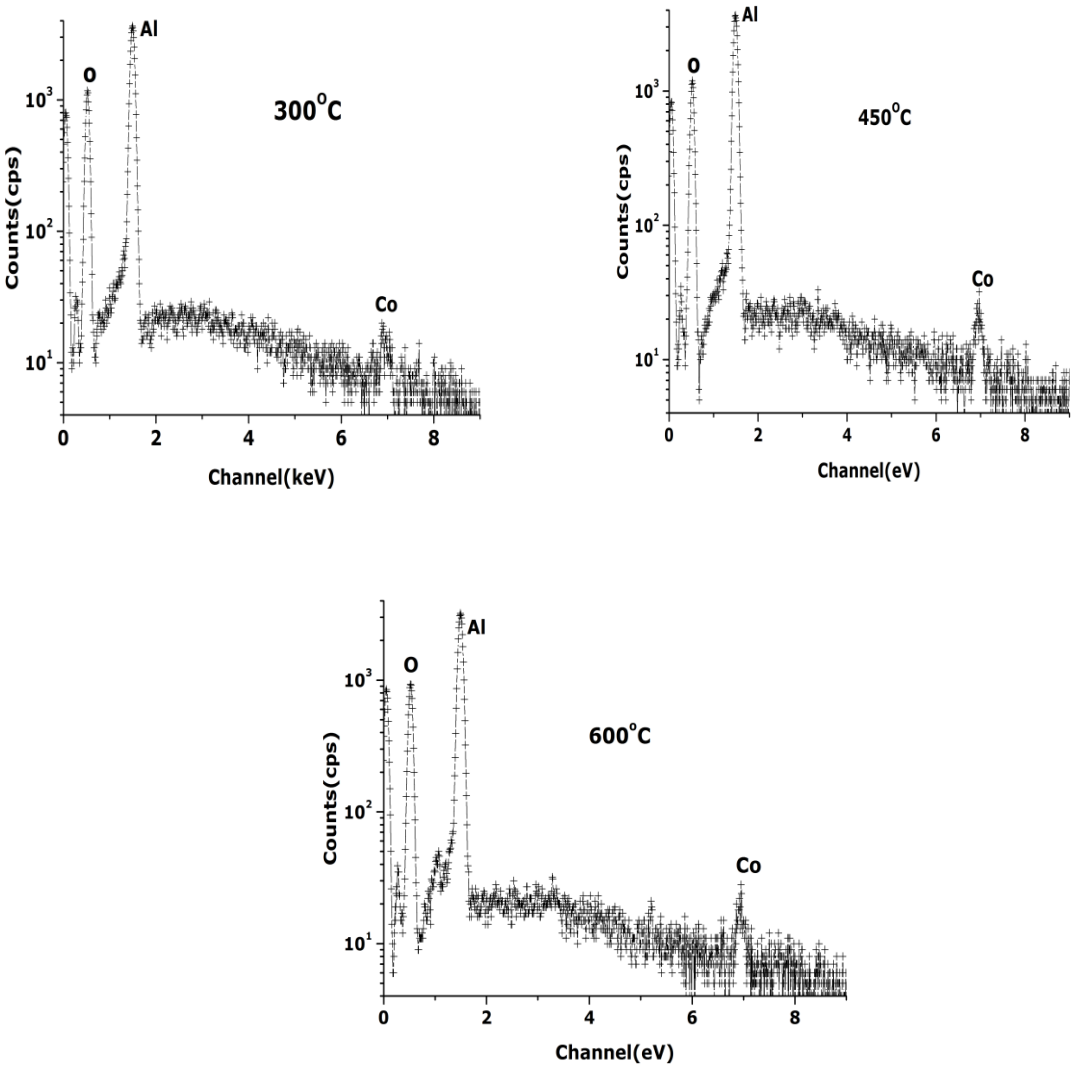

Figure 5.14: shows the EDS spectrum of laser surface structured Co-Al_2O_3 cermet solar absorber as deposited and heat treated at different temperatures 300ºC, 450ºC and 600ºC in air for 2 h.

5.6.3 XRD analysis of Annealed Coatings

The XRD pattern of the annealed Co-Al_2O_3 cermet is depicted in Fig. 5.15. One can see that the original Al diffraction peaks (111), (220) (311) of low intensity and (200), (400) of high intensity seen in the non-annealed deposited samples appear in the samples annealed at the different temperatures. All Al diffraction peaks coincide with those given within the JCPDS cards 00-004-0787 that describes the light gray metallic Al substrate. These Bragg peaks are attributed to the Al face-centered cubic lattice (Space group Fm3m) with a unit cell parameter a = 4.049˚A.

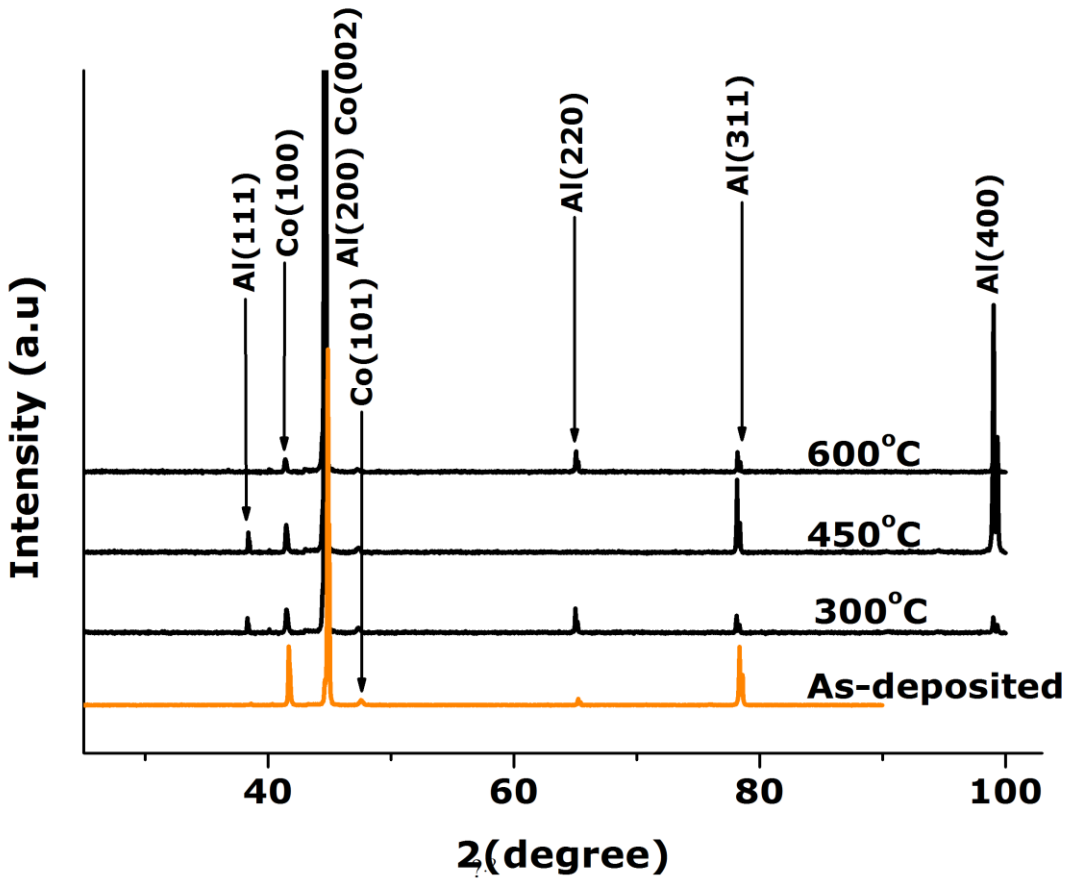

Figure 5.15: X-rays diffraction of the optimized laser surface structured Co nanocylinders-Al_2O_3 cermet as-deposited state and annealed at 300°C, 450°C, and 600°C in air for 2 h.

The Co diffraction peaks corresponding to reticular orientations of (100), (002), (101) are observed and they coincide with those given with the JCPDS cards 00-005-0727. These Bragg peaks are attributed to the Closed packed hexagonal Co lattice that is also face-centered cubic type with unit cell parameters a = 2.503˚A and c = 4.061˚A.

Cobalt has a face-centered cubic (Cu type) structure above 450°C and a closed packed hexagonal structure stable at room temperature. Similar to the previous XRD results of the non-annealed optimized samples in section, no diffraction peak for alumina is observed as expected due to the amorphous nature of the alumina. The XRD pattern also indicates a decrease in the intensity of the

Co (100) and Co (101) peaks with increasing annealing temperatures. The lowest intensity of the signal of these peaks is at 600 °C. This is mainly because of decrease in the thickness of Co nanoparticles due to oxidation and also the hypothesis prior discussed that there is fast melting of Co and its partial diffusion out of the pores creating columnar laser induced surface structures shown by the AFM images.

5.6.4 Raman analysis of Annealed Coatings

Raman spectroscopy is are powerful and non-invasive characterization technique used to identify and characterize cobalt oxides. The Raman spectra for femto-second laser surface structured nanocermet on Al substrate and annealed at different temperatures is depicted in Fig. 5.16. The oxides of cobalt that we will look for are Green cobalt (II) oxide (CoO), blue cobalt (II, III) oxide (Co_3O_4) and black cobalt (III) oxide (Co_2O_3). Co_3O_4 and CoO the only two stable oxides of cobalt which explains why Co_3O_4 and not Co_2O_3 phase was found in the samples. The standard Raman spectra of Co_3O_4 established by Hadjiev [5.16] shows five Raman-active modes identified at 194, 482, 522, 618 and 691 cm^{-1}. The Raman spectrum of CoO is represented by a two-phonon peak at ~ 1060cm^{-1} at room temperature as well as magnon lines below 300 cm^{-1}. The intensity of laser excitation is kept low in CoO Raman scattering in order to avoid thermal oxidation of CoO. The spectra of the samples annealed at 600°C revealed three broad bands centered at 482, 522, 691 cm^{-1} which corresponds to the vibration of Co_3O_4 due to oxidation of the cobalt nanoparticles. This Co_3O_4 oxide has profound influence on the optical performance of the annealed laser surface structured Co-Al_2O_3 nano-cermet, it is responsible for the degradation of the cermet at high temperature as evidenced by the low solar absortance and high emittance values in Table 5.3. The shape of the Raman spectra doesn't show significant change up to 450°C and shows no formation of Co_3O_4 indicating the stable structure of the cermet solar absorber coatings. The modes of

Co_3O_4 are however pronounced for 600°C demonstrating that there is degradation of the laser surface structured Co nanocylinders-Al_2O_3 cermet solar absorber coatings. Diffusion of Co towards the surface of the nanoporous host matrix and formation of the three Co_3O_4 modes are responsible for this degradation at 600°C implying that this particular cermet solar absorber coating is not suitable for high-temperature solar applications.

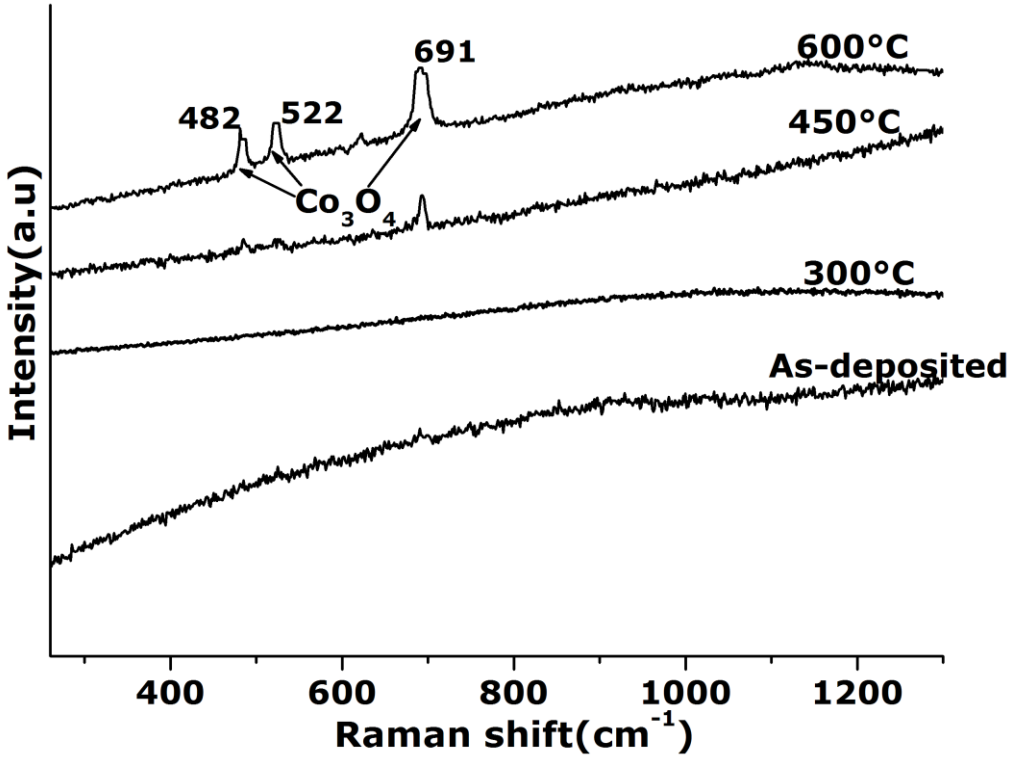

Figure 5.16: Raman spectra of the annealed laser surface structured Co nanocylinders-Al_2O_3 cermet solar absorber

5.6.5 Total reflectance and infrared emissivity ε(λ) of Annealed Coatings

Fig. 5.17 reports the total reflectivity (both specular and diffuse) of the optimized laser surface structured Co nanocylinders-Al_2O_3 cermet samples with SEM images shown in Fig 5.1c, were prepared under the same conditions and annealed at different temperatures 300ºC, 450ºC and 600ºC in air for 2h. This total reflectivity was measured with a lambda 900 UV–VIS–NIR spectrophotometer from Varian, Inc. (model internal DRA-2500) in the

wavelength range of 190 nm–2500nm under normal incidence. The corresponding values of the laser structured coating are given in Table 5.3.

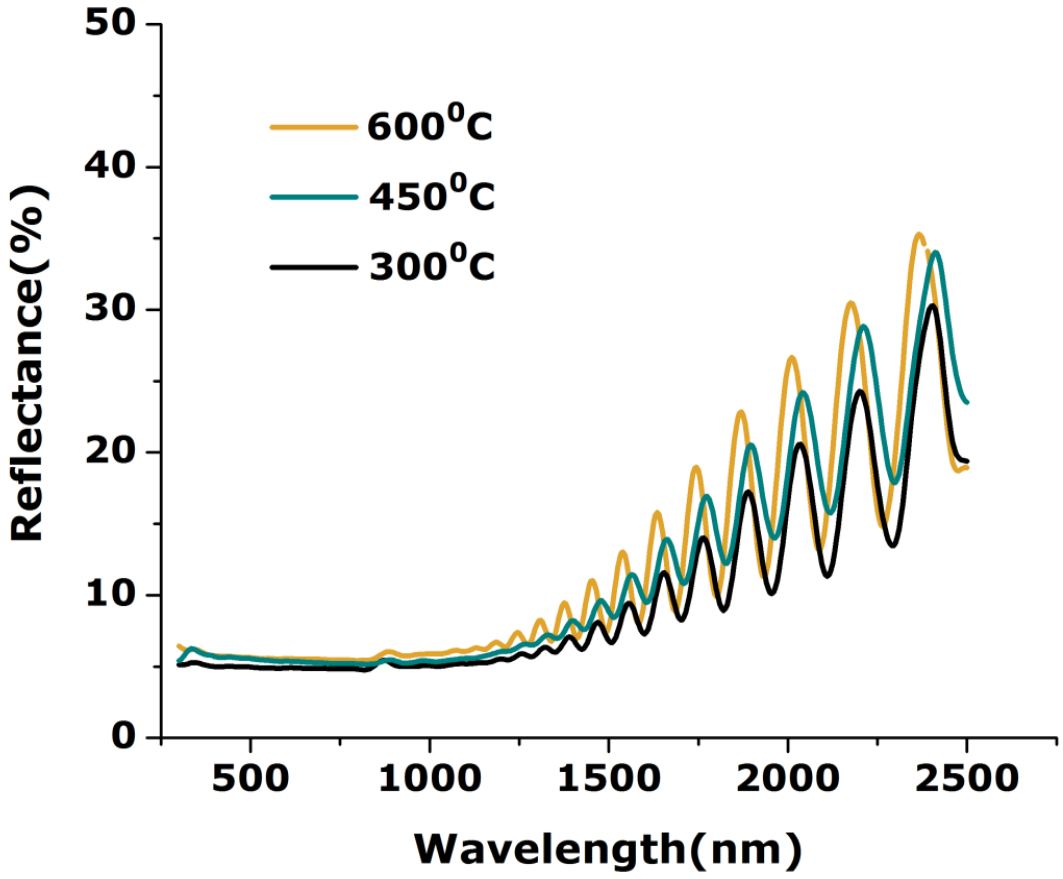

Figure 5.17: Total reflectance of the annealed laser surface structured Co nanocylinders-Al_2O_3 cermet solar absorber.

The optimized sample shown in Fig. 5.1c exhibits lowest reflectance of ~ 5% in the spectral region 300-1300nm and a higher reflectance (5-30%) in spectral region 1300-2500nm with an interference pattern which has increasing intensity in its oscillations. Annealing the cermet causes its absorptance to decrease, less of the incident light is absorbed and more light of varying intensity goes into multiple reflections which results in varying intensity of light interference that displays as an oscillating pattern. Another possible reason is the contribution of the femtosecond laser-induced nano and micro surface structures which enhance the surface nanoplasmonics of the cermet that will mean a stronger interference pattern.

With increase in the annealing temperature up to 600°C, the total reflectance shows no significant change in the reflectance spectra of the cermet. This indicates that the optimized femtosecond laser surface structured Co nanocylinders-Al_2O_3 cermet has good thermal stability up to 600°C in air but can only be confirmed after investigation by other techniques like Raman spectroscopy and of the effect of annealing on the solar selectivity (α/ε). This particular optical result can be attributed to the well-known outstanding properties of Aluminium oxide coatings that include high hardness, excellent dielectric properties, refractoriness and good thermal properties which makes them stable after annealing in air for 2h at the temperatures discussed. To achieve high solar selectivity, the coatings should exhibit low reflectivity in the visible near infrared (vis-NIR) region but high in the infrared region.

The solar absorptance α was calculated by numerical integration given in Eqn. 5.1 drawn from Chapter 3, section 3.2, using measured total reflectance spectrum found in Fig.5.15 in the solar region of 3-25 nm, and the solar irradiance at Air Mass 1.5 (AM 1.5). Where $I_{sol}(\lambda)$ is the incident radiation and $R(\lambda)$ is the reflection function of the material.

$$\alpha = \frac{\int_{300}^{2500} I_{sol}(\lambda)[1 - R(\lambda)]d\lambda}{\int_{300}^{2500} I_{sol}(\lambda)d\lambda} \qquad 5.1$$

The numerical calculation of the thermal emittance is done using Eqn. 5.2 drawn from Chapter 3 section 3.2 . $R(\lambda)$ is the measured reflectance in the solar region 5-50 μm and $I_b(\lambda, \mathrm{T})$ the black body spectrum for a given temperature T.

$$\varepsilon = \frac{\int_{5}^{50} [1 - R(\lambda)] I_b(\lambda, \mathrm{T})d\lambda}{\int_{5}^{50} I_b(\lambda, \mathrm{T})d\lambda} \qquad 5.2$$

	Annealing temperature (°C)	Absorptance (α)	Emittance (ε)
Sample 1	300	0.81	0.36
Sample 2	450	0.81	0.48
Sample 3	600	0.85	0.46

Table 5.3: Effect of annealing in air for 2h on solar absorptance and thermal emittance values of optimized laser surface structured Co nanocylinders-Al_2O_3 cermet solar absorber as grown on Al substrate.

As evident from Table 5.3, the solar absorptance decreases with increasing annealing temperatures. At 600°C, the oxidation of Cobalt to cobalt oxide as is confirmed by Raman leads to a lower absorptance and higher emissivity. Thermal stability of a selective solar absorber coating is very important because the absorber degrades at higher operating temperatures which causes a decrease in the selectivity [3.17]. This is true in the case of the annealed laser surface structured Co nanocylinders-Al_2O_3 cermet, the degradation is at higher operating temperature because of the oxidation of cobalt. To use the coating for CSP applications it is necessary for it to have every high structural, physical and chemical stability at high temperature (580°C) under vacuum, maintaining good performances in terms of high solar absorption and low thermal emissivity [3.18]. The laser surface structured Co nanocylinders-Al_2O_3 cermet exhibits high structural stability however from the results in Table 5.3 the marked decline in absorptance and increase in emittance confirms that this particular cermet is a good candidate for solar absorber applications at temperature lower than 500°C, which is mid-temperature applications.

5.7 REFERENCES

[5.1] H. Masuda, H. Yamada, M. Satoh, H. Asoh, M. Nakao, T. Tamamura, Highly ordered nanochannel array architecture in anodic aluminia. American Institute of Physics 1 (1997) I-534 - I-535.

[5.2] X. Zhang, Preparation of porous alumina by anodization. Nanyang Technological University, Singapore.

[5.3] Y. C. Sui, J. M. Saniger, Characterization of anodic porous alumina by AFM. Materials Letters 48 (2001) 127-136.

[5.4] H.E. Swanson, E. Tatge, National Bureau of Standards, (U.S.) Circular 1 (1953) 11.

[5.5] L.J.E. Hofer, W.C. Peebles, Journal of American Chemical Society 69 (1947) 897.

[5.6] A. Cuevas, L. Martínez, R. Romero, E.A. Dalchiele, R. Marotti, D. Leinen, J.R. Ramos-Barrado, F. Martin, Electrochemically grown cobalt-alumina composite layer for solar thermal selective absorbers. Solar Energy Materials & Solar Cells130 (2014) 380–386.

[5.7] M. Darques, J. Spiegel, J.D.-T. Medina, I. Huynen, L. Piraux, Ferromagneticnanowire-loaded membranes for microwave electronics. J. Magnet. Magnet.Mater. 321 (2009) 2055–2065.

[5.8] F. Ghmari, T. Ghbara, M. Laroche, R. Carminati, J.-J. Greffet, Influence of micro-roughness on emissivity. J. Appl. Phys. 96 (2004) 2656–2664.

[5.9] U. Kreibig, M. Vollmer, Optical Properties of Metal Clusters. (1995), Germany: Springer.

[5.10] I.H. Zabel, D. Stroud, Metal clusters and model rocks: electromagnetic proper-ties of conducting fractal aggregates. Phys. Rev. B 46 (1992) 8132–8138.

[5.11] W. Theiss, SCOUT Optical Spectrum Simulation. (2002), Achen: W. Theiss Hard-and Software.

[5.12] K. Gelin, Preparation and Characterization of Sputter Deposited Spectrally Selective Solar Absorbers, Ph.D. Dissertation. Sweden: Uppsala University; (2004).

[5.13] Z.Y. Nuru, Spectrally selective $Al_XO_Y/Pt/Al_XO_Y$ solar absorber coatings for high temperature solar-thermal applications. Ph.D. Dissertation, South Africa: University of Western Cape; (2014).

[5.14] A.A. Ziabari, A.B. Khatibani, Optical properties and thermal stability of solar selective absorbers based on Co-Al_2O_3 cermets. Chinese Journal of Physics 000 (2017) 1–10. 28Deut8.

[5.15] D.W. Ding, M.C. Long, W.M. Cai, Y.H. Wu, D.Y. Wu, C.Chen, In-situ synthesis of photocatalytic $CuAl_2O_4$-Cu hybrid nanorod arrays. Chem.Commun. (2009) 3588–3590.

[5.16] Y. Li, W. Qiu, F. Qin, H. Fang, V.G. Hadjiev, D. Litvinov, J. Bao, Identification of Cobalt Oxides with Raman Scattering and Fourier Transform Infrared Spectroscopy. The Journal of Physical Chemistry.

[5.17] Ch. Zou, L. Huang, J. Wang, Sh. Xue, Sol. Energy Mater. Sol. Cells 137 (2015) 243–252 .

[5.18] A. Antonaia, A.Castaldo, M.L. Addonizio, S.Esposito, Stability of W-Al_2O_3 cermet based solar coating for receiver tube operating at high temperature. Solar Energy Materials & Solar Cells 94 (2010) 1604–1611.

CHAPTER SIX

CONCLUSION AND RECOMMENDATIONS

Solar thermal Power has turned into a multi-billion, fast growing industry for meeting the ever-increasing energy requirements of the world. Solar energy harvested by selective solar absorbers can be considered environment friendly and an alternative route to alleviate our dependence on traditional energy sources such as fossil fuels. In this regard, there is an increasing demand for spectrally selective coatings for mid- and high-temperature solar thermal applications. In this thesis, the cermet-based selective solar absorber that has been designed is a femtosecond laser surface structured Co nanocylinders–Al_2O_3 cermets. Results on the optical performance of solar selective Co-Ni nanocylinder-Al_2O_3 cermet with an additional femto-second laser surface structuring are also reported.

It was confirmed that the optical absorptance characteristics of optimized femtosecond surface structured selective solar absorbers consisting of electrodeposited non-percolated and highly oriented Co nanocylinders embedded in Al_2O_3 host matrix deposited on flexible Aluminium substrates can be enhanced significantly. The ultrafast laser surface structured Co nanocylinders into Alumina host matrix exhibited an optical absorptance $\alpha(\lambda)$ above 98% and a relatively low emittance $\varepsilon(\lambda)$ of 0.03 in the spectral solar range of 200-1100nm.

The observed highly reduced reflectance can result from several absorption mechanisms which include antireflection and plasmonic effects. The random sub-wavelength surface textures created by the laser surface nanostructuring in terms of graded refractive index at the air/solid interface contribute to light absorption by the antireflection effect. The nanocermet exhibits strong absorption in the visible region because of surface plasmon resonance also known as plasmonic effect and quantum confinement effect. The surface plasmons confined to the surface interact strongly with light and they have the unique capacity to confine light to very small dimensions.

The optical properties of the ultrafast laser surface laser surface irradiated Co-nanocylinders-Al_2O_3 nanocermet strongly depend on the particle shape and size, concentration of the particle in the matrix, particle distribution and local dielectric environment in the dielectric matrix. The various sizes and shapes of the surface nanostructures that are smaller than light wavelength can also give rise to the enhanced absorptance by multiple reflections and partial absorptions of light between the surface features. Also, as a result of the gradual increase of

the refractive index of a rough surface and lower surface reflection more light gets absorbed into the selective absorber layer, it can be concluded therefore that the laser surface structured cermet does not need an anti-reflection layer.

The operation parameters that include temperature, operation time and concentration of the acid affect the optical properties of the ferromagnetic nanocermet. It was observed that the hexagonal pore pattern gets more regular when temperature decreases, anodization time and voltage increase. Surface morphology of the coatings affects the solar absorptance of the coatings. The more regular and hexagonal the cermet's pore array is the stronger its absorbance. Also, electrodeposition of the metal ions into the pore gets more accurate and of a higher percentage. In a graded cermet, the reflectance from the cermet is reduced by gradually increasing the metal volume fraction; hence the refractive index, as a function of depth from the surface to the base of the film.

The coating based on the laser surface structured Co-Al_2O_3 cermet revealed high performance as a selective solar absorber. We observed that the operating voltage and temperature are two of the most important factors in the process of production of porous alumina host matrix. The voltage influences the pore density and porosity of fabricated alumina host matrix or template. When the voltage is increased from 10V to 30V, we observe a higher degree of self-ordering and smaller diameter of pores beneficial for high absorptance in the visible range. The regular pore array achieved at 30V creates an accurate metal volume fraction while at lower voltage will result in uneven, random and reduced metallic concentration which increases the thermal emittance in the IR.

New materials that fall under cermet-based spectrally absorbers including metal inclusions and dielectrics are extensively explored because of their potential for high-temperature applications (over 400°C). The selection of the femtosecond laser nanostructured Co nanocylinders- Al_2O_3 cermet for research investigation in this thesis is because Al_2O_3 cermet based coatings have been found to have excellent optical properties and thermal stabilities. For high-temperature CSP applications, achieving thermally stable spectrally selective absorbers remains a major challenge. The hypothesis that the columnar laser induced surface structures could be due to fast melting of Co and its partial diffusion out of the pores which is plausible in view of the low melting temperature of Co suggests that this laser surface structured cermet Al_2O_3 may not be suitable for high temperature applications, especially

above 500°C. This particular application requires that the metal inclusions in the dielectric host matrix have high melting points and high nitriding and oxidation resistance. This is a possible area for further research however; within the interest of the scope of this study the thermal stability characteristics of the femtosecond laser surface structured Co nanocylinders-Al_2O_3 cermet were conducted.

To improve the overall solar selectivity and protect the selective absorber from humidity, dust and corrosive environments, self-cleaning, transparent superhydrophobic coatings on top of solar absorber coatings are recommended.

The exposure of the laser nanostrucuted Co nanocylinders- Al_2O_3 cermet samples to annealing results in their degradation at high temperature. High temperature annealing (600°C) in air affects the optical selectivity of the deposited particles, due to the oxidation of cobalt to cobalt (III) oxide. These results indicate that this type of coatings are good candidates for solar absorber applications at temperature lower than 600°C. Even though, the cermet based coatings exhibit high thermal stability in vacuum, studies have shown that their performance deteriorates significantly when exposed to air due to oxidation and/or diffusion of the metal component in the dielectric matrix which is the case with the laser nanostrucuted Co nanocylinders- Al_2O_3 cermet under investigation. Therefore, recent research has been focused towards the development of high-temperature solar selective coatings based on transition metal nitrides/oxynitrides/oxides and silicides.